

Interstellar Water Chemistry: From Laboratory to Observations

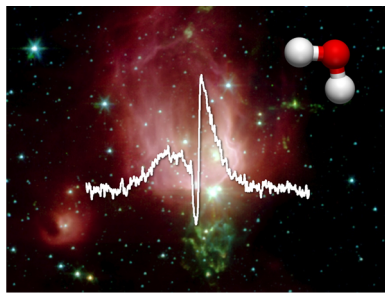
Ewine F. van Dishoeck,^{*,†,||} Eric Herbst,^{*,‡} and David A. Neufeld^{*,§}

[†]Leiden Observatory, Leiden University, P.O. Box 9513, 2300 RA The Netherlands,

[‡]Department of Chemistry, University of Virginia, P.O. Box 400319, Charlottesville, Virginia 22904, United States

[§]Department of Physics and Astronomy, Johns Hopkins University, 3400 North Charles Street, Baltimore, Maryland 21218, United States

^{||}Max Planck Institute for Extraterrestrial Physics, 85748 Garching, Germany



Background: Courtesy NASA/JPL-Caltech/T. Megeath (Harvard-Smithsonian CfA)

CONTENTS

1. Introduction	9043
1.1. Water Observations	9044
1.2. Astronomical Techniques	9045
1.2.1. Description of Telescopes	9045
1.3. Types of Interstellar and Circumstellar Clouds	9047
1.4. Types of Radiation Fields and Ionization Fraction	9048
2. Water Spectroscopy and Excitation	9050
2.1. Pure Rotational Transitions	9050
2.2. Vibrational Transitions: Gas and Ice	9051
2.3. Electronic Transitions	9052
2.4. Rate Coefficients for Inelastic Collisions	9052
2.5. Water Excitation and Radiative Transfer	9053
2.6. Masers	9054
3. Water Chemistry	9055
3.1. Low-Temperature Ion–Neutral Chemistry	9055
3.1.1. General Considerations	9055
3.1.2. Low Temperature Gas-Phase Formation of H ₂ O	9055
3.1.3. H ₂ O Photodissociation	9056
3.2. High-Temperature Gas-Phase Chemistry	9057
3.3. Ice Chemistry	9058
3.3.1. General Considerations	9058
3.3.2. Water Ice Formation	9060
3.3.3. Water Ice Desorption	9061
3.4. Solving the Kinetic Equations	9062
3.4.1. Rate Equations and Models	9063
3.4.2. Gas–Grain Simulations and Surface Chemistry	9063
3.4.3. More Advanced Approaches	9064
4. Comparison with Observations	9065
4.1. Testing Ion–Molecular Chemistry	9066
4.1.1. Water Abundances in Diffuse and Translucent Clouds	9066

4.1.2. Related Species in Diffuse and Translucent Clouds	9067
4.1.3. Dense PDRs	9067
4.2. Testing Solid-State Chemistry: Ice Formation and Photodesorption	9067
4.2.1. Cold Clouds: Ice Observations	9067
4.2.2. Cold Pre- and Protostellar Cores: Gas-Phase Water	9068
4.2.3. Outer Protoplanetary Disks	9069
4.2.4. Related Ice Species	9070
4.3. Testing Gas–Grain Chemistry: Water Ice Sublimation	9070
4.3.1. Warm Protostellar Envelopes and Hot Cores	9070
4.4. Testing High-Temperature Chemistry	9071
4.4.1. Shocks	9071
4.4.2. Supernova Remnants	9072
4.4.3. External Galaxies	9073
4.4.4. Evolved Stars	9073
4.4.5. Inner Protoplanetary Disks	9074
4.5. Testing Photodissociation Models	9075
4.5.1. Comets	9075
4.5.2. Bow Shocks	9076
4.6. Water Ortho-to-Para Ratio	9076
5. Concluding Remarks	9077
Author Information	9078
Corresponding Author	9078
Notes	9078
Biographies	9078
Acknowledgments	9079
References	9079

1. INTRODUCTION

Water is a fundamental molecule in the universe. On Earth, water exists in all three phases: gas, liquid, and solid (ice). Liquid water facilitates many chemical reactions as a solvent. Much of the geology on Earth is shaped by water. Life on Earth, and similar life elsewhere on Earth-like planets in space, would not be possible without water.

Water consists of hydrogen and oxygen atoms, which are the first and third most abundant elements in the universe.

Special Issue: 2013 Astrochemistry

Received: June 12, 2013

Published: November 21, 2013

According to the standard cosmology,^{1–3} hydrogen was formed immediately after the Big Bang, some 13.8 billion years ago (13.8 Gyr). After about 1 ms, protons and neutrons emerged from the cooling quark–gluon plasma, and after 1 s the baryonic content was frozen. Primordial nucleosynthesis produced D, He (the second most abundant element), and Li nuclei after about 3 min, and they recombined to neutral atoms after about 10⁵ yr (0.1 Myr). Heavier atoms including oxygen were produced much later in the evolution of the universe (at least a few 10⁸ yr), by nuclear fusion of H and He in the central parts of massive stars. When these stars have exhausted their supply of nuclear fuel, they develop a wind or explode as a supernova and enrich the space between the stars with heavy elements.

Even after several generations of stars, the abundance of hydrogen atoms is still some 2000 times higher than that of oxygen atoms in our solar neighborhood. Molecules such as water form in localized regions of cold and dense gas and dust between the stars (see Figure 1). Typical densities in such

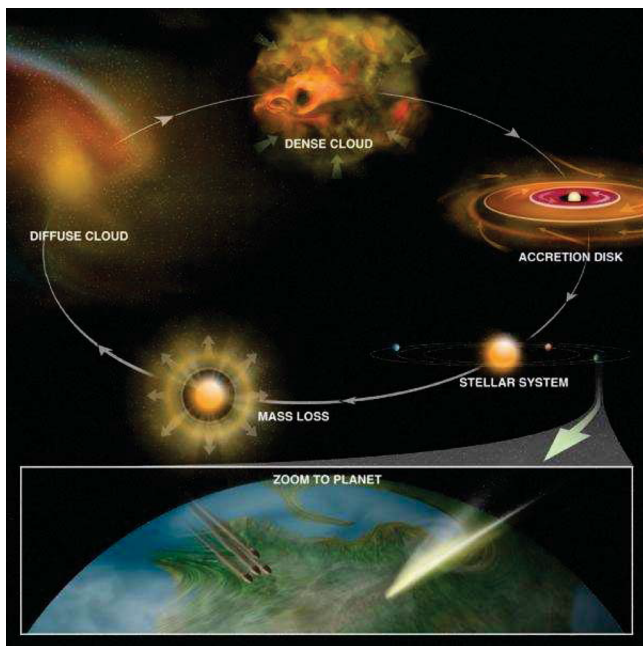


Figure 1. Schematic of different types of interstellar clouds and the cycle of the formation and death of stars. Reprinted with permission from Bill Saxton, NRAO/AUI/NSF.

interstellar clouds are 10⁴ hydrogen molecules per cm³ and temperatures can be as low as 8 K (pressure ~10⁻¹⁴ mbar). The clouds also contain small 0.001–0.1 μm sized solid dust particles or “grains”, consisting of amorphous silicates and carbonaceous material. Grains are important because they absorb and scatter the ultraviolet (UV) radiation produced by stars and thereby protect molecules from dissociating photons. Reactions on the surfaces of the dust particles promote the formation of molecules, especially of H₂ and other hydrogen-rich species like H₂O.

Interstellar space is a gigantic ultrahigh vacuum laboratory with densities low enough that molecules can form only through kinetic two-body processes in the gas phase. H₂O is one of the simplest molecules consisting of hydrogen and oxygen atoms. Hence, one would expect the chemistry of water in space to be straightforward and to have been fully understood and characterized decades ago. While the basic framework of interstellar water chemistry was indeed established in the

1970s and recognized to involve both gas-phase^{4,5} and solid-state chemistry,^{6–8} many of the key chemical processes have been measured in the laboratory only in the past decade. Tests of these chemical processes are possible only now thanks to a number of powerful telescopes, culminating with the Herschel Space Observatory, which have high enough sensitivity and spatial or spectral resolution to detect water in various environments.^{9–12}

1.1. Water Observations

Interstellar water vapor was discovered in 1969 in the Orion nebula by the group of Charles Townes.¹³ This detection was somewhat accidental, since it was found that water can emit anomalously strong radiation at 22 GHz (1.4 cm) via the maser process (see section 2.6). This self-amplifying process produces very bright and sharp lines that can be observed even in external galaxies. In fact, the best evidence for the existence of a black hole outside our Milky Way is based on tracking accurately the motions of water masers in the galaxy NGC 4258.¹⁴

While this unexpected discovery and application of water is interesting in itself, it tells us little about the actual chemistry and abundance of water in space. To probe the bulk of gaseous water, observations of lines that are thermally excited and do not exhibit population inversion are needed. Observations of the majority of these pure rotational lines are blocked from the ground by the water that is present in the Earth’s atmosphere. Hence, space missions, starting with the Infrared Space Observatory (ISO) and followed by the Submillimeter Wave Astronomy Satellite (SWAS), the Swedish-led satellite Odin, and finally the Herschel Space Observatory, have been crucial for our understanding of the water chemistry (see Table 1). Nonmasing water emission has now been detected in many environments ranging from diffuse clouds to dense planet-forming disks around young stars in the Milky Way and from nearby galaxies out to the highest redshifts. Water is also found in cometary comae, the atmospheres of planets in our own solar system, and even those of extrasolar planets, or exoplanets¹⁵ (see Figure 2, from Weiß et al.,¹⁶ and Figure 3, adapted from Seager and Deming¹⁷ and Madhusudhan and Seager¹⁸ for two extreme examples of water in the distant and nearby universe, respectively).

At the low densities and high vacuum conditions in space, water exists either as a gas or in the solid state as ice. Liquid water can only occur under relatively higher pressures on large solid bodies such as asteroids or planets; its triple point is at 273 K and 6.1 mbar. Water gas freezes out as ice around 100 K under interstellar conditions.¹⁹ Water ice was detected in 1973 in the infrared spectra of protostars forming deep inside molecular clouds²⁰ and is now found in dense interstellar clouds throughout our own and external galaxies.²¹

This review provides first an overview of the techniques to observe water in space (section 1.2), of the types of clouds in which water is observed (sections 1.3 and 1.4), and of water spectroscopy and excitation (section 2). The bulk of the review discusses the various chemical processes that lead to the formation of water, both in the gas phase and on the surfaces of grains (section 3). Many of these processes also apply to other molecules, but the focus here is on water. Finally, the different chemical routes to water are tested against a wide range of observations, from tenuous molecular clouds in which UV radiation penetrates to high-density regions in which stars and planets are currently forming (section 4). The discussion is limited to H₂¹⁶O and its ¹⁸O and ¹⁷O isotopologues. The chemistry of HDO is similar to that of H₂O in many aspects, but

Table 1. Important Telescopes for Water Observations

telescope	wavelength/frequency	spectral resolving power R	spatial resolution ^a
SWAS	557 GHz	10^6	$3.2' \times 4.0'$
Odin	557 GHz	10^6	$2'$
ground cm	22 GHz	10^6	$0.001''$ to a few arcsec
ground mm	many, e.g., 183, 380 GHz 203 ^b , 391 ^b , 692 ^b GHz	10^7 10^7	$0.2\text{--}20''$ $0.2\text{--}20''$
Herschel-HIFI ^c	480–1250 GHz 1410–1910 GHz	10^7 10^7	$44''\text{--}17''$ $15''\text{--}9''$
Herschel-PACS ^d	55–210 μ m	$(1 - 5) \times 10^3$	$9.4''$
Herschel-SPIRE ^e	200–670 μ m	$\sim 10^3$	$17\text{--}42''$
Spitzer	10–38 μ m	600	$10''$
ISO-SWS ^f	2.5–45 μ m	2000, 20000	$14'' \times 20''$ to $17 \times 40''$
ISO-LWS ^g	45–197 μ m	200, 10000	$\sim 80''$
ground 4–10 m optical	2.8–3.3 μ m	$\leq 10^8$	$\leq 1''$
ground 4–10 m infrared	11–14 μ m	10^4	$1''$

^a1 arcmin = $1' = 60''$. ^b $H_2^{18}O$. ^cHeterodyne instrument for the far infrared. ^dPhotodetector array camera and spectrometer. ^eSpectral and photometric imaging receiver. ^fShort-wavelength spectrometer. ^gLong-wavelength spectrometer.

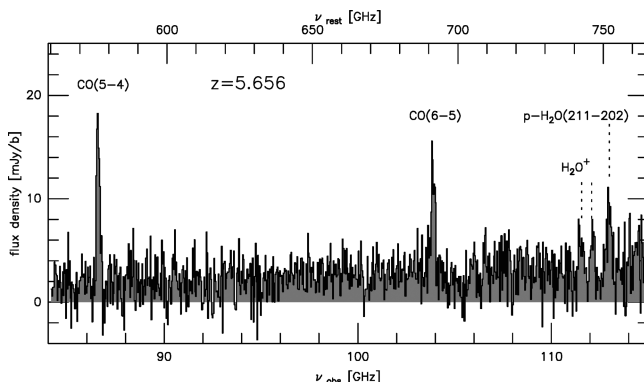


Figure 2. ALMA spectrum of the distant galaxy SPT0346-52 showing detections of pure rotational lines of neutral and ionized water, together with CO. The galaxy has a red-shift of $z = 5.66$ [transition shifted to $\nu = \nu_{\text{rest}}/(1 + z)$]. This red-shift corresponds to an age of just 1.0 Gyr since the Big Bang. Reprinted with permission from Reference 16. Copyright 2013 American Astronomical Society.

there are also important differences due to fractionation reactions that can selectively enhance HDO. Although interesting by themselves, discussion of these processes is outside the scope of this review. HDO is summarized in recent reviews by Caselli and Ceccarelli²² and by Ceccarelli et al.²³

1.2. Astronomical Techniques

Water can be observed through various transitions over a range of wavelengths (see section 2), which require different telescopes, instruments, and detectors, as summarized in Table 1. Throughout this paper, we will use the astronomical convention to indicate submillimeter lines through their frequencies in GHz and far-infrared lines through their wavelengths in μ m. Laboratory spectroscopists usually adopt either GHz or wavenumbers (cm^{-1}). For reference, 200/100/50 μ m correspond to 50/100/200 cm^{-1} and 1500/3000/6000 GHz, respectively.

Astronomers express the spatial resolution that can be achieved by their telescopes in units of seconds of arc, or arcseconds. One arcsec is $1/3600$ of a degree or $1/206265$ of a radian ($\pi/180/3600$). The nearest interstellar clouds are at a distance of ~ 150 parsec, with parsec being a distance unit employed by astronomers. A parsec is defined as the distance from the Sun

under which the Sun–Earth system is seen with an angle of 1 arcsec. In practice, 1 pc = 3.086×10^{18} cm or 3.261 lightyear. Another distance unit often used is the astronomical unit (AU; not to be confused with atomic unit or arbitrary unit), which is defined as the average Sun–Earth distance, 1 AU = 1.496×10^{13} cm. At a distance of 100 pc, 1 arcsec ($''$) corresponds to 100 AU diameter. Thus, a typical beam (spatial resolution element) of the Herschel Space Observatory of $20''$ on the sky encompasses a 3000 AU (0.015 pc) diameter region if one of the closest star-forming regions at 150 pc distance is observed. For comparison, the mean orbital radius of Neptune in our own solar system is at ~ 30 AU, so to study a planet-forming region in the nearest clouds requires a spatial resolution of $0.2''$. Such high spatial resolution is only just being achieved by the Atacama Large Millimeter/Submillimeter Array (ALMA). In the following, the main telescopes for observing water are briefly discussed.

1.2.1. Description of Telescopes. The Infrared Space Observatory (ISO) was a cooled 0.6 m infrared telescope in space covering the 2.5–240 μ m range and operative from 1995 to 1998. It had two spectrometers on board: the short-wavelength spectrometer (SWS, 2.5–45 μ m)²⁴ and the long-wavelength spectrometer (LWS, 45–197 μ m).²⁵ Each instrument had a low-resolution grating and a high-resolution Fabry–Perot mode, which provided modest resolving powers $R = \lambda/\Delta\lambda$ ranging from ~ 200 up to $\sim 10^4$. The mid- to far-infrared wavelength range is particularly rich in rotational transitions of H_2O and related hydrides, as well as vibrational bands of gas and ice. ISO indeed provided a first view of the wealth of H_2O features and its gas-grain chemistry.^{10,26}

SWAS,²⁷ launched in 1998, and Odin,²⁸ launched in 2001, were pioneering submillimeter satellites with antennas of ~ 0.6 and 1.1 m diameter, respectively, operating primarily in the 1998–2007 period. Both missions were specifically designed to observe the lowest pure rotational $1_{10}\text{--}1_{01}$ transition of H_2O at 557 GHz. The receivers were based on the heterodyne technique, in which the high-frequency signal from the sky is down-converted by mixing with a local oscillator signal tuned to a nearby frequency. The difference signal has a much lower frequency, which can be amplified with standard radio techniques. Heterodyne receivers naturally have very high spectral resolving power $R > 10^6$. Since the velocity resolution $\Delta\nu = c\Delta\lambda/\lambda$, with c being the speed of light, this value of R corresponds to $<0.3 \text{ km s}^{-1}$ in velocity units. Typical observed

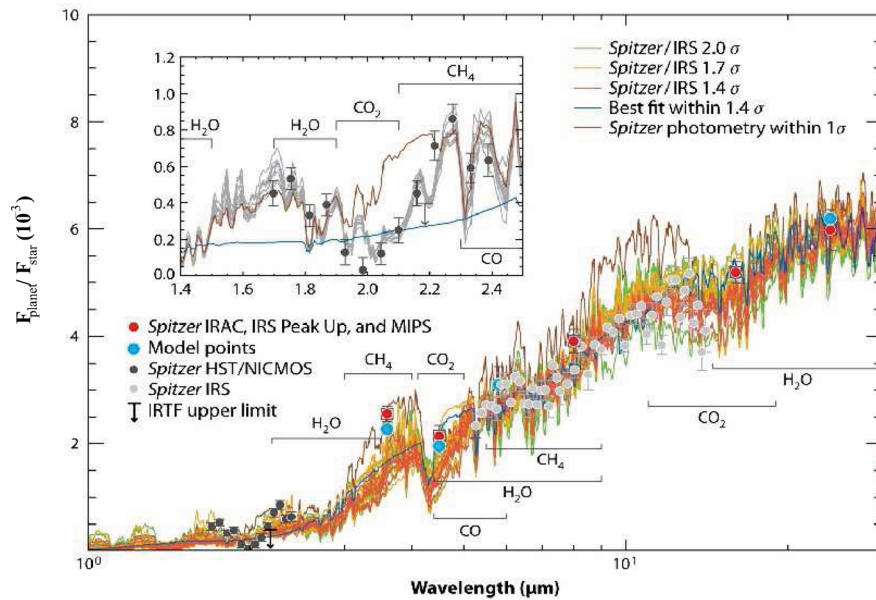


Figure 3. Spectrum of the exoplanet HD 189733b observed by various instruments (black and blue dots and squares with error bars), together with various model spectra suggesting the presence of water in absorption. Adapted with permission from ref 17 (copyright 2010 Annual Reviews) and ref 18 (copyright 2009 American Astronomical Society).

widths of water lines range from a few kilometers/second up to 100 km s^{-1} , so these spectra fully resolve the kinematics of the gas.

The Herschel Space Observatory²⁹ was a 3.5 m diameter telescope, operative from mid-2009 to mid-2013. It had three instruments that provided imaging and spectroscopic capabilities in the 55–672 μm wavelength range. As for the earlier missions, observing water in space was one of the main drivers for the design of Herschel. Because the instruments were housed in a superfluid helium cryostat and the telescope was bigger, the sensitivity of Herschel was much higher than that of SWAS and Odin. Moreover, because the sharpness of the images scales inversely with the diameter of the telescope, the spatial resolution provided by Herschel was up to an order of magnitude higher than that of the earlier missions.

Of the three Herschel instruments, the results from the heterodyne instrument for the far-infrared (HIFI) will be highlighted most in this review.³⁰ HIFI was a very high resolution (R up to 10^7) heterodyne spectrometer covering the 490–1250 GHz (600–240 μm , 16 – 42 cm^{-1}) and 1410–1910 GHz (210–157 μm , 47 – 64 cm^{-1}) bands. HIFI observed a single pixel on the sky at a time. The photodetector array camera and spectrometer (PACS) consisted of a camera and a medium resolution imaging spectrometer for wavelengths in the range 55–210 μm (180 – 47 cm^{-1}).³¹ The PACS spectrometer obtained spectra simultaneously over a limited wavelength range at each pixel of a 5×5 array. The detector consisted of a 25×16 pixel Ge:Ga photoconductor array. The Spectral and Photometric Imaging REceiver (SPIRE) was a camera and a low resolution Fourier Transform Spectrometer for wavelengths in the range 194–672 μm (51 – 15 cm^{-1}) using bolometers to detect the radiation.

Most of the water line radiation from space does not reach telescopes on the ground, however, because it is absorbed by the abundant water in the Earth's atmosphere. However, high-lying maser lines of H_2^{16}O such as the 3_{13} – 2_{20} 183 GHz and 4_{14} – 3_{21} 380 GHz lines, as well as the well-known 6_{16} – 5_{23} line at 22 GHz (1 cm) through which interstellar water was originally discovered, can be observed from Earth.³²

Another option is to observe water isotopologs. About 1 in 500 water molecules in space contain the heavier ^{18}O isotope. Some signatures from H_2^{18}O , such as the 3_{13} – 2_{20} line at 203 GHz, the 4_{14} – 3_{21} line at 391 GHz, and the 5_{32} – 4_{41} line at 692 GHz, are able to penetrate the Earth's atmosphere, even if nonmasing, and these lines have been detected with ground-based telescopes such as the 10 m Caltech Submillimeter Observatory (CSO), the 15 m James Clerk Maxwell Telescope (JCMT), and the IRAM 30 m telescope. Interferometers are even more powerful: these consist of arrays of antennas for which the signals are combined to produce a single, sharper image. Examples include the IRAM Plateau de Bure Interferometer (PdBI) ($6 \times 15 \text{ m}$ dishes), the SubMillimeter Array (SMA) ($8 \times 6 \text{ m}$), and, most importantly, the recently inaugurated ALMA ($54 \times 12 \text{ m} + 12 \times 7 \text{ m}$). Since these ground-based telescopes and arrays are much bigger and can see up to a 1000 times more sharply than any of the current or past satellites, they allow astronomers to zoom in on the astronomical sources and map the location of water isotopologues in detail.³³ However, ground-based facilities can only observe thermal lines from warm water ($>100 \text{ K}$), not from cold water.

The Spitzer Space Telescope was launched in 2003 and performed mid-infrared spectroscopic observations from 5–38 μm until the mission ran out of coolant in mid-2009. The IRS instrument had modest resolving power $R = 600$ from 10 to 38 μm , but only $R \sim 50$ from 5 to 10 μm .³⁴ However, its sensitivity surpassed that of ISO by nearly 3 orders of magnitude due to the new generation of large format Si:As array detectors. Spitzer was therefore able to open up a completely new view of warm water in planet-forming regions by observations of highly excited pure rotational lines. It was also very well suited to detect solid-state bands of water ice in sources similar to those that led to our own solar system.

A variety of large (4–10 m) ground-based optical telescopes have near- and mid-infrared spectrometers that can observe the vibration–rotation lines of hot water near 3 μm as well as highly excited pure rotational lines near 10 μm . Examples of instruments are Keck-NIRSPEC ($R = 25000$), VLT-CRIRES

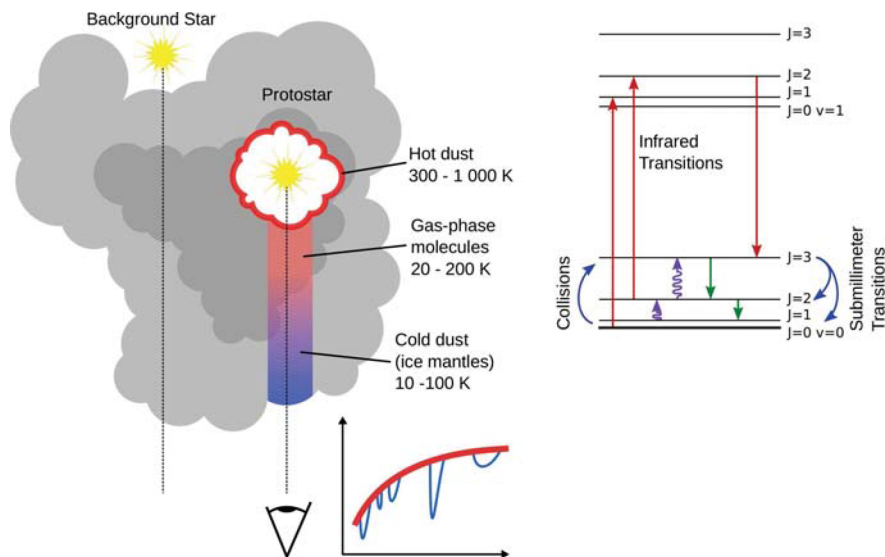


Figure 4. (Left) Schematic energy level diagram showing typical pure rotational submillimeter and vibration–rotation near-infrared lines, together with various radiative and collisional processes that excite the molecules. (Right) Cartoon illustrating infrared absorption line observations of ice or gas toward an embedded protostar or a background star. The hot (300–1000 K) dust near the star provides the continuum against which cold ice and gas can be seen in absorption. Absorption can also occur against cool background stars.

Table 2. Types of Interstellar and Circumstellar Clouds and Their Physical Characteristics

name	typical density (cm^{-3})	typical temp (K)	typical A_V (mag) ^a	examples
diffuse cloud	10^2	30–100	≤ 1	ζ Oph
translucent cloud	10^3	15–50	1–5	HD 154368
dense PDR	10^4 – 10^5	50–500	<10	Orion Bar
cold dense cloud	10^4 – 10^5	10–20	>10	Taurus cloud
prestellar core	$\geq 10^5$	8–15	10–100	L1544
prostellar envelope				
cold outer	10^4 – 10^7	8–100	10–100	NGC 1333 IRAS4A
warm inner/	10^7 – 10^9	≥ 100	100–1000	W3 IRS5
hot core				Orion hot core
shock	10^4 – 10^5	200–2000	\leq few	L1157 B1
protoplanetary disk				
outer	10^6 – 10^{10}	10–500	1–100	TW Hya, HD 100546
inner	10^9 – 10^{15}	100–3000	1–1000	AS 205
AGB envelope				
outer	$< 10^8$	10–100	1–50	IRC+10216 (C-rich)
inner	10^{10} – 10^{13}	100–2000	50–1000	VW CMa (O-rich)

^aSee section 1.4 for definition.

($R = 10^5$), VLT-VISIR ($R = 10^4$), and Gemini-Michelle and -TEXES. Most of them are echelle grating spectrometers using large-format infrared detector arrays in which one array dimension is used for the spectral range and the other array dimension for the spatial domain. Thus, these “long-slit” spectrometers also provide information on the spatial distribution of the emission on subarcsec scale. In the future, the EXES mid-infrared instrument ($R = 10^5$) on the Stratospheric Observatory for Infrared Astronomy (SOFIA),³⁵ a 2.7 m telescope onboard a B747 airplane, will be a powerful facility as well for water observations since it flies at 13.7 km above much of the Earth’s atmosphere.

At near- and mid-infrared wavelengths, cold ices and gases can be seen in absorption against a bright continuum. This continuum can be provided by hot dust close to either a young or old star, but it can also be due to a background star (see Figure 4). Absorption observations probe only a pencil-beamline-of-sight toward the source. In contrast, submillimeter and far-

infrared lines of warm and cold gaseous water are generally in emission and can thus be mapped. Cold water gas can also absorb against line emission from warmer water at larger distances.

The bound–bound electronic transitions of H_2O at UV wavelengths can in principle be observed using high spectral resolution instruments (up to 10^5) on the Hubble Space Telescope (HST) and the Far Ultraviolet Space Explorer (FUSE), in absorption along the line of sight to a bright star. However, there are no detections of interstellar water at UV wavelengths to date.³⁶

1.3. Types of Interstellar and Circumstellar Clouds

The interstellar medium has a complex and inhomogeneous structure, the denser concentrations of which are called clouds (see the book by Tielens³⁷ and Tielens³⁸ for broad overviews). A summary of typical densities, temperatures, and extinctions (see section 1.4) of various cloud types discussed here is presented in Table 2. The regions range from low density diffuse clouds in

which UV radiation can readily penetrate to cold dense cores on the verge of collapse to form a star to the envelopes around dying stars (Figure 1). Diffuse and translucent clouds are low-density examples of photo-dissociation or photon-dominated regions (PDRs);³⁹ traditional PDR examples are dense clouds illuminated by a nearby bright star, such as seen in Orion. The terminology indicates that the physics and chemistry are controlled by far-ultraviolet (FUV; 912–2000 Å) radiation. When the nearby source emits X-rays, the region is called an XDR.

The principal ingredient of clouds is hydrogen, followed by helium (about 0.10 by number). Oxygen, carbon, and nitrogen are present with abundances of 5×10^{-4} , 3×10^{-4} , and 1×10^{-4} , respectively. The small silicate and carbonaceous dust grains make up ~1% of a cloud by mass but only $\sim 10^{-12}$ by number. Hydrogen is primarily in molecular form in the regions listed in Table 2 but is difficult to observe directly. Astronomers therefore usually observe the strong lines from the abundant CO molecule and its isotopologues as a tracer of H₂, even though this naturally introduces uncertainties.

Much of this review discusses water associated with star-forming regions in which a cloud is collapsing under its own gravity to form one or more protostars. In this stage, the young star is deeply embedded in its natal cloud and is still accreting material from the envelope and thus growing in mass. The luminosity from the young star heats the envelope and sets up a radial gradient in temperature, with values in the inner envelope (sometimes also called “hot core”) well above 100 K and temperatures in the colder outer regions down to 10 K. Because the cloud always has some angular momentum, material cannot continue to fall in radially but part of it ends up in a rotating disk around the young star (Figure 1). The protostar also develops jets and winds that can escape in a direction perpendicular to the disk. When these high-velocity jets and winds interact with the quiescent surrounding envelope and cloud, they create shocks, and material can be entrained in so-called bipolar outflows. Figure 5⁴⁰ illustrates the different protostellar components. Although this cartoon refers to an isolated low-mass protostar (mass $< 2 M_{\odot}$, luminosity $< 10^2 L_{\odot}$) which will develop into a star like our Sun, the same physical components are also found in high-mass protostellar environments forming stars such as those seen in Orion (mass $< 8 M_{\odot}$, luminosity $> 10^4 L_{\odot}$).

With time (~ 1 Myr), the opening angle of the wind increases and the envelope material is gradually dispersed, revealing a young pre-main sequence star surrounded by a so-called protoplanetary disk. The term “pre-main sequence” indicates that the young star is not yet in its stable hydrogen-burning stage, although nuclear fusion of deuterium nuclei does occur. The young star emits UV radiation from the stellar corona as well as from shocked accreting material that is being funneled from the disk onto the star. Once accretion stops and the disk becomes less turbulent, the sub-micrometer-sized grains coagulate to larger and larger particles and settle to the midplane (a few megayears). There they can form kilometer-sized planetesimals that interact gravitationally to form (proto)planets and eventually a full planetary system that may or may not resemble our planetary system (up to 100 Myr). Within our solar system, comets and asteroids are left-over planetesimals that did not make it into a planet and were scattered and preserved in the outer regions of the disk or “nebula” out of which our solar system formed. The star itself reaches the main sequence after a few $\times 10^7$ yr.

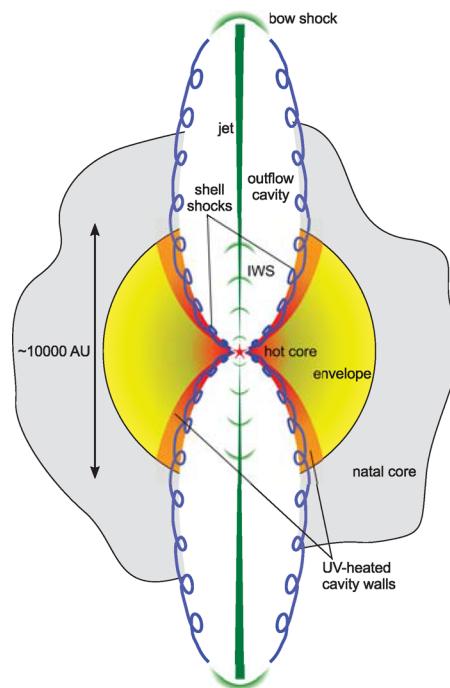


Figure 5. Cartoon of a protostellar envelope with the different physical components and their nomenclature indicated. IWS stands for internal working surfaces. The indicated scale is appropriate for a low-mass protostar. On this scale, the ~100 AU radius disk surrounding the protostar is not visible. Reprinted with permission from ref 40. Copyright 2011 The University of Chicago Press.

At the end of their life cycle, low-mass stars have exhausted their nuclear fuel and they are no longer stable but expand and lose part of their mass (Figure 1). These evolved asymptotic giant branch (AGB) stars are therefore surrounded by circumstellar envelopes, i.e., extended dense shells of molecular material that can also contain water. The temperatures are high, 2000–3000 K near the stellar photosphere, but drop with radius down to 10 K at the outer edge. Depending on the type of star, the envelopes can be either carbon-rich (with an elemental abundance of carbon exceeding that of oxygen) or oxygen-rich.

High-mass, young stars evolve much faster than their low-mass counterparts and are still embedded in their natal clouds when they reach the hydrogen-burning main sequence phase, after $\sim 10^5$ yr.⁴¹ Thus, they do not have an optically visible premain sequence stage, and the existence of disks around high-mass, young stars is still heavily debated. High mass stars emit copious UV photons that can ionize atomic hydrogen, leading to a fully ionized H II region surrounding the young star once it has reached the main sequence. At the end of their lives, they explode as supernovae with their cores ending up as black holes or neutron stars.

1.4. Types of Radiation Fields and Ionization Fraction

UV radiation plays an important role in interstellar chemistry, both in destroying chemical bonds and in liberating molecules from the ice. The UV radiation impinging on an interstellar cloud is often approximated as the average radiation produced by all stars from all directions in its neighborhood. The average interstellar radiation field (ISRF) has been characterized by Habing⁴² and Draine⁴³ to have an intensity of about $I_0 = 10^8$ photons cm⁻² s⁻¹, with a relatively flat spectrum between 912 and 2000 Å (Figure 6).⁴² The threshold of 912 Å corresponds to the ionization potential of atomic H at 13.6 eV; because of its high

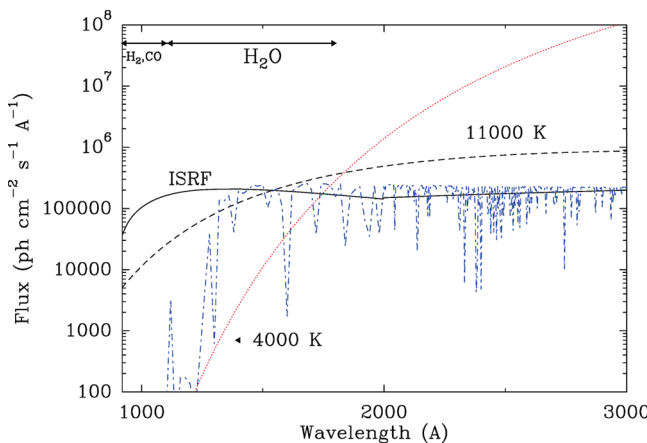


Figure 6. Comparison of the general interstellar radiation field of Draine (extended for $\lambda > 2000 \text{ \AA}$ using ref 46) with various stellar radiation fields scaled to have the same integrated intensity from 912 to 2000 \AA . The scaled stellar atmosphere model radiation field of a B9 star⁴⁷ ($T_* \approx 11\,000 \text{ K}$) is included as well (dashed-dotted). The wavelength range where the photodissociation of H_2O occurs is indicated. (The figure is based on ref 45.)

abundance, virtually all photons with energies above 13.6 eV are absorbed by H and do not affect the chemistry.

If a cloud is located close to a bright star, the radiation from the star itself can dominate over that of the general ISRF. For hot O- and B-type stars with effective photospheric temperatures of $T_* = 20\,000\text{--}50\,000 \text{ K}$, the shape of the radiation field is not very different from that of the ISRF. However, cooler A-, F-, G-, K-, and M-type stars with $T_* = 3000\text{--}10\,000 \text{ K}$ will have many fewer FUV photons to dissociate molecules. In some sources (e.g., young stars, shocks), Lyman α radiation at 1216 \AA dominates the radiation field. Water has a substantial photodissociation cross section at this wavelength, whereas other molecules like CO, N₂, and CN do not (see Tables and discussion in Bergin et al.⁴⁴ and van Dishoeck et al.⁴⁵).

Dust particles attenuate the UV radiation with depth into a cloud, thereby shielding molecules from the harshest radiation. The dust optical depth at wavelength λ is given by³⁷ $\tau_d(\lambda) = n_d C_{\text{ext}}(\lambda) L$, where n_d is the dust density in cm^{-3} , C_{ext} the extinction cross section in cm^2 , and L the path length in cm. The

extinction is the sum of absorption and scattering processes. Astronomers usually measure the extinction at visual wavelengths, A_V , which is defined as $1.086 \times \tau_d$ at 5500 \AA . The intensity decreases as $I_{5500} = I_0 10^{-0.4A_V}$ with depth into a cloud. The steepness of this decline increases toward UV wavelengths and depends on the grain properties such as size, composition, shape, and scattering characteristics.⁴⁸ The observed extinction curve from infrared to UV wavelengths implies that there must be a large range of grain sizes. Most of the dust mass is in $\sim 0.1 \mu\text{m}$ grains, but most of the surface area is in much smaller grains, down to $0.001 \mu\text{m}$ or less. These smaller grains dominate the absorption and scattering of UV radiation.

For a typical interstellar grain size distribution, UV radiation ceases to be important at $A_V \approx 5 \text{ mag}$, when the intensity at visible wavelengths has declined by a factor of 100 and that at UV wavelengths by a factor of at least 10^4 . Because the extinction increases monotonically with path length L , A_V (in units of magnitudes) is often used as a measure of depth into a cloud. Another quantity often used by astronomers is that of column density in cm^{-2} , i.e., the number density n in cm^{-3} of a species integrated along a path, $N = \int n \text{ d}L$. The relation between extinction and the column density of hydrogen nuclei is found empirically to be^{49,50} $N_{\text{H}} = N(\text{H}) + 2N(\text{H}_2) = (1.8 \times 10^{21})A_V \text{ cm}^{-2}$, based on observations of diffuse clouds where both $N(\text{H})$, $N(\text{H}_2)$, and A_V are measured directly.

Cosmic ray particles, i.e., highly energetic atomic nuclei with $>\text{MeV}$ energies, penetrate even the densest clouds and provide the required level of ionization to kick-start the chemistry. The resulting ions can react rapidly with neutral molecules down to very low temperatures as long as the reactions are exothermic and have no activation barrier (see section 3.1). The cosmic rays also maintain a low level of UV radiation by interacting with hydrogen.⁵¹ The ionization of H and H₂ produces energetic secondary electrons that can bring H₂ into excited electronic states. These states subsequently decay through spontaneous emission, mostly in the H₂ B-X Lyman and C-X Werner bands, producing a UV spectrum consisting of discrete lines and a weak continuum in the 900–1700 \AA range.⁵² The flux of internally generated UV photons is typically $10^4 \text{ photons cm}^{-2} \text{ s}^{-1}$ but depends on the energy distribution of the cosmic rays (see Figure 4 of Shen et al.⁵³).

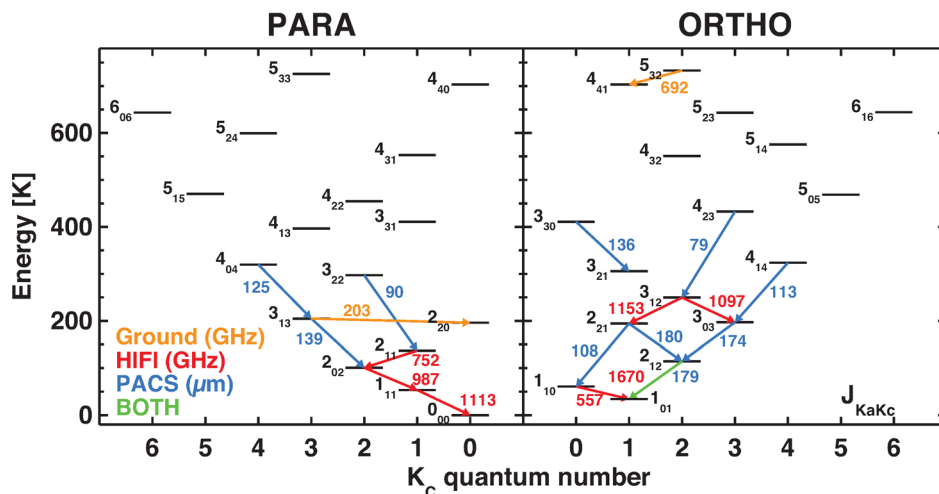


Figure 7. Energy levels of ortho- and para- H_2O , with some important transitions observed with Herschel-HIFI (in GHz) and Herschel-PACS (in μm) indicated. Adapted with permission from ref 40. Copyright 2011 The University of Chicago Press.

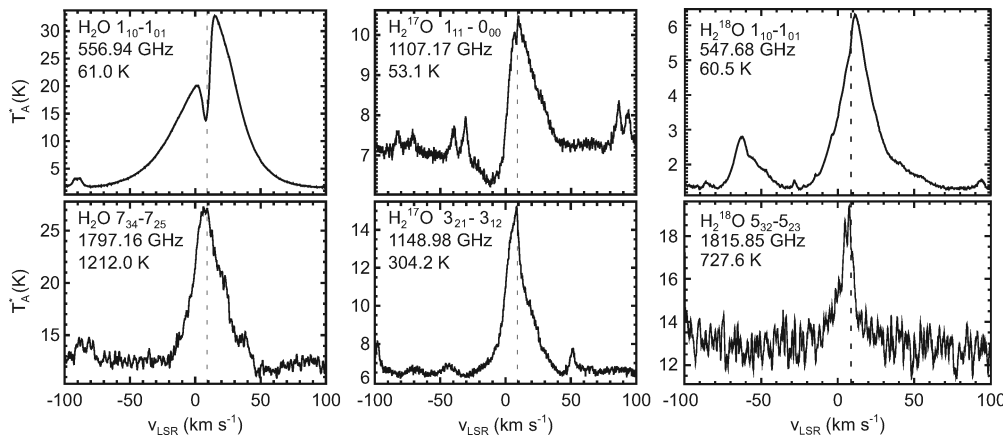


Figure 8. Examples of pure rotational lines of H₂O and its isotopologues observed with Herschel-HIFI toward the Orion-KL molecular cloud. The quantum numbers, frequencies, and upper energy level of the transitions are indicated. The velocity scale is in the so-called local standard of rest (LSR) frame; the dashed line indicates the 9 km s⁻¹ velocity of the cloud. In this and other submillimeter heterodyne spectra, the units of intensity are in (antenna or main-beam) temperature T_A or T_{mb} in kelvin, as commonly used by radio astronomers. The Rayleigh–Jeans equation relates this temperature to intensity I through $T_{mb} = c^2/(2k_B\nu^2)I_L$, where c is the speed of light, k_B is the Boltzmann constant, and ν is frequency. Adapted with permission from ref 67. Copyright 2010 American Astronomical Society.

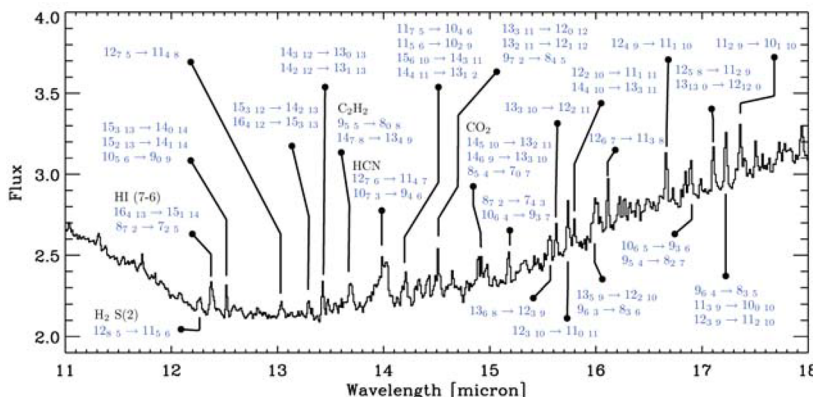


Figure 9. Spitzer spectrum of the protoplanetary disk around the young star RNO 90 illustrating the detection of many highly excited pure rotational water lines in space. Some representative identifications are indicated; many features are blends at the low spectral resolving power $R = 600$ of the Spitzer-IRS. Transitions refer to $J_{K_a K_c}$ in the ground vibrational state of H_2^{16}O unless otherwise indicated. Reprinted with permission from ref 74. Copyright 2010 American Astronomical Society.

Some cosmic sources (e.g., hot matter near young stars or black holes) also produce X-rays that can impact the chemistry. However, in practice, their chemical effects are similar to those of cosmic rays.⁵⁴

Interstellar clouds are largely neutral. In diffuse clouds, the UV radiation from the ISRF can ionize atomic carbon because its first ionization potential is less than 13.6 eV, in contrast with oxygen and nitrogen. Since the abundance of gas-phase carbon with respect to hydrogen is about 10^{-4} , this also sets the maximum electron fraction in the cloud (about two-thirds of the carbon budget is locked up in carbonaceous grains). With depth into the cloud, the UV radiation decreases and carbon is converted from atomic into molecular form. Around $A_V = 5$ mag, cosmic rays take over as the main ionizing agent at a rate denoted by ζ in s^{-1} . The resulting ionization fraction depends on the detailed chemistry and grain physics but is typically 10^{-8} – 10^{-7} and scales as $(n/\zeta)^{-1/2}$.

2. WATER SPECTROSCOPY AND EXCITATION

Water has dipole-allowed pure rotational, vibrational, and electronic transitions that occur at far-infrared/submillimeter,

infrared, and ultraviolet wavelengths, respectively. Water has three vibrational modes: the ν_1 symmetric stretch centered at 2.7 μm , the ν_2 bending mode at 6.2 μm , and the ν_3 asymmetric stretch at 2.65 μm . Astronomical examples of each of the types of transitions are presented.

2.1. Pure Rotational Transitions

H_2O is an asymmetric rotor with an irregular set of energy levels characterized by quantum numbers $J_{K_A K_C}$, where J indicates the total rotational quantum number of the molecule and K the projections of J on the principal axes of inertia. For asymmetric rotors like H_2O , K_A and K_C indicate the K values at the prolate and oblate symmetry limits to which the level correlates. Because of the nuclear spin statistics of the two hydrogen atoms, the H_2O energy levels are grouped into ortho ($K_A + K_C = \text{odd}$, parallel nuclear spins of the H nuclei) and para ($K_A + K_C = \text{even}$; antiparallel nuclear spins of H nuclei) ladders (Figure 7). Radiative transitions between these two ladders are forbidden to high order, so that only chemical reactions can effectively transform one form of water into the other by exchanging an H atom. The energy levels within each ladder are populated by a combination of collisional and radiative excitation and de-

excitation processes (see section 2.5). The radiative rates are governed by the electric dipole moment of water, $\mu_D = 1.85 \text{ D}$ ($6.17 \times 10^{-30} \text{ C m}$).

There are two main publicly available databases that summarize the transition frequencies, transition strengths or Einstein A coefficients, and statistical weights for astronomically relevant molecules like water: the Jet Propulsion Laboratory catalog (JPL)⁵⁵ (spec.jpl.nasa.gov) and the Cologne Database for Molecular Spectroscopy^{56,57} (www.astro.uni-koeln.de/cdms/catalog).

The molecular data for H_2O in the vibrational ground state are well-known up to very high J -values from laboratory work starting more than 30 years ago.^{58–60} For pure rotational transitions within ν_2 , $2\nu_2$, ν_1 , and ν_3 vibrationally excited states, new measurements⁶¹ and intensities⁶² have recently become available.

The spectroscopy of the important isotopologues H_2^{18}O and H_2^{17}O is less well covered in the laboratory, and new measurements of transitions in vibrationally excited states are warranted. The current line lists derive primarily from older work.^{58,63–66}

Many of the pure rotational lines of water and its isotopologues have been detected at submillimeter and far-infrared wavelengths toward bright sources such as the Orion molecular cloud^{67–70} (see Figure 8 for example). Very highly excited pure rotational lines up to $J = 18$ ($E_u/k \approx 5000 \text{ K}$) are found at mid-infrared wavelengths in low-resolution Spitzer Space Telescope data at $10–38 \mu\text{m}$.^{71–74} An example spectrum of an infrared spectrum of a protoplanetary disk is presented in Figure 9. In contrast with the submillimeter spectra, the mid-infrared lines are generally not resolved so that most features are blends of lines.

2.2. Vibrational Transitions: Gas and Ice

The vibration–rotation transitions of water at infrared wavelengths have been studied for many decades in the laboratory,^{75,76} and all the relevant molecular data are summarized in the HITRAN database⁷⁷ at www.cfa.harvard.edu/hitran. Most recently, line lists appropriate for temperatures up to several thousand kelvin and including higher vibrational transitions have been published for water and its isotopologues^{60,78–82} and are posted at www.exomol.com/molecules/H2O.html. The higher temperature data are particularly important for exoplanets and cool stellar atmospheres. An example of an observed vibration–rotation spectrum at low spectral resolution toward a high-mass protostar is presented in Figure 10.⁸³

There is also a rich literature on laboratory spectroscopy of water ice, both for interstellar and solar system applications.^{84,85} In contrast with low pressure gas-phase spectra, the solid-state water spectra have no rotational substructure and are very broad, with profiles that depend on the morphology, temperature, thermal history, and environment of the water molecules.^{86–91} For example, the spectrum of crystalline water ice has a sharp feature around 3200 cm^{-1} ($3.1 \mu\text{m}$) that is lacking in amorphous water ice (Figure 11).⁹² Most water ice in the universe is actually thought to be in a high-density amorphous ice form that does not occur naturally on Earth.^{89,93} Porous ices have dangling OH bonds that absorb around 3700 cm^{-1} ($2.70 \mu\text{m}$)⁹⁴ but are not seen in space. In interstellar ices, water is mixed with other species such as CO and CO_2 , which can block the dangling OH bands and affect both the line profiles and intensities, as illustrated by laboratory studies for the $6 \mu\text{m}$ bending mode.⁹⁵

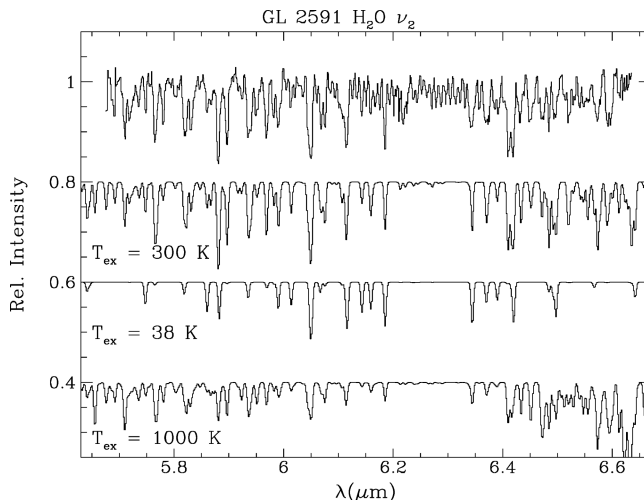


Figure 10. Vibration–rotation lines of H_2O in the ν_2 band observed with ISO-SWS in absorption toward the high-mass protostar AFGL 2591. The normalized spectrum is compared with simulated spectra for various excitation temperatures, with 300 K providing the best fit. The model spectra are offset vertically for clarity. Even at this low spectral resolving power of $R \approx 2000$, the data can distinguish between different models. Reprinted with permission from ref 83. Copyright 1996 European Southern Observatory.

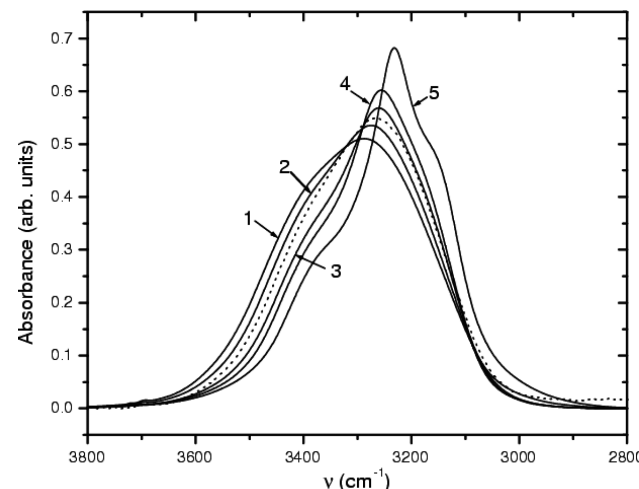


Figure 11. The OH stretching mode at $3.3 \mu\text{m}$ of a sample of pure water ice as deposited on a quartz substrate at 12 K (dashed line), compared with the spectra of water ice deposited on a CsI substrate (solid lines): (1) after deposition at 12 K and (2) after warm-up to 50 K , (3) to 80 K , (4) to 120 K , and (5) to 160 K . Note the appearance of a sharp peak due to crystallization at 160 K . Under interstellar conditions at much lower pressures and slower warm-up rates, the phase transitions shift to lower temperatures (see section 3.3.3). Reprinted with permission from ref 92. Copyright 2002 European Southern Observatory.

The far-infrared librational modes of water ice at 45 and $63 \mu\text{m}$ have been measured as well.^{96,97} Laboratory spectra for fitting astronomical data can be downloaded from various Web sites such as the NASA-Ames ice database at www.astrochem.org/db.php and the Leiden ice database at www.strw.leidenuniv.nl/~lab.

Water ice has been observed both from the ground at $3 \mu\text{m}$ and in space up to long wavelengths with a wide variety of instruments^{98–100} (Figure 12). In most cases, the absorption is against the hot dust surrounding a protostar embedded within the cloud, but there is an increasing data set on water ice toward

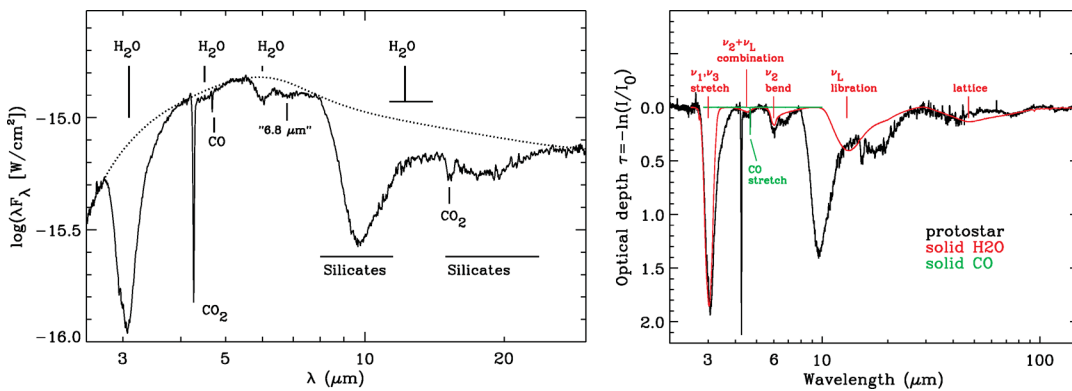


Figure 12. (Left) Detection of water ice at 3, 4.5, 6, and 11 μm along the line of sight toward the protostar Elias 29 obtained with the ISO-SWS. The dotted line indicates the source continuum that acts as the “lamp” against which the water ice bands are seen in absorption. (Right) Continuum-divided spectrum on an optical depth scale overlaid with a laboratory spectrum of H_2O ice at $T = 10 \text{ K}$ from Hudgins et al.⁸⁶ Reprinted with permission from ref 100. Copyright 2008 European Southern Observatory.

background sources^{101,102} (Figure 4). The latter situation allows pristine water ice to be probed, unaffected by heating or radiation from the protostar. Water ice has also been seen in the spectra of evolved stars^{103,104} and toward many sources in external galaxies.^{105–107} The observed ice spectra are generally consistent with compact amorphous water ice, although the actual interstellar ice porosity is poorly constrained.¹⁰⁸ Only few sources show the signature of crystalline water ice.^{109,110}

2.3. Electronic Transitions

The ground electronic state of water is nonlinear with a bond angle of 104.5° and O–H bond length of 0.95 Å. The molecule has C_{2v} symmetry with a molecular orbital configuration $1a_1^2 2a_1^2 3a_1^2 1b_1^2 1b_2^2$ making up the $\tilde{\chi}^1\text{A}_1$ state. Its dissociation energy to $\text{H} + \text{OH}$ is 5.1 eV. The first excited electronic state to which dipole-allowed transitions are possible is $\tilde{\Lambda}^1\text{B}_1$ [$1b_1 \rightarrow 4a_1(3s)$ excitation], which has a vertical excitation energy of 7.5 eV. Strong absorptions therefore do not start until ~ 7 eV (~ 1800 Å), well above the dissociation energy. The $\tilde{\Lambda}$ state does not have bound energy levels, however: absorption leads directly to dissociation (see section 3.1.3). Similarly, the next dipole-allowed excited state, the $\tilde{\beta}^1\text{A}_1$ state [$3a_1 \rightarrow 4a_1(3s)$ excitation] at 9.8 eV, is largely dissociative. Bound electronic states do not appear until higher energies and have largely Rydberg character in which a bonding electron is promoted to a hydrogen-like “diffuse” orbital such as the 4s orbital.

The water gas-phase absorption spectrum is well-known^{111–113} and is available from the MPI Mainz UV–Vis Spectral Atlas of Gaseous Molecules database¹¹⁴ at www.uv-vis-spectral-atlas-mainz.org. Figure 13 illustrates the H_2O ultraviolet absorption spectrum, including the ionization limit at 12.61 eV (983 Å). Since most of the excited electronic states are dissociative, this figure illustrates directly the photodissociation processes described further in section 3.1.3. Figure 14 compares the absorption spectrum of water ice with that of water vapor; the ice band is shifted to shorter wavelengths due to the slightly smaller dipole moment of water in the excited state leading to less favorable interactions with the neighboring water molecules.^{115,116} The EUV spectrum of H_2O excited by electron impact has been measured by Ajello.¹¹⁷

Searches for H_2O absorption into the $\tilde{\chi}^1\text{B}_1$ state around 1240 Å have been made for diffuse clouds,³⁶ but no lines have been detected. Similarly, no H_2O emission has yet been detected at UV wavelengths.

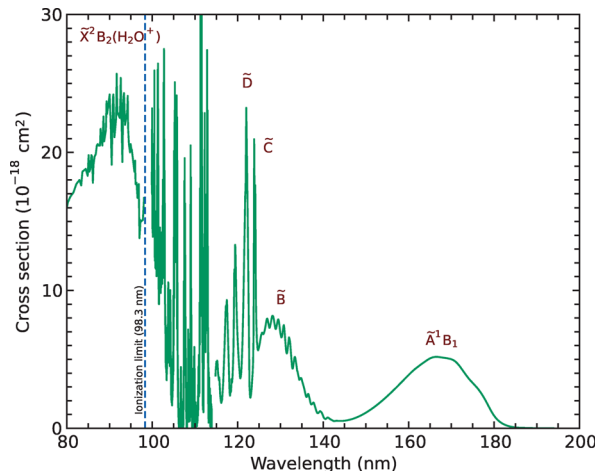


Figure 13. Absorption spectrum of gaseous H_2O starting from the $\tilde{\chi}^1\text{A}_1$ state. Photodissociation occurs mainly through the $\tilde{\Lambda}$ and $\tilde{\beta}$ electronic states. Figure produced using data from the ref 114.

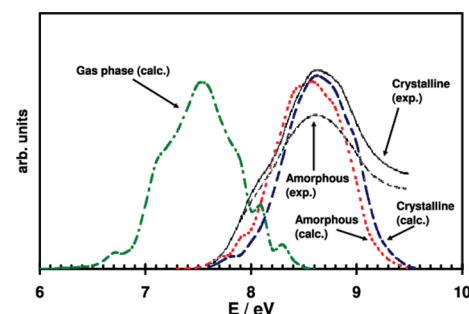


Figure 14. UV absorption spectrum of water ice compared with that of water vapor. Note the shift of the $\tilde{\Lambda} - \tilde{\chi}$ ice band to higher energies. Reprinted with permission from ref 115. Copyright 2008 European Southern Observatory.

2.4. Rate Coefficients for Inelastic Collisions

The most important collision partners of water in interstellar space are ortho- and para- H_2 , with electrons and H only significant in specific regions and He contributing at a low level. The only method to provide the thousands of state-to-state rate coefficients needed for astronomical applications is through theory. The process consists of two steps. First, a multidimensional potential energy surface describing the interactions

between the colliders has to be computed using state-of-the-art ab initio quantum chemical methods and fitted to a convenient representation for use in the dynamics. Second, the dynamics on this surface have to be calculated using inelastic scattering calculations at a range of collision energies. Full quantum calculations are used at low collision energies, whereas quasiclassical methods are often employed at the highest energies.

Early studies used simplifications such as replacing H₂ with He,¹¹⁸ including only a limited number of degrees of freedom of the colliding system (i.e., keeping some angles or internuclear distances frozen), or approximations in the scattering calculations.¹¹⁹ The most recent calculations have been performed on a 5 D potential surface and consider collisions of H₂O with both para-H₂ and ortho-H₂ separately.^{120,121} This 5 D potential is based on the full 9 D potential surface computed by Valiron et al.¹²² The rate coefficients for pure rotational transitions within $v = 0$ have been computed with the quantum close coupling method, even up to high energies, where such calculations become very computer intensive. Interestingly, the cross sections for collisions of ortho- and para-H₂O with ortho-H₂ are found to be significantly larger than those with para-H₂ for low J , so that explicit treatment of the ortho/para H₂ ratio in interstellar cloud models is important.

The quantum close coupling calculations performed to date have included the lowest 45 rotational states of both ortho- and para-H₂O. These include the states from which emission or absorption has been observed in the vast majority of astronomical observations. However, a few studies of astrophysical absorption¹²³ and emission^{68,71,124} probe states of even higher excitation (see Figure 9); here, extrapolation methods must currently be employed to estimate the collisional rate coefficients of relevance.^{125,126}

Direct comparison of absolute values of theoretical state-to-state cross sections with experimental data is not possible for water, but the accuracy of the 9 D potential surface and resulting rate coefficients has been confirmed implicitly through comparison with other data sets,^{127,128} including differential scattering experiments of H₂O with H₂¹²⁹ and the presence of weakly bound states.^{130–132} At higher temperatures (>80 K), the cross sections derived from pressure broadening data¹³³ agree with theory within 30% or better for low J . Overall, the uncertainty in the most recent cross sections obtained from full quantum calculations is estimated to range from a few tens of percent to a factor of a few, depending on the transition.¹³⁴

Several studies have investigated how the water model line intensities from interstellar clouds depend on the choice and accuracy of the collisional rate coefficients.^{134–136} For some transitions, such as the important $1_{10}-1_{01}$ 557 GHz line, the uncertainty in the intensity scales linearly with that in the cross section.¹³⁷ For higher-lying lines, the dependence is less direct due to optical depth effects and the possibility that infrared pumping contributes (see section 2.5). The difference between model intensities using the older quasiclassical trajectory results¹³⁸ and the new quantum rate coefficients^{120,121} is typically less than 50%, although some lines can show variations up to a factor of 3, especially at lower temperatures and densities. While substantial, these uncertainties generally do not affect astronomical conclusions. Altogether, the collisional rate coefficients have now reached such high accuracy that they are no longer the limiting factor in the interpretation of the astronomical water data. This conclusion is a testimony to the decade long effort by molecular physicists and quantum chemists to determine them.

For vibration–rotation transitions of water, much more limited information is available. A set of collisional rate coefficients derived from vibrational relaxation data has been published¹²⁵ but is accurate only to an order of magnitude. The same study also considers H₂O–electron rate coefficients. Little is known about H₂O–H collisional rate coefficients, which are important in some astrophysical regions, such as dissociative shocks.¹³⁹

Collisional rate coefficients for H₂O and for other astrophysically relevant species can be downloaded electronically from the BASECOL database¹⁴⁰ at www.basecol.obspm.fr and from the LAMDA database¹⁴¹ at home.strw.leidenuniv.nl/~moldata/.

2.5. Water Excitation and Radiative Transfer

The observed spectrum of interstellar water vapor, whether detected in emission or absorption, depends upon the relative populations in the various rovibrational states (the “level populations”). These, in turn, are determined by a complex interplay of collisional and radiative processes. Under conditions of thermal equilibrium (TE), the molecular motions are characterized by a Maxwell–Boltzmann distribution with a single kinetic temperature, T_{kin} , and the water molecules are bathed in a blackbody radiation field with a temperature T_{BB} equal to T_{kin} . Then the fractional population in any given rovibrational state, i , of energy, E_i , is determined purely by thermodynamic considerations and is given by the Boltzmann factor $f_i = \exp(-E_i/kT)/Q(T)$, where g_i is the degeneracy of the state and $Q(T) = \sum g_i \exp(-E_i/kT)$ is the partition function.

In the interstellar medium, however, the radiation field is typically far from equilibrium with the gas, and TE does not apply. Were this not the case, molecules would show no net emission or absorption of radiation and would therefore be undetectable. Nevertheless, if the gas density is sufficiently high, collisional processes can dominate radiative processes and the relative level populations can attain a state of “local thermodynamic equilibrium” (LTE), in which they are described by a Boltzmann distribution at a single temperature, T_{kin} .

Radiative rates scale with the dipole moment (μ_D) and transition frequency (ν) as $\mu_D^2 \nu^3$. Because water possesses a large dipole moment and a large rotational constant, its spontaneous radiative rates for dipole-allowed rotational transitions are relatively large compared, for example, to those of the commonly observed CO molecule ($\mu_D = 1.85$ vs 0.1 D and rotational constants 9–28 vs 1.9 cm^{-1}). Thus, except in very dense regions where stars are forming, the level populations typically show departures from LTE and a detailed treatment of the molecular excitation is needed. In this case, the level populations quickly reach a quasi-equilibrium in which each state is populated at the same rate as it is depopulated. The resulting populations can still be plotted in a Boltzmann diagram and fitted with a so-called excitation temperature T_{ex} or T_{rot} (if only rotational levels are involved), but T_{ex} has no physical meaning and can be very different from the kinetic temperature T_{kin} of the region.

The excitation of interstellar water vapor generally involves three types of processes: (1) collisional excitation and de-excitation, (2) absorption of—and stimulated emission by—the surrounding radiation, and (3) spontaneous radiative decay (see Figure 4). In the first of these processes, inelastic collisions with molecular hydrogen usually dominate; because the rate coefficients for excitation by ortho- and para-H₂ can differ substantially, the collisional excitation rates depend both upon the H₂ density and the H₂ ortho-to-para ratio (section 2.4). In environments where the electron fractional abundance exceeds

$\sim 10^{-4}$, electron impact excitation can also be important, provided the electron density is high enough for collisions to dominate over radiative excitation.

In the second of these processes (absorption and stimulated emission), the relevant radiation field includes both external continuum radiation and the line radiation emitted by nearby water molecules. A strong external radiation field, resulting from continuum emission from warm dust, for example, can lead to pumping of pure rotational transitions and vibrational pumping in a series of vibrational bands, particularly the $\nu_2 = 1 - 0$ band at $6.3 \mu\text{m}$. The effects of line radiation from nearby water molecules complicates the problem significantly, because the level populations of water molecules in one location affect those in another. Put another way, the equations of statistical equilibrium that determine the level populations at each point within an interstellar gas cloud must be solved simultaneously with the equations of radiative transfer that determine the radiation field at each point.

Several methods, of varying complexity, have been developed to solve the excitation problem described above. These include Monte Carlo simulations,¹⁴² iterative methods such as accelerated Lambda iteration (ALI),¹⁴³ hybrid methods, and escape probability methods,¹⁴⁴ in which the spontaneous emission of photons is assumed to be followed either by escape or local reabsorption. For media with a monotonic and large velocity gradient¹⁴⁵ (LVG), escape probability methods are preferred, as they are both accurate and computationally inexpensive; for static media, however, there is a trade-off between computational expense and accuracy. Publicly available computer programs that can be used to model the excitation of—and emission from—interstellar water vapor and other molecules include RATRAN¹⁴⁶ (a hybrid Monte Carlo/ALI code), LIME¹⁴⁷ (a code suited for arbitrary 3D geometries), and Radex¹⁴⁸ (an escape probability code).

In the absence of an external radiation field, the typical behavior of the water rotational level populations is that departures from LTE are most pronounced for the states of highest energy, as expected because the spontaneous radiative decay rates tend to increase with energy. A secondary effect is that the departures from LTE also increase with quantum number K_A . In this context, the set of states with lowest K_A (0 or 1) for given J are sometimes called the “backbone” states¹⁴⁹ (i.e., for ortho-water, the states $1_{01}, 2_{12}, 3_{03}, 4_{14}, 5_{05}, 6_{16} \dots$). These states tend to show the smallest departures from LTE because they possess the fewest routes for spontaneous radiative decay.

2.6. Masers

One fascinating consequence of the secondary behavior described above (i.e., the fact that the departures from LTE increase with K_A) is that radiative transitions with $\Delta J = J_u - J_l = 1$ and $\Delta K_A = +1$ between states of similar energy can exhibit a “population inversion”. Here, the population in the upper state, divided by its degeneracy, exceeds that for the lower state; as a result, the stimulated emission rate exceeds the absorption rate, leading to the maser phenomenon in which the intensity of the radiation along a given ray can increase exponentially. Indeed, the first water transition ever detected from the interstellar gas, the $6_{16} - 5_{23}$ transition near 22 GHz,¹³ exhibits strong maser action. Interferometric observations¹⁵⁰ of this transition reveal large luminosities emerging from maser spots of only $\sim 10^{13} \text{ cm}$ in size; typical brightness temperatures (defined as the temperature for which the Planck function yields an intensity equal to that observed) often exceed 10^{10} K and in

extreme cases¹⁵¹ can exceed 10^{15} K . Over the 40 years since the first detection of interstellar water maser emission in the 22 GHz transition, several additional maser transitions have been found at higher frequencies: these are listed in Table 3 and marked on

Table 3. Masing Transitions of Water Vapor

vibrational state	transition	frequency (GHz)	source type ^a	ref
ground	$6_{16} - 5_{23}$	22.235	ISM, CSE	Cheung et al. ¹³
ground	$3_{13} - 2_{20}$	183.310	ISM, CSE	Waters et al. ¹⁵⁵
ground	$10_{29} - 9_{36}$	321.226	ISM, CSE	Menten et al. ¹⁵⁶
ground	$5_{15} - 4_{22}$	325.153	ISM, CSE	Menten et al. ¹⁵⁷
ground	$4_{14} - 3_{21}$	380.197	ISM, CSE	Phillips et al. ¹⁵⁸
ground	$7_{53} - 6_{60}$	437.347	ISM, CSE	Melnick et al. ¹⁵⁹
ground	$6_{43} - 5_{50}$	439.151	ISM, CSE	Melnick et al. ¹⁵⁹
ground	$6_{42} - 5_{51}$	470.889	CSE	Melnick et al. ¹⁵⁹
ground	$5_{33} - 4_{40}$	474.689	CSE	Menten et al. ¹⁶⁰
ground	$5_{32} - 4_{41}$	620.701	ISM, CSE	Neufeld et al. ¹⁵²
ground	$5_{24} - 4_{31}$	970.315	CSE	Justtanont et al. ¹⁶¹
$\nu_2 = 1$	$4_{40} - 5_{33}$	96.261	CSE	Menten and Melnick ¹⁶²
$\nu_2 = 1$	$5_{50} - 6_{43}$	232.687	CSE	Menten et al. ¹⁶³
$\nu_2 = 1$	$1_{10} - 1_{01}$	658.006	CSE	Menten et al. ¹⁶³

^aISM, interstellar medium; CSE, circumstellar envelopes of evolved stars.

the energy level diagram shown in Figure 15.¹⁵² With the exception of the 621 and 970 GHz transitions, which were observed with the HIFI instrument on Herschel, and the 380 GHz transition, detected using the Kuiper Airborne Observatory, all the transitions listed in Table 3 can be observed from ground-based observatories.

In the case of interstellar water masers, the transitions observed to show maser action are precisely those for which population inversions are predicted¹⁵³ in the absence of an external radiation field. Many of the interstellar water masers are likely produced by collisional excitation in shocks¹³⁹ associated with forming stars.

Several additional maser transitions, observed in evolved stars but not the interstellar medium, are most likely pumped by continuum radiation. These circumstellar maser transitions include several transitions within the ν_2 vibrational band: here, maser action is apparently favored for $\Delta K_A = -1$. A possible pumping scheme has been discussed by Alcolea and Menten,¹⁵⁴ but further modeling is still needed to understand the excitation of vibrationally excited masers in circumstellar envelopes.

In addition to the intrinsic interest of the maser phenomenon, the 22 GHz transition has proven to be a powerful astronomical tool. For example, within the galaxy, the 22 GHz maser emission is used as a beacon to locate regions where massive stars are forming.¹⁶⁴ Masers have also been detected in many external galaxies, especially those with strong far-infrared fluxes.^{165,166} Thanks to their extraordinary brightness, 22 GHz water masers can be observed with very long baseline interferometry (VLBI), which can provide milliarcsecond resolution. Moreover, individual maser spots typically show very narrow linewidths, allowing accurate line-of-sight velocities to be inferred. Thus, VLBI observations enable proper motion studies of warm astrophysical gas and can provide geometric distance estimators, yielding the distances and motions of star forming regions in our galaxy and of circumnuclear disks in active galaxies.^{167,168} As noted in the Introduction, such observations have led to the best evidence yet obtained for the existence of supermassive black

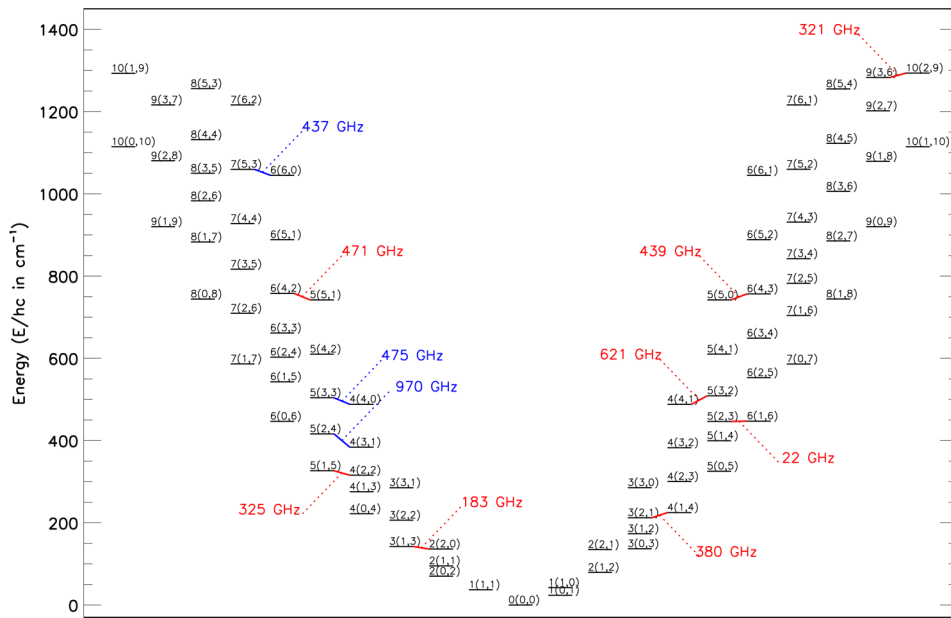


Figure 15. Energy level diagram showing water maser transitions detected to date. Red lines denote known interstellar water maser transitions, and blue lines denote transitions for which maser emission has been confirmed in evolved stars only. Reprinted with permission from ref 152. Copyright 2013 American Astronomical Society.

holes in external galaxies,¹⁴ as well as revised estimates for the size of the Milky Way.¹⁶⁹

3. WATER CHEMISTRY

Figure 16 presents an overview of the main reactions involved in the water chemistry. Three distinct synthetic routes are seen: (i) low-temperature ion–neutral chemistry ($\lesssim 100$ K), (ii) high-temperature neutral–neutral chemistry, and (iii) surface chemistry. In the following subsections, each of these types of chemistries will be discussed in detail. Throughout this section, s-X denotes a surface species.

3.1. Low-Temperature Ion–Neutral Chemistry

3.1.1. General Considerations. Ion–neutral chemistry is the dominant gas-phase chemistry in cold interstellar clouds, where the low temperatures limit the important reactions to those that are rapid, exothermic, and without activation energy barriers. Figure 16 shows the chain of ion–molecule reactions leading to water. Such reactions between ions and neutrals have strong long-range forces, leading to large rate coefficients for product channels without barriers.¹⁷⁰ For reactions in which the neutral has no permanent dipole moment, the long-range force normally consists of the attraction between the ionic charge and the dipole polarizability of the neutral. For such systems, a simple long-range capture model known as the Langevin model leads to a temperature-independent rate coefficient k_L ($\text{cm}^3 \text{s}^{-1}$) of¹⁷¹

$$k_L = 2\pi e\sqrt{\alpha/\mu} \approx 10^{-9} \quad (1)$$

where e is the electronic charge (esu), α is the polarizability (cm^3), and μ (g) is the reduced mass of the reactants. Typical values are $10^{-9} \text{ cm}^3 \text{s}^{-1}$. For neutral species with a permanent dipole moment like water, a somewhat more complex long-range capture approach shows that there is an approximately inverse dependence on the square root of temperature from roughly 10 to 300 K, which then gradually turns into the Langevin rate coefficient at higher temperatures. In the low-temperature limit, a theoretical approach, known as the trajectory scaling meth-

od^{170,172–174} yields an expression for the rate coefficient k_{TS} of

$$k_{TS}/k_L = 0.4767x + 0.6200 \quad (2)$$

in terms of a unitless parameter, x , which is given by the equation

$$x = \mu_D/(2\alpha kT)^{1/2} \quad (3)$$

Here μ_D (esu cm) is the dipole moment of the neutral reactant. In more common units, the dipole moment for water is 6.17×10^{30} C m (1.85 D). With a large dipole moment and an ion of low mass, e.g., H_3^+ , the predicted rate coefficient for ion–neutral reactions at 10 K can exceed $10^{-8} \text{ cm}^3 \text{s}^{-1}$. When the temperature is high enough that $x < 2$, another expression must be used for the rate coefficient:¹⁷³

$$k_{TS}/k_L = (x + 0.5090)^2 / 10.526 + 0.9754 \quad (4)$$

With this second expression, the ratio between the trajectory scaling and Langevin rate coefficients eventually approaches unity as the temperature is raised. A large compendium of ion–neutral reactions and rate coefficients measured at assorted temperatures (but rarely under 100 K) shows that the long-range capture models are often quite accurate, although they do not tell us anything about the product channels and their branching fractions.¹⁷⁵ In addition to ion–neutral reactions, low-temperature chemical processes do include selected neutral–neutral reactions involving at least one radical, because these processes possess no activation energy barrier and even have a weak inverse temperature dependence in their rate coefficient.¹⁷⁶

While ion–neutral reactions produce an assortment of molecular ions, both positively and, to a lesser extent, negatively charged, the final step in the production of neutral molecules like H_2O normally occurs via dissociative recombination reactions between positive molecular ions and electrons. The rate coefficients and products of these highly exothermic and rapid reactions have been studied via both benchtop experiments, viz., the flowing afterglow apparatus, and large-scale ones, viz., storage ring methods.^{177,178} The rate coefficients are typically 10^{-7} cm^3

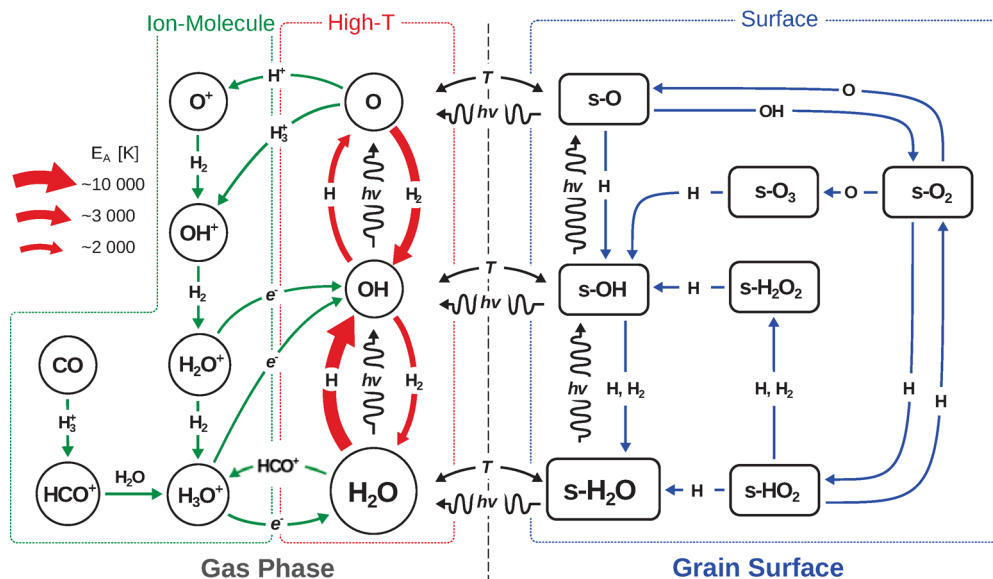


Figure 16. Summary of the main gas-phase and solid-state chemical reactions leading to the formation and destruction of H_2O . Three different chemical regimes can be distinguished: (i) ion–neutral chemistry, which dominates gas-phase chemistry at low T (green); (ii) high-temperature neutral–neutral chemistry (red); and (iii) solid-state chemistry (blue). $\text{s}-\text{X}$ denotes species X on the ice surfaces. Adapted with permission from ref 40. Copyright 2011 The University of Chicago Press.

s^{-1} at room temperature and vary with the inverse square root of temperature. Product channels are often dominated by significant dissociation, such as three-body channels (e.g., $\text{H}_3\text{O}^+ + \text{e} \rightarrow \text{OH} + \text{H} + \text{H}$) rather than breakage of just one bond.

Ions are produced by a variety of processes, with cosmic-ray ionization being the most universal because the cosmic rays, traveling near the speed of light with energies ranging upward of 1 MeV to more than 1 GeV, are able to penetrate large column densities of material, as discussed in section 1. The energy spectrum of cosmic rays cannot be fully determined by measurements above the Earth, however, because the solar wind and the Earth's magnetic field interfere with the low-energy flux, which is the most important for ionization, since the cross section for ionization depends inversely on the translational energy of the cosmic rays.^{179–181} Using estimates for the low-energy flux in unshielded interstellar space and the penetration efficiency in diffuse and dense sources, combined with chemical simulations, the first-order rate coefficient ζ_{H} for ionization of atomic hydrogen directly by cosmic rays and secondarily by electrons produced by cosmic-ray bombardment is found to be as high as 10^{-15} s^{-1} in diffuse clouds and at the edge of denser sources.^{182,183} The value of ζ_{H} is reduced to less than 10^{-16} s^{-1} deeper into the cloud by $A_{\text{V}} = 10$ mag, and eventually drops to $\sim 10^{-17} \text{ s}^{-1}$ in the interior of dense clouds.^{179,184} Propagation effects associated with Alfvén waves (a magnetohydrodynamic phenomenon) can also play a role in excluding cosmic rays from dense cloud interiors, even for somewhat smaller shielding column densities.

3.1.2. Low Temperature Gas-Phase Formation of H_2O .

The ion–neutral synthesis of gaseous water commences with the formation of molecular hydrogen on the surfaces of dust particles (see section 3.3), after which H_2 is either ejected immediately or sublimates within a short period, even at temperatures as low as 10 K.^{185–190} The formation of H_2 occurs with high efficiency even in diffuse clouds. Indeed, in some diffuse clouds with $A_{\text{V}} < 1$ mag, approximately half of the hydrogen has already been converted from atoms to molecules.¹⁹¹ Ionization of H_2 by cosmic-ray protons and secondary electrons occurs with a first-

order rate coefficient $\zeta_{\text{H}_2} \approx 2\zeta_{\text{H}}$ and leads primarily to the hydrogen ion, H_2^+ , and electrons.¹⁷⁹ Other products include¹⁹² H , H^+ , and even H^- .

Once H_2^+ is produced, it is rapidly converted into the triatomic hydrogen ion by reaction with ubiquitous H_2 :



with a near-Langevin rate coefficient¹⁷⁵ of $(1.7\text{--}2.1) \times 10^{-9} \text{ cm}^3 \text{ s}^{-1}$. At an H_2 gas density of 10^4 cm^{-3} , the time scale between reactive collisions with H_2 is then 14 h, which is a short time in astronomical terms. The H_3^+ ion does not react with H_2 but is destroyed more slowly by reaction with electrons (time scale about 50 yr) and with a variety of abundant neutral atoms and molecules.^{193,194} Reaction with atomic oxygen leads mainly to the transitory OH^+ ion at an overall rate coefficient of $1.2 \times 10^{-9} \text{ cm}^3 \text{ s}^{-1}$, with a product branching fraction of 0.70, and to the water ion, with a branching fraction of 0.3:¹⁷⁵

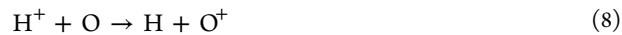


The hydroxyl ion reacts rapidly with H_2 to form the water ion



which then reacts with H_2 to form the saturated hydronium ion (H_3O^+) + H . Although the ions OH^+ and H_2O^+ are removed rapidly by reaction with H_2 , there are many sources in which these ions can be detected as long as the clouds have a relatively high H/H_2 fraction^{195–201} (see section 4.1).

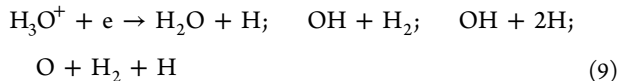
The sequence of reactions leading to the hydronium ion can also start with protons, which undergo a slightly endothermic charge transfer reaction with oxygen atoms²⁰²



after which a reaction with H_2 leads quickly to OH^+ and H . The charge exchange route is more efficient in diffuse clouds where at least 50% of the hydrogen is in the form of atoms and the temperature is high enough (50–100 K) that the weak endothermity of 226 K can be overcome. The range of

measured values¹⁷⁵ of the rate coefficient at 300 K is $(6.0\text{--}6.8) \times 10^{-10} \text{ cm}^3 \text{ s}^{-1}$. Computed values are up to a factor of 2 lower at this temperature.²⁰³

The hydronium ion is destroyed principally by dissociative recombination with electrons. Although the rate coefficient at low temperatures is very large, the fractional electron abundance with respect to hydrogen in cold dense clouds of $10^{-7}\text{--}10^{-8}$ is so low that the overall rate of reaction is not rapid. Nevertheless, it is this reaction that leads to water as well as to OH and possibly O:



A number of experiments have been undertaken on this system,^{204–207} and the currently accepted values for the overall rate coefficient as a function of temperature and the product branching fractions derive from storage ring experiments, the most recent in Heidelberg.²⁰⁵ The branching fractions from this experiment (on D_3O^+) in the low-temperature limit are 0.165 ($\text{D}_2\text{O} + \text{D}$), 0.125 ($\text{OD} + \text{D}_2$), 0.71 ($\text{OD} + \text{D} + \text{D}$), and 0.0 ($\text{O} + \text{D}_2 + \text{D}$). These values are in excellent agreement with an earlier storage ring study in Stockholm²⁰⁶ but somewhat less so with an earlier result from a storage ring in Aarhus²⁰⁴ and a flowing afterglow study.²⁰⁸ The Stockholm group found no isotopic effect, so the Heidelberg results can be used for H_3O^+ . Note that water is not the major product channel in any of these experiments.

The destruction of gaseous water is mainly by reactions with abundant ions such as H_3^+ , HCO^+ , C^+ , H^+ , and He^+ . With its dipole moment of 1.85 D, the ion–neutral rate coefficients at low temperatures are considerably greater than the Langevin value. The measured value¹⁷⁵ for the reaction with H_3^+ at room temperature, 300 K, is $5 \times 10^{-9} \text{ cm}^3 \text{ s}^{-1}$, and the estimated value using the trajectory scaling model is also this value. At a temperature of 10 K, the predicted rate coefficient would be approximately a factor of 4.6 greater. The reactions of water with protonating ions, e.g., H_3^+ and HCO^+ , lead to H_3O^+ , but dissociative recombination leads to species other than water on 83.5% of collisions, so the processes are not cyclic in the main and do lead to the destruction of water with a high efficiency. The balance between formation and destruction of water in dense clouds leads to a prediction¹⁷⁶ of a small fractional abundance of water of 10^{-8} to a few $\times 10^{-7}$ in pure gas-phase models. This is consistent with observations of diffuse and translucent clouds but considerably greater than what is observed in cold dense clouds (see section 4.1).

3.1.3. H_2O Photodissociation. Destruction of neutrals such as water can occur not only by ions but also via photoinduced processes. The photodissociation of H_2O in the gas phase has been very well studied, both experimentally^{111–113,208,209} and theoretically.^{210–213} Many of the excited electronic states of water are dissociative, i.e., the potential is either fully repulsive, leading to direct dissociation, or the potential is bound in one direction but dissociative in another direction. Alternatively, a bound state can couple with a potential surface of another symmetry leading to predissociation. For the interstellar radiation field, the photodissociation is dominated by absorption into the $\tilde{\text{A}}$ state, which dissociates into $\text{H} + \text{OH}$ in the electronic ground state, $\text{X}^2\Pi$ (see Figure 13). The OH molecules are produced with low rotational excitation but with considerable vibrational excitation, which increases with photon energy.²¹³ At the experimental energy of 7.87 eV (1576 Å), close to the peak

absorption energy, the distribution^{214,215} over $v = 0, 1, 2, 3$, and 4 levels of OH is 1.00:1.11:0.61:0.30:0.15.

Photodissociation through the $\tilde{\text{B}}$ state is important at higher photon energies, including Lyman α at 1216 Å. In this case, the OH is produced not only in the ground state but also for a small fraction in the excited electronic $\text{A}^2\Sigma^+$ state. The OH A state will rapidly decay radiatively to the X state. The OH is produced vibrationally cold, with the $\text{X}^2\Pi$ $v = 0, 1, 2, 3$, and 4 populations scaling as $\sim 0.60:0.10:0.09:0.08:0.07$, with the fractions only weakly dependent on photon energy.^{208,105} In strong contrast with the $\tilde{\text{A}}$ state, the photodissociation of water through the $\tilde{\text{B}}$ state produces OH molecules with very high rotational excitation, with levels up to $J = 70/2$ populated for $v = 0$. The precise J values depend sensitively on the energy above the OH(X) or OH(A) threshold. Specifically, there is a strong preference for populating the highest rotational product state for which the rotational barrier energy is lower than the available photon energy, the so-called “single J phenomenon” observed experimentally.^{217,218} In section 4.5, specific interstellar regions will be discussed where OH is produced prominently through this channel and where the “prompt emission” of highly rotationally excited OH is observed.

A small fraction of absorptions into the higher electronic states of H_2O can also lead to the $\text{O} + \text{H}_2$ or $\text{O} + \text{H} + \text{H}$ products.^{111,208,218} For the general interstellar radiation field, the overall fraction is about 10% compared with the $\text{H} + \text{OH}$ products.

There are two different treatments for translating the cross sections into photodissociation and photoionization rates to be used in astrochemical models. The first is for radiation that originates external to the source and can penetrate significantly, such as in diffuse interstellar clouds and dense PDRs. Here the rate (s^{-1}) as a function of depth A_V into the cloud is often fit to the expression^{48,219}

$$k_{\text{pd}} = \alpha \exp(-\gamma A_V) \quad (10)$$

where A_V is the visual extinction, α is related to the strength of the radiation field in the absence of extinction as well as the absorption cross sections to the appropriate excited electronic states (Figure 13), and γ is a unitless parameter that takes into account the extinction at shorter wavelengths than the visible, which are particularly important for photodestruction. For gaseous water in the unshielded average interstellar radiation field,⁴³ the photodissociation parameter for the production of OH and H is²²⁰ $\alpha = 8.0 \times 10^{-10} \text{ s}^{-1}$, whereas the depth dependence is given by $\gamma = 2.20$. See www.strw.leidenuniv.nl/~ewine/photo for more information. For clouds exposed to more intense radiation, this rate is scaled by a factor of χ .

In dense regions shielded from stellar radiation, there is still a remnant UV radiation field caused by secondary electrons produced by cosmic-ray bombardment, mainly of molecular hydrogen in the gas, as discussed in section 1.4. The photodissociation rate (s^{-1}) for this radiation source is fit to the expression⁵²

$$k_{\text{pd}} = \zeta_{\text{H}_2} A / [C_{\text{ext}}^{\text{H}}(1 - \omega)] \quad (11)$$

where the cosmic-ray ionization rate ζ_{H_2} (s^{-1}) inside dense clouds is on the order of $10^{-17}\text{--}10^{-16} \text{ s}^{-1}$, $C_{\text{ext}}^{\text{H}}$ is the dust extinction cross section per H atom in cm^2 , ω is the dust albedo at UV wavelengths with a typical value of 0.5, and A contains the integral of the molecular photodissociation cross sections with the cosmic-ray-induced spectrum. For water, the rate is

calculated⁵² to be $970\text{--}980 \zeta_{\text{H}_2} \text{s}^{-1}$ for the production of OH and H.

The role of X-rays in the destruction of water and other neutrals can also be important in regions near sources that produce copious amounts of X-rays, such as near the midplane of protoplanetary disks around cool T Tauri stars²²¹ and the inner envelopes around low-mass protostars.²²²

3.2. High-Temperature Gas-Phase Chemistry

As gas-phase temperatures rise from the 10 K value of cold cores, the relative importance of endothermic reactions and exothermic reactions with activation energy increases. The subject has been looked at anew by Harada et al.²²³ Among the most important of such reactions are those between neutral species and H₂, the most abundant gas-phase molecule. The first reactions of this type to "turn on" involve radicals or atoms. For the case of water production, the two key reactions of this type are



and



Both of these reactions have been studied by many groups, and there are theoretical and experimental studies in assorted temperature ranges, as well as critical reviews of the literature.^{193,224} The rate coefficients determined from the data are typically fit to a modified Arrhenius form with three parameters:

$$k(T) = \alpha(T/300 \text{ K})^\beta \exp(-\gamma/T) \quad (14)$$

The 1992 review by Baulch et al.²²⁴ was a careful study of the existing literature at the time; a rate coefficient $k (\text{cm}^3 \text{ s}^{-1})$ for reaction 12 of $3.44 \times 10^{-3}(T/300)^{2.67} \exp(-3160/T)$ was suggested for the temperature range 300–2500 K. This reaction is endothermic by roughly 900 K (1 kcal/mol = 503 K) but has a much larger barrier, more precisely a value for γ of 3160 K. At a temperature of 300 K, the recommended rate coefficient is $9.2 \times 10^{-18} \text{ cm}^3 \text{ s}^{-1}$. A more recent theoretical value of $7.1 \times 10^{-18} \text{ cm}^3 \text{ s}^{-1}$ was computed²²⁵ for a temperature of 300 K, in reasonable agreement with the recommended value. If one compares the rate of the reaction per O atom ($k_{12}n(\text{O})$) with the analogous rate for the initial reaction for the ion–molecule synthesis ($\text{O} + \text{H}_3^+$), the $\text{O} + \text{H}_2$ rate becomes roughly equal to the ion–molecule rate at 300 K with a typical fractional abundance of 10^{-8} for H₃⁺ with respect to H₂ in dense clouds. At a somewhat lower abundance of H₃⁺, the temperature at which the neutral–neutral reaction dominates²²⁶ is somewhat lower, such as 230 K. At temperatures higher than 300 K, the neutral–neutral mechanism certainly dominates, if the OH product then continues efficiently to water by reaction 13. More recent experiments for reaction 12 have mainly studied the high-temperature limit (>1000 K). For example, if the high temperature studies of Javoy et al.²²⁷ are extrapolated down to 1000 K, a rate coefficient for $\text{O} + \text{H}_2$ of $\sim 9 \times 10^{-14} \text{ cm}^3 \text{ s}^{-1}$ is obtained, whereas the recommended value of Baulch et al. is $4 \times 10^{-13} \text{ cm}^3 \text{ s}^{-1}$. In summary, the 1992 recommended value still seems to be reasonable over a wide range of temperatures relevant for interstellar applications.

Regarding the reaction of OH + H₂, which is highly exothermic but possesses a considerable barrier, the most recent review recommends a rate coefficient of $7.7 \times 10^{-12} \exp(-2100/T) \text{ cm}^3 \text{ s}^{-1}$ over the temperature range 200–450 K,²²⁸ with a 300 K value of 6.7×10^{-15} . The 1992 critical review of Baulch et al. recommends a value over the temperature range 300–2500 K of

$1.55 \times (T/300)^{1.60} \exp(-1660/T) \text{ cm}^3 \text{ s}^{-1}$, leading to a rate coefficient of 6.1×10^{-15} at room temperature. Both of these rate coefficients are smaller than the one from the expression adopted by Harada et al.²²³ [$k = 8.40 \times 10^{-13} \exp(-1040/T)$]. The rate coefficients must be compared with those for other competitive reactions of OH with abundant species, such as OH + O, to determine the efficiency of the neutral–neutral reaction route to water. At room temperature, the latter reaction has a rate coefficient²²⁸ of $3.5 \times 10^{-11} \text{ cm}^3 \text{ s}^{-1}$. When multiplied by a standard O atom fractional abundance with respect to H₂ of 10^{-4} , one gets a rate per OH of $3.5 \times 10^{-15} \text{ cm}^3 \text{ s}^{-1}$, somewhat smaller than the rate per OH of the OH + H₂ reaction. Thus, it is likely that the neutral–neutral reactions leading to water formation in the gas-phase dominate at room temperature and above.

When the H₂ reactant is excited to its $v = 1$ vibrational state, as is the case in the outer layers of dense PDRs and disks (section 4), the rate coefficients of both reactions 12 and 13 are known to increase by orders of magnitude at 300 K, since the vibrational energy is sufficient to overcome the barrier if it is useable for that purpose.^{225,229,230} Moreover, much of the excess energy becomes vibrational energy of the product.

Depending on the H/H₂ ratio in the gas, the back reactions of eqs 12 and 13 can of course also occur and drive water back to oxygen. Under most astrophysical situations, however, the forward reactions dominate because of the higher activation energies involved (Figure 16).

The neutral–neutral reaction network that forms water is particularly important in shocks^{231,232} (see section 4.4.1). Following the passage of shock waves, the internal energy of the water molecules relaxes much more quickly than the translational energy, so that the situation is a distinctly nonthermal one ($T_{\text{rot}} \ll T_{\text{kin}}$). In such situations, the use of state-selective rate coefficients according to the actual water excitation, rather than thermally averaged rate coefficients, would be more appropriate, although this is seldom done (see Balakrishnan²²⁵ for the effect on the O + H₂ reaction).

3.3. Ice Chemistry

3.3.1. General Considerations. For most sources other than those at high temperatures, it is important to include the chemistry that occurs on dust grains, especially for water. Surface chemistry is coupled to the gas-phase chemistry via accretion and desorption processes, the latter both thermal and nonthermal. Thermal desorption is another term for sublimation, while nonthermal processes include photodesorption, which has recently been studied in the laboratory and through classical molecular dynamics simulations (see below).

Technically, the term sublimation refers to solid to gas conversion under complete equilibrium conditions, where both desorption and accretion occur at equal rates. Thermal desorption refers to desorption from a surface that occurs into a vacuum. Since desorption always occurs in competition with accretion under astrophysical conditions, we use primarily the term sublimation to describe the solid–gas transition. The term thermal desorption is normally used to describe temperature-programmed desorption experiments in the laboratory.

In addition to the formation of H₂, low-temperature grains provide the surfaces for reactions that form water ice and a number of other ices, with methanol the most complex yet observed.^{98,235} Since water is the dominant observed ice in dense interstellar clouds and protostellar regions, the chemistry of its formation has been studied extensively. Direct accretion from the gas in dense regions can only explain the abundance of CO ice

among the dominant interstellar ices. So, ice chemistry is needed to convert abundant accreting species such as oxygen atoms into water. As depicted in Figures 16 and 17, three well-studied major

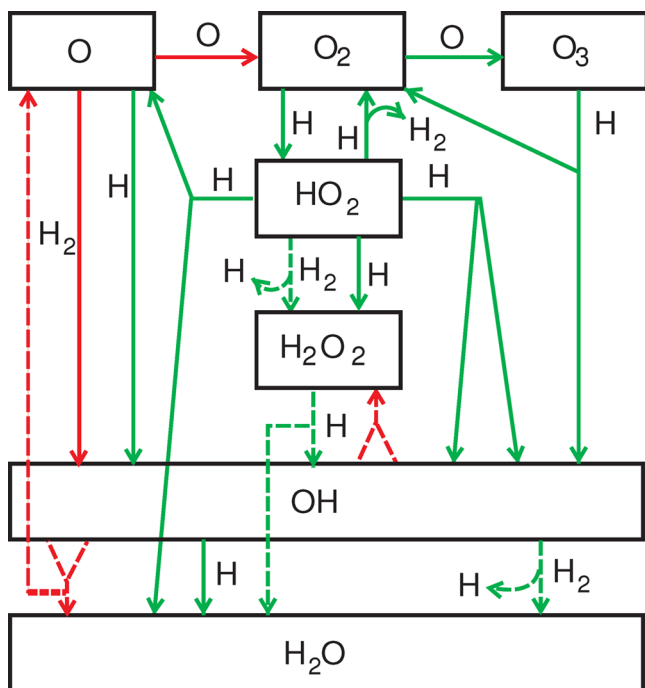


Figure 17. Schematic representation of the surface chemistry reaction network leading to the formation of water ice, based on Cuppen et al.²³³ and Lamberts et al.²³⁴ Green arrows refer to reactions that have been characterized by experiments or through simulations of experimental data. Red arrows refer to reactions that have not yet been studied experimentally or for which the experimental data are inconclusive. Four cases are distinguished: (i) efficient, effectively barrierless (<500 K) reactions (green), (ii) reactions with a barrier above 500 K (dashed-green), (iii) reactions not studied experimentally (red), and (iv) reactions studied experimentally but for which results are inconclusive (red-dashed).

routes exist for the low-temperature formation of water ice,⁸ the simplest of which is the hydrogenation of atomic oxygen, with more complex routes starting from s-O₂ and s-O₃. Both of these molecular species are formed via surface reactions, in which s-O atoms associate. Hydrogenation occurs via reaction of the oxygen species with atomic hydrogen. In addition to this hydrogenation route, a new study indicates that water ice can also be formed by the reaction of s-OH and s-H₂ on grains via a tunneling process,²³⁶ even though it has a barrier of 2100 K.

At low temperatures, the dominant mechanism for reactions on surfaces is thought to be the so-called Langmuir–Hinshelwood (LH) process, in which surface species, bound only by weak “physisorption” forces, diffuse among so-called lattice sites of minimum potential energy either by a classical random walk or by tunneling under barriers between sites. Unlike the gas phase, the dominant reactions on surfaces and ices, as they build up, are association reactions ($A + B \rightarrow AB^* \rightarrow AB$) in which rapid energy transfer from the complex (AB^*) to the grain allows the complex to stabilize. For cold grains, only the most weakly bound species, such as atomic hydrogen and oxygen, can diffuse, whereas at temperatures above 20–30 K, the more volatile heavier species begin to diffuse and desorb thermally. The LH mechanism can be modeled by rate equations similar to those for

the gas-phase chemistry, in which the rate coefficients are related to the rate of diffusion of both reactant partners.

It is important to distinguish the chemistry that occurs on bare surfaces (silicates and amorphous carbon) from the chemistry that occurs on ice layers that build up in cold dense sources. If most of the available oxygen is converted to water ice, the number of water ice monolayers on each grain becomes on the order of hundred. For such thick layers, the underlying grain surface does not matter anymore for the chemistry. Note also that ice chemistry can occur not only on the surface but also in layers under the topmost one, where both bulk diffusion and chemistry in pores can be competitive. For these lower layers, a simple LH mechanism such as described below may not be relevant, and other possibilities have been suggested, such as the swapping in position of nearby species.²³⁷

To discuss the water chemistry that occurs on the surfaces of ice mantles of interstellar grains, we first need to consider rate coefficients for accretion onto the grains and desorption from them as well as those for assorted chemical processes. In the following discussion, we use upper case K for the rate coefficients involving grains to distinguish them from gas-phase rate coefficients. Unless stated to the contrary, we will use concentration units of number of species per dust particle for adsorbed species. More normal units for laboratory processes are monolayers and areal concentrations. With these conventions, the first-order accretion rate coefficient for a given gas phase species, K_{acc} (s^{-1}), is given by

$$K_{\text{acc}} = \xi \sigma_d v \quad (15)$$

where ξ is the efficiency of sticking, σ_d is the grain cross section, and v is the thermal velocity of the accreting species A. The accretion rate (s^{-1}) for the number of species A per grain is then the product of this rate coefficient and the gas-phase concentration of A, $n(A)$. Other units for the accretion rate of species A are easily obtained. If it is desired to express the accretion rate in terms of areal concentration per second ($\text{cm}^{-2} \text{s}^{-1}$), then the rate coefficient must be multiplied by $n(A)$ and also divided by the surface area of the grain. To convert this expression to monolayers per second, one must divide the expression for the rate in areal concentration per second by the lattice site density, N , which lies in the vicinity of 10^{15} cm^{-2} , depending upon the surface.¹⁸⁷ Finally, if it is desired to determine the volume rate of accretion, for use in gas–grain chemical simulations of interstellar sources, one must multiply the rate coefficient by both the concentration of species A and the grain concentration. The sticking efficiency ξ is normally estimated from the theoretical expression of Hollenbach and Salpeter¹⁸⁵ and has been studied explicitly for H on water ice by molecular dynamics simulations.^{238,239} It varies strongly with temperature but is close to unity at 10 K.

The thermal desorption/sublimation rate coefficient, K_{subl} (s^{-1}), is given by the first-order Wigner–Polanyi equation¹⁷⁰

$$K_{\text{subl}} = \nu \exp(-E_D/k_B T) \quad (16)$$

In this expression, ν is the so-called trial frequency, which corresponds roughly to the frequency of vibration of a physisorbed molecule such as water trapped in a lattice site ($\sim 10^{12} \text{ s}^{-1}$), and k_B is the Boltzmann constant, while E_D is the desorption energy, or energy needed to remove a water molecule from the ice into the gas phase. The desorption energy of course depends on the ice or bare surface from which desorption occurs. For a water molecule on an ice dominated by water, a commonly used value based on laboratory studies¹⁹ is $E_D/k_B \approx 5600–5700$

K, where this relatively high value for a physisorbed species is caused at least in part by hydrogen bonding.

Nonthermal desorption mechanisms include photodesorption, desorption following chemical reaction, and cosmic-ray-induced desorption. The photodesorption rate coefficient is normally reported in terms of an efficiency per incident photon ($\sim 10^{-3}$) multiplied by the flux ($\text{cm}^{-2} \text{s}^{-1}$) of photons in the far-UV portion of the spectrum striking a grain. To achieve units of molecules s^{-1} , the product must be divided by the site density of the surface ($\sim 10^{15} \text{ cm}^{-2}$). The overall rate of photodesorption per grain would then be obtained by multiplying the rate coefficient by the number of molecules on the surface or within a few monolayers of the surface. Laboratory experiments with monochromatic light sources indicate that photodesorption can either be a discrete or continuous process, depending upon the excited electronic state of the adsorbate initially excited. Water ice provides an example of a continuous process²⁴⁰ (see Figure 14), whereas CO ice provides an example of a mainly discrete one.²⁴¹

Other mechanisms for nonthermal desorption have been less explored. Nevertheless, the results of a very recent laboratory study of the surface reaction between s-D and s-OD, which produces deuterated water on grains, indicates that more than 90% of the product is released into the gas phase,²⁴² although this fraction depends strongly on the underlying surface. This high percentage does not hold universally for other reactions, however, and the details of so-called reactive or chemical desorption are not well understood.

It is normally assumed that the photodissociation rate for ice species is the same as for the gas, unless there is strong evidence to the contrary, as does occur for water ice¹¹⁶ (Figure 14). Also, unlike photodesorption, which is mainly a surface to near-surface process,^{115,240} photodissociation can occur throughout the entire ice mantle up to ~ 100 monolayers. For water ice, a small photoionization channel leading to H_2O^+ in the gas is not included in ice models, but is added to the s-OH + s-H production channel because it is assumed that the newly formed ion will undergo dissociative recombination on the negatively charged grain surface. Photodissociation can be followed by reactive desorption if the products are reactive radicals. For example, the photodissociation products s-OH + s-H produced in the top ice layers can recombine to form water once again, with a fraction being ejected from the surface (see section 3.3.3).

The LH diffusive rate coefficient is based on the site-to-site hopping rate K_{hop} to a nearest neighbor site, which is similar to the sublimation rate, except that the diffusive barrier E_b takes the place of the desorption energy, viz.,

$$K_{\text{hop}} = \nu \exp(-E_b/k_B T) \quad (17)$$

where ν is once again the trial frequency. The rate coefficient is first-order and is used as written with concentration units of molecules per grain. In some treatments, tunneling under the diffusion barrier is included for atomic hydrogen.¹⁸⁹ The diffusion rate equivalent to a journey over an entire grain, K_{diff} , is just the hopping + tunneling rate divided by the number of lattice sites on the grain, N . The LH rate coefficient for the reaction between, e.g., s-OH and s-H is obtained by calculating the rate at which the two diffusing reactants find themselves in the same lattice site.¹⁹⁴ For reactions without chemical activation energy, the reaction is then assumed to occur instantaneously, whereas for reactions with chemical activation energy, a factor $\kappa < 1$ is included to take into account the more rapid of the two

processes of tunneling under the activation barrier (transition state) or hopping over it.

The overall expression for K_{LH} for the surface reaction between s-OH and s-H is then given by

$$K_{\text{LH}} = \nu \kappa (K_{\text{diff}}(\text{s-H}) + K_{\text{diff}}(\text{s-OH})) \quad (18)$$

if the units for the concentration of s-OH and s-H are numbers of species per grain. Other possible units, which will involve an additional factor in the expression for the LH rate coefficient, include monolayers per grain and actual volume concentrations, which requires knowledge of the volume concentration of grains. For the radicals OH and H, $\kappa = 1$, while for the reaction s-OH + s-H₂ \rightarrow s-H₂O + s-H, another pathway to form water, $\kappa < 1$ because of the chemical activation energy.²³⁶ It should be noted that the role of activation energy for surface reactions differs from that in the analogous gas-phase process, both because the actual values need not be the same and because for the surface process there is a competition involving the two types of barriers, diffusive and chemical. Thus, if the diffusion barrier is higher than the chemical barrier, the two reactants will have many chances to hop over or tunnel under the chemical barrier before they diffuse away. An analogous process in a gas-phase reaction involves a long-lived complex, which is trapped statistically.

It is important to realize that the above formulation ignores the option of the direct (Eley–Rideal) process, in which the reactant lands on top of the surface molecule, or the “hot atom” processes in which the reactant reaches the surface with extra translational energy. More general limitations of the above formulation are discussed in section 3.4.3.

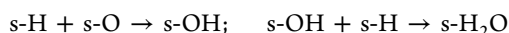
Although relevant laboratory experiments on the buildup of ices such as water on cold surfaces have been undertaken increasingly in the past decade, it is still the case that very few quantitative studies of actual rate coefficients are available.¹⁷⁰ The experiments typically deposit several layers of one of the reactants on a cold substrate (around 10–30 K) and then bombard the ice with the second reactant, usually atomic H or O. The reaction is then monitored *in situ* through infrared spectroscopy of the products in the ice. For example, in experiments of O₂ ice bombarded by H-atoms,²⁴³ the 3 μm features of H₂O₂ and H₂O appear after minutes (for a typical H-atom flux of $\sim 10^{13} \text{ atoms cm}^{-2} \text{s}^{-1}$) and the signal saturates after a few hours. Reaction rates can then be derived from these growth curves, depending on temperature and other experimental parameters. Reaction products can also be probed through temperature-programmed desorption experiments, in which the ice is heated up after a certain reaction period and products are measured using mass spectroscopy as they come off the ice.

Unlike gas-phase experiments, however, the transfer of even such quantitative laboratory data to interstellar conditions is not simple. The difference in time scales, for example, between laboratory (hours) and interstellar processes (up to 0.1 Myr) can lead to difficulties in interpretation.²⁴⁴ Rather than reaction rates, full microscopic modeling of the experiments is needed to infer basic molecular parameters such as binding energies E_D and diffusion barriers E_b , but such modeling has been done only in a few cases.^{234,245} Diffusion barriers E_b are particularly difficult to determine and so are usually simply taken to be a fraction of E_D in the models. Thus, the rate coefficients for surface/ice processes found in papers in the astrochemical literature have considerable uncertainty.

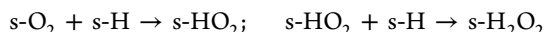
3.3.2. Water Ice Formation. With this background, we can look more closely at the various approaches to the formation of

interstellar water ice (Figure 17). The mechanisms discussed below have been recent subjects of experimental study.^{234,243,246–250} We maintain the assumption that the formation of water ice occurs via diffusive (Langmuir–Hinshelwood) reactions, but we are aware of the possibility that the chemistry on an ice mantle is far more complex than this simple diffusive approach, as noted above. With these reservations, we discuss the studied mechanisms below, originally put forward by Tielens and Hagen⁸ before much experimental evidence existed.

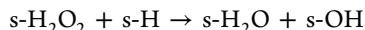
- Mechanism 1, starting from O: In this series of reactions, both atomic H and atomic O accrete onto a grain, diffuse toward one another, and form the radical OH. A second H atom lands on the grain and diffuses to the OH to form water:



- Mechanism 2, starting from O₂: This mechanism starts with the diffusive formation of molecular oxygen, s-O + s-O → s-O₂. The molecular oxygen can then add atomic H twice to form the s-HO₂ radical and then s-H₂O₂:



It is also possible for the second step to occur with molecular rather than atomic hydrogen, although the amount of H₂ on or in the ice mantle is poorly determined. Moreover, the reaction between s-HO₂ and s-H₂ may have an activation energy barrier. Once hydrogen peroxide is produced, it can react with atomic hydrogen to form s-OH and s-H₂O:



The newly formed s-OH can react with s-H to once again form s-H₂O. Similarly, s-HO₂ + s-H can lead to 2 s-OH, which can react further to s-H₂O.

- Mechanism 3, starting from O₃: Once s-O₂ is produced, addition of another surface/ice oxygen atom can produce ozone. The ozone can then react with s-H to form s-OH + s-O₂, followed by reaction of s-OH with s-H to form water, as already discussed.

- Mechanism 4, use of H₂: The reaction between s-OH and molecular hydrogen to form water and H is controversial.²⁵¹ There is a newly measured rate coefficient that suggests that the reaction can occur via tunneling, although this reaction possesses considerable activation energy in the gas-phase.²³⁶

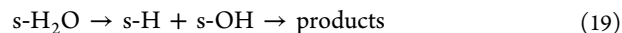
The role of mechanisms 1, 2, and 4 have been compared by Cuppen and Herbst²⁵² under a variety of physical conditions in the interstellar medium. Under diffuse and translucent cloud conditions ($A_V \leq 3$ mag; $n_H \leq 10^3 \text{ cm}^{-3}$), mechanism 1 dominates, although little water ice is produced due to efficient photodesorption of all grain surface species. The controversial reaction between s-OH and s-H₂ (mechanism 4) becomes important under the conditions of cold dense cores ($A_V \leq 10$ mag; $5 \times 10^3 \leq n_H \leq 5 \times 10^4 \text{ cm}^{-3}$) if it occurs at all. In the models of Cuppen and Herbst,²⁵² mechanism 2 occurs at the 20% level for dense cores, but Ioppolo et al.²⁴³ and Du et al.²⁵³ find mechanism 2 to be of at least comparable efficiency based on new experiments and models. Of course, these results are very model dependent, since, for example, the amount of solid-phase H₂ differs strongly from model to model. Also, the results depend on the ratio of gas-phase atomic O and H arriving at the surface. Nevertheless, it is important for modelers to include all of the mechanisms so that water can be produced under diverse physical conditions.

As the dust temperature rises from 10 K, larger species than atoms begin to diffuse both on and inside the ice mantles. Most of these species are not reactive unless activated by the formation of radicals, which can occur via photodissociation or via energetic particle bombardment, such as cosmic rays. Association reactions of radicals can lead to complex organic species, as discussed by Garrod and Widicus Weaver in this issue (<http://dx.doi.org/10.1021/cr400147g>).

3.3.3. Water Ice Desorption. Thermal Sublimation. As the dust temperature rises from 10 K to about 30 K, sublimation of the more volatile molecules, such as CO, begins. Once the dust temperature rises above 100 K, water ice and complex organic species sublime on very short time scales under interstellar conditions,^{19,254} leading to high gas-phase abundances of water and organics. The binding energy E_D of water ice to be used in eq 16 is 5600 K for pure amorphous ice, with a slightly higher value of 5770 K found for crystalline ice.¹⁹ Above ~100 K, the desorption rate of interstellar ice is so rapid due to the exponential dependence that the half-life time of ice mantles (i.e., the time it takes for the surface population of H₂O molecules on an interstellar grain to decrease to half its initial value) becomes less a year (see Table 2 in Fraser et al.¹⁹). As a result, the gas-phase abundance of water can become temporarily as high as the original ice abundance, on the order of 10⁻⁴ with respect to H₂.

In realistic astronomical ice mixtures, the sublimation pattern can be rather complex, since a number of different effects can occur in which the combined ices do not have independent desorption rates,^{255,256} but since water is the principal ice ingredient, this does not affect the water chemistry. Note that the precise dust temperature at which rapid desorption sets in is density-dependent through the Clausius–Clapeyron relation and can be obtained by solving the desorption/accretion balance: at densities of 10¹³ cm⁻³ found in the inner regions of protoplanetary disks,¹²⁴ the sublimation temperature is increased to 160 K. Similarly, planetary surfaces such as those of the Jovian moons Europa and Ganymede in our own solar system are covered by water ice even though their temperatures are somewhat above 100 K.

Photodesorption. At dust temperatures below ~100 K, the best-studied mechanism that can get some small fraction of water ice returned to the gas phase is photodesorption. This process has been studied in detail in the laboratory^{240,257} and through classical molecular dynamics simulations.^{115,116,258–261} It starts with photodissociation of a water molecule in the ice after absorption of a UV photon, followed by a number of subsequent processes involving the dissociation fragments:



Since both fragments have excess energy and are able to move through the ice, there are a number of possible outcomes of the process (Figure 18):

- (1) H desorbs while OH stays trapped in the ice
- (2) OH desorbs while H stays trapped in the ice
- (3) H and OH both desorb
- (4) H and OH are both trapped in the ice
- (5) H and OH recombine to H₂O, which desorbs
- (6) H and OH recombine to H₂O, which stays trapped in the ice

The probabilities of each of these processes have been computed and depend strongly on the depth into the ice. Figure 19 summarizes the probabilities for the first six monolayers for

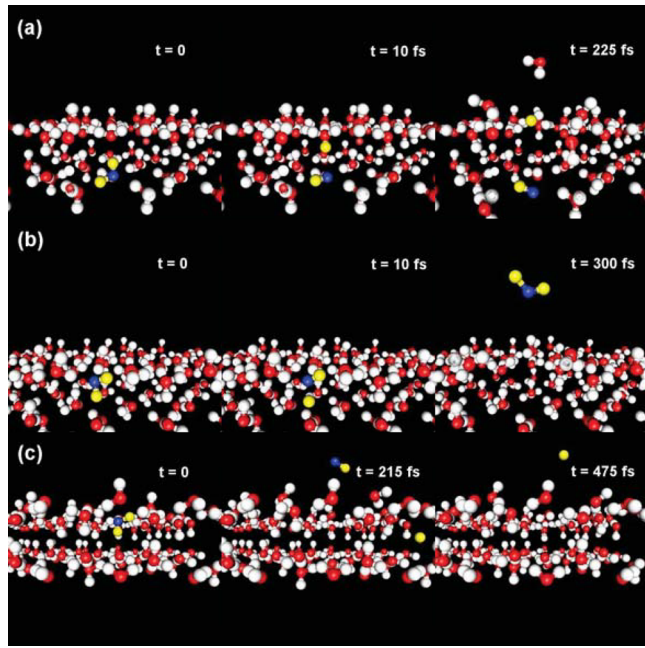


Figure 18. Snapshots of trajectories of mechanisms of H₂O photodesorption for a crystalline ice model. (a) One of the surrounding molecules desorbs (“kick-out” mechanism). (b) The photofragments H and OH recombine and desorb as H₂O. (c) The photofragments both desorb as separate species. The red and white atoms correspond to O and H atoms in the surrounding ice, and the blue and yellow atoms correspond to the O and H atoms of the photodissociated H₂O molecule. Reprinted with permission from ref 115. Copyright 2008 European Southern Observatory.

the case of a compact amorphous ice structure.¹¹⁵ Consistent with experiments, photodesorption of H, OH, and H₂O (outcomes 1, 2, 3, and 5) only occurs for the top few monolayers of the ice; the other outcomes (4 and 6) are part of the normal photodissociation processes that also take place deep inside the ice. The model finding that the OH desorption probability is larger than that of H₂O is consistent with experiments, although the theoretical OH/H₂O production ratio is somewhat higher than the experimental value²⁴⁰ of ~2. Interestingly, the probabilities for crystalline and compact amorphous water ice are found to be very similar.¹¹⁶ Also, variations with ice

temperature in the 10–100 K range are small: there is a ~30% increase for the OH and H₂O desorption probabilities when the ice temperature is increased from 10 up to 90 K.^{240,258,260}

In parallel with the six outcomes noted above, there is another mechanism operating in the top few layers initiated by the same UV photon: the energetic H atom can “kick out” a neighboring H₂O molecule before it desorbs, becomes trapped, or recombines (see Figure 18). Probabilities for this kick-out mechanism and all other mechanisms are summarized for water and its isotopologues in Arasa et al.^{258,259,261}

There are two important caveats in these simulations. First, they only consider excitation of H₂O ice into the first excited $\tilde{\text{A}}$ electronic state, but not into the higher $\tilde{\text{B}}$ or $\tilde{\text{C}}$ states. The probabilities for each of the outcomes may be different if a higher electronic state is excited, because the fragments will have more translational energy. Also, the higher OH internal rotation following the $\tilde{\text{B}}$ state dissociation (see section 3.1.3) may change the relative outcomes. Since the $\tilde{\text{A}}$ state is the dominating channel, the main conclusions are unlikely to change, however. Second, the molecular dynamics calculation only follows the processes on picosecond time scales. On the much longer time scales in the laboratory experiments and in space, slower diffusion processes may play a role. Wavelength-dependent water ice photodesorption experiments measuring both the OH and H₂O channels are warranted.

3.4. Solving the Kinetic Equations

The chemistry that occurs in astronomical sources is rarely defined by thermodynamics for a number of reasons. In low-temperature sources such as cold interstellar clouds, most reactions are exceedingly slow and do not occur significantly within the lifetimes of the sources. Those reactions that do occur efficiently must be barrierless and exothermic; typical destruction routes are not the reverse of formation routes, so even though a steady state can occur eventually, the situation never reaches true thermodynamic equilibrium, although astronomers often use the term inappropriately. Also, the UV radiation field is characterized by a much higher temperature than the kinetic temperature. It is thus necessary to solve the kinetics directly. The reactions that directly lead to the formation and destruction of water in various sources and varying conditions depicted in Figure 16 must therefore all be considered. A summary of important gas-phase reactions and their rate coefficients leading to water is given in

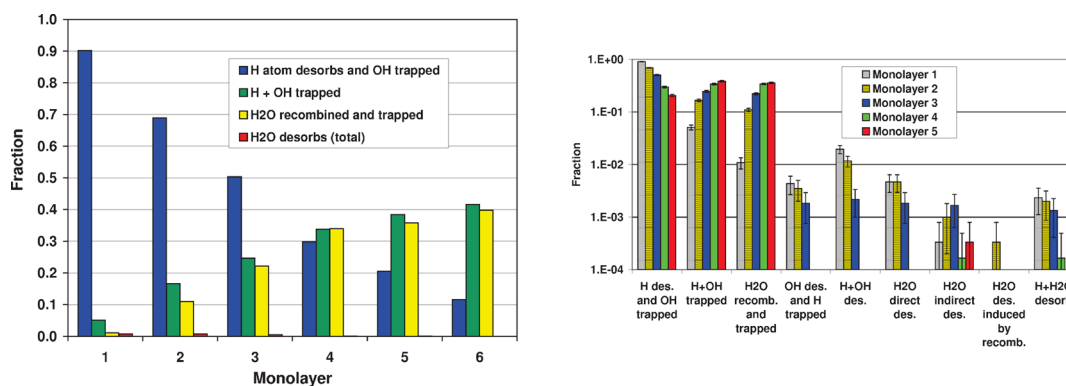


Figure 19. (Left) Fractions of the main outcomes after H₂O ice photodissociation for the top six monolayers of amorphous ice on a linear scale. These probabilities are calculated from all trajectories in classical molecular dynamics simulations, irrespective of excitation energy. Note that H₂O desorbs in only a very small fraction of the outcomes. Right: Fractions of the detailed outcomes after H₂O photodissociation for the top five monolayers of amorphous ice on a logarithmic scale. The error bars correspond to a 95% confidence interval. Reprinted with permission from ref 115. Copyright 2008 European Southern Observatory.

Table 1 of Hollenbach et al.²⁶² Networks of chemical reactions to be included in general models of interstellar chemistry can be found in assorted URLs such as the UDFA and KIDA sites www.udfa.net/ and kida.obs.u-bordeaux1.fr/model; these networks can contain up to 10 000 reactions involving 1000 species; many of the reactions included have not yet been studied in the laboratory under the relevant physical conditions. The KIDA database also contains codes for the solution of the chemistry via rate equations.

3.4.1. Rate Equations and Models. The standard approach to the determination of time-dependent atomic and molecular concentrations $n(AB)$ in a system of coupled chemical reactions is to use standard kinetic (rate) equations for each of the species in the system and to integrate them as a function of time subject to constraints such as the total gas density and temperature, the elemental abundances, and the initial abundances of each species. Rather than concentrations, the modelers usually report “abundances”, which are referenced to the density of molecular hydrogen [$x(AB) = n(AB)/n(H_2)$] or to total hydrogen nuclei $n_H = n(H) + 2n(H_2)$ [$x(AB) = n(AB)/n_H$]. Note the factor of at least 2 difference between these two definitions. In addition to chemical reactions, processes such as photodissociation and photoionization need to be included, as well as accretion and desorption processes for models that include grain chemistry.

In the simplest models, the density and temperature remain homogeneous and time-independent. These models are often labeled “pseudo-time-dependent” because only the chemistry changes with time, eventually reaching a steady state. If only the temperature is allowed to change with time and the density is constant and homogeneous, the term used to describe the situation is “0-D”, a terse term meaning that there is no dependence on spatial parameters. If the physical conditions change along one particular axis, the term used is “1-D”. This term is often used to describe diffuse and translucent clouds and more generally the photon-dominated regions (PDRs) in which a nearby star is the source of photons traveling into a nearby cloud.²⁶³ The photons cause both the physical diversity as well as the consequent chemical diversity along the axis. Static 2-D models in which the physical parameters remain constant with time also exist: examples include protoplanetary disks²⁶⁴ or protostellar envelopes in which an outflow cavity has been carved out.¹⁹⁷ The most complex physical models couple hydrodynamics (either semianalytic or numerical, in 1D, 2D, or 3D) with chemistry; these have been calculated primarily for low-mass star-forming regions representative of the origins of our solar system, in which material collapses inward to form a star surrounded by a protoplanetary disk.^{265–268}

Although most sources studied by astrochemists contain both a gas phase and a condensed phase consisting of small dust particles, some aspects of the chemistry can be handled by networks that are almost exclusively gas phase in nature, especially in low-density diffuse clouds. The one major exception is the formation of molecular hydrogen from two neutral H atoms, which can only occur efficiently in the interstellar medium on the surfaces of dust particles. In such a gas-phase model, the formation and destruction of gaseous water at low temperature (Figure 16) is incorporated through the differential rate equation

$$\begin{aligned} \frac{d[H_2O]}{dt}_{LT} &= k_{dr}[H_3O^+][e] - k_{im}[H_2O][I^+] \\ &\quad - k_{pd}[H_2O] \end{aligned} \quad (20)$$

where LT stands for low temperature and the brackets for concentration, with I = ion, and only the dominant reactions are

included. Formation occurs through a dissociative recombination reaction, which also forms the radical OH. Such reactions tend to become more rapid as the temperature is reduced; viz., $k_{dr} \propto T^{-0.5}$ (section 3.1). It is easily seen that this equation is coupled with differential equations for the abundances of other species, such as that for the protonated water ion, H_3O^+ , which itself is formed by the series of ion–neutral reactions depicted in Figure 16. Destruction of water occurs through a number of ion–neutral reactions involving positive ions I⁺ such as HCO^+ and H_3^+ ; photodissociation is also important under certain conditions.

For sources or portions of sources in which the temperature exceeds 200 K, neutral–neutral reactions can become dominant, even if they are endothermic or possess barriers. For water, in particular, eq 20 has to be supplemented (or replaced) by the formation reaction between OH and H₂ (reaction 13), which is exothermic but possesses an activation energy barrier:

$$\frac{d[H_2O]}{dt} = \frac{d[H_2O]}{dt}_{LT} + k_{OH-H_2}[OH][H_2] \quad (21)$$

The activation energy barrier is also counteracted by the high abundance of H₂, the concentration of which is 10⁴ times greater than that of the second most abundant molecule, CO. At high temperatures, the radical OH is itself formed mainly via the neutral–neutral reaction between O and H₂ (reaction 12), as depicted in Figure 16 and discussed above. Up-to-date general networks for the gas-phase chemistry including reactions and their rate coefficients as functions of temperature can be found in the above-mentioned KIDA and UDFA databases; the former contains a special high-temperature addendum²²³ for temperatures up to 800 K.

For gas-phase models, sensitivity analyses are available to determine the relative importance of reactions for specific species under given physical conditions and to determine the uncertainty of the calculated abundances based on the uncertainties, measured or estimated, of the rate coefficients in the reaction network utilized.²⁶⁹ For example, for the case of water vapor, the cumulative uncertainties in all gas-phase reactions leading to water result in a ±0.5 dex spread in water abundances for a dark cloud model.²⁷⁰ Such analyses provide useful information on the ongoing collaborations between modelers of interstellar sources and the laboratory and theoretical chemists who measure or calculate rate coefficients for use in the chemical simulations.

3.4.2. Gas–Grain Simulations and Surface Chemistry.

The solution of gas–grain chemical simulations of interstellar sources is most easily accomplished by using rate equations for both gas-phase and grain–surface reactions. In the rate equations, both accretion and desorption processes must be included. Using water as an example, a simplified version of the rate equation of water ice, denoted as s-H₂O, can be written as

$$\begin{aligned} \frac{d[s-H_2O]}{dt} &= K_{LH}[s-OH][s-H] + K_{LH}[s-OH][s-H_2] \\ &\quad + K_{acc}[H_2O] - K_{subl}[s-H_2O] \\ &\quad - K_{ntd}[s-H_2O] - K_{pd}[s-H_2O] \end{aligned} \quad (22)$$

where, as before, an upper case K is used for the rate coefficients on the grains to distinguish them from gas-phase rate coefficients, and no distinction is made between bulk and surface reactants. Although chemical destruction routes for other surface molecules exist, for water the dominant destruction is via nonthermal desorption (ntd) at low temperatures and sublimation (subl) at temperatures when they rise to near 100 K. Photodissociation (pd) in which the H and/or OH fragments

remain in the ice or photodesorb can also be important (see section 3.3.3).

3.4.3. More Advanced Approaches. In the previous sections, the rate equation method for surface/ice chemistry was discussed, with no distinction being made between the surface and the interior layers of the ice mantle, other than for the distinction between photodesorption and photodissociation. It is possible to use the rate equation approach and consider the surface and interior layers separately; while the simple approach is known as a two-phase approach (surface + interior and gas phase), the more complex method is known as a three-phase approach (surface, interior, gas phase). Although this approach has been tried since the initial work of Hasegawa and Herbst,²⁷¹ it does not solve all of the problems with the rate equation approach. One rather basic problem is that grains are small and the flux of accreting species is also small, except in the densest cores. The result is that on some of the smaller grains, with radii much less than the standardly used value of $0.1\text{ }\mu\text{m}$, the average abundance of reactive species such as H can be considerably less than 1 per grain. In such a situation, one must take account of both the discreteness of the rate problem and the fact that fluctuations are likely to be large. For example, consider the formation of molecular hydrogen under these circumstances. For the process to happen, there must be at least two hydrogen atoms on a given grain at the same time, clearly a fluctuation. To achieve these goals requires what is known as a “stochastic” approach, in which the laws of probability are utilized, although it is possible to mimic some of the stochastic effects with an empirical modification of the rate equations,²⁷² whether the calculation be a two-phase or three-phase one. This modification, known as the modified rate approach, has been improved by Garrod²⁷³ and shown to be a good substitute for more time-consuming stochastic methods over certain ranges of physical conditions.²⁷⁴

There are two principal stochastic approaches that can be applied to grain surface/ice chemistry: one is known as the master equation approach²⁷⁵ and the other is known as the Monte Carlo approach.^{8,188,276} In the former approach, the concentrations are replaced by probabilities. For example, if we consider a simple system in which only H atoms land on grains, one would formulate individual deterministic equations for the probabilities of 0 H atoms, 1 H atom, 2 H atoms, etc. on a grain; their solution would then give a time-dependent distribution of H atoms, which would allow one to determine both the average and the standard deviation. Unfortunately, if we expand the system from one surface reactant to many, we have to compute joint probabilities; e.g., the simultaneous probability of 1 H atom, 1 O atom, 10 CO molecules, etc. on an individual grain, resulting in very large numbers of equations to solve and necessitating some approximations. At present, the most popular approximation to the master equation method is known as the method of moments, and it has been applied successfully on a small number of attempts.²⁷⁷ It is used in a “hybrid” approach with rate equations depending upon whether the abundances of reactants are large or small. The strong point of a method based on the master equation is that the differential equations can be solved simultaneously using one integrator with the rate equations used for the gas-phase chemistry.

The Monte Carlo approach is based on the choice of random numbers to mimic the stochastic chemistry. In a given time period, one compares the rates of various processes, e.g., chemical reactions on the surface, accretion, and desorption, and links them to proportional ranges of random numbers in the range 0–1. Thus, if there are two processes to consider and one is

twice as fast as the other, the faster one could be assigned random numbers from 0 to 0.6666 and the slower from this number to unity. So, after many time periods of calling random numbers, the comparison in rate between the two processes should indeed be two. The rates of the processes are still determined using rate coefficients and concentrations of species. One strong point of the Monte Carlo approach is that it can be used in both a macroscopic and microscopic sense, and anything in between. In the macroscopic sense, the only interest is in the number of atoms or molecules of a given species on a grain and not where they are located. In a fully microscopic Monte Carlo treatment, on the other hand, the interest is in exactly where on each monolayer individual species are located as well as pores in the ices.

The details of the microscopic approach used for surface/ice chemistry, known as the continuous time random walk (CTRW) approach,¹⁸⁸ are discussed in the review by Chang et al., so they will not be repeated here in detail. The basic idea is to consider a grain as a square lattice of binding sites with periodic boundary conditions. One can start with either a “flat” surface of silicates or amorphous carbon, in which all binding sites are the same, or with a “rough” surface in which there are irregularities among binding sites. As accretion, chemistry, and desorption occur, monolayers of ices are built up and the details of the ice on a specific grain emerge. Figure 20 shows the formation of water ice

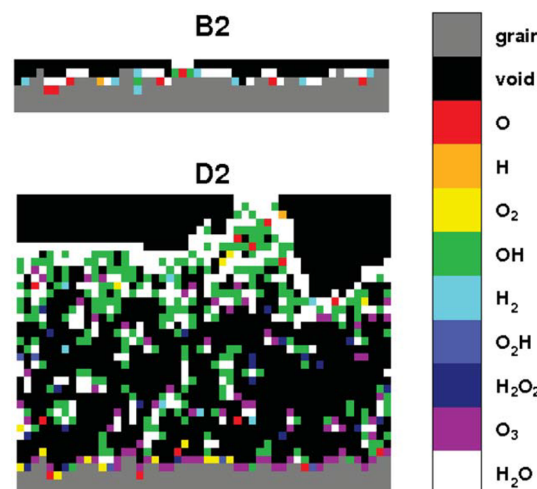


Figure 20. Vertical cross section of the production of water ice after 3×10^5 yr in a translucent interstellar cloud from different mechanisms shown in Figure 16. The CTRW Monte Carlo results are taken from the B2 and D2 models of Cuppen and Herbst²⁵² with $n_{\text{H}} = 250\text{ cm}^{-3}$, $T_{\text{d}} = 16\text{ K}$, and $A_V = 1\text{ mag}$ and $n_{\text{H}} = 10^3\text{ cm}^{-3}$, $T_{\text{d}} = 14\text{ K}$, and $A_V = 3\text{ mag}$, respectively. Water molecules are shown in white, OH radicals in green, H_2O_2 in blue, H_2 in light blue, O_2 in yellow, O_3 in purple, and pores in black. The topmost layers of the actual grain are seen to be rough. Reprinted with permission from ref 252. Copyright American Astronomical Society.

and other molecules such as OH from H , H_2 , O , O_2 , and O_3 for an individual grain in a diffuse (top) and translucent (bottom) interstellar cloud, with the latter having a visual extinction of $A_V = 3\text{ mag}$ and a total hydrogen density of 10^3 cm^{-3} . The gas phase consists of atomic hydrogen and oxygen and is unchanged as the grains evolve for 3×10^5 yr. No gas-phase chemistry is included. In the diffuse cloud model, virtually no water ice is formed because of rapid photodissociation and photodesorption of all the reactants. In the translucent cloud model, water is formed on

the surface, but there is a still a significant residual amount of OH in the lower monolayers where H cannot penetrate to react with OH. These models have a significant amount of empty space in the ice, but the model porosity depends sensitively on the initial roughness of the surface and associated diffusion rates, as well as the deposition rate, and may be overestimated in these models.

The basic difficulty with the microscopic treatment is that it takes a large amount of computer time, even without coupling to the gas-phase chemistry, and the weakness of the Monte Carlo method as a whole is that it cannot easily be coupled with normal rate equations for the gas-phase chemistry. Rather the gas-phase chemistry must be treated by a macroscopic Monte Carlo method whatever type of Monte Carlo approach is used for the surface/ice chemistry. The result is that only a few stochastic calculations with the microscopic Monte Carlo approach have been attempted, and these are mainly simulations of ice buildup without gas-phase chemistry, or simulations with gas-phase chemistry and only a small number of surface reactions. Figure 21

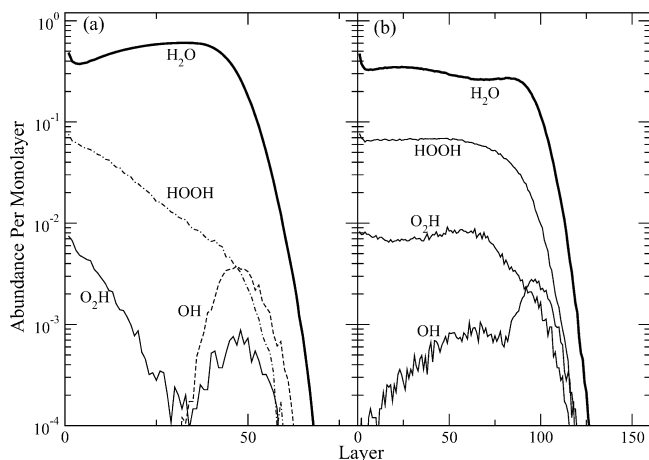


Figure 21. The fraction of each monolayer occupied by assorted molecules including water using gas (macroscopic Monte Carlo)–grain (microscopic Monte Carlo) models for 10 K cold dense interstellar clouds. The layers increase from the innermost layer 0 to the outermost layer. The gas temperature is taken to be the same as the dust temperature. Model a (left) has $n_{\text{H}} = 2 \times 10^4 \text{ cm}^{-3}$, and model b (right) has $n_{\text{H}} = 10^5 \text{ cm}^{-3}$. Adapted with permission from ref 278. Copyright American Astronomical Society.

shows model molecular abundances²⁷⁸ as a function of monolayer for cold grains in dense clouds at 10 K. Unlike the translucent case, the water is formed mainly in the inner rather than outer monolayer. It is still not yet possible to compare the rate equation approach with Monte Carlo stochastic ones, although Chang et al. are working on an approximation that should make large gas-grain simulations with many surface reactions possible with the microscopic–macroscopic Monte Carlo approach. In addition, a method developed by Vasyunin and Herbst,²⁷⁹ in which there is somewhat less information about the positions of species within individual monolayers, is now in the public domain.

A number of papers have shown that gas–grain chemical simulations with macroscopic stochastic approaches to the surface chemistry can differ significantly from those using rate equations under specific physical conditions and times. Detailed examples are shown by Garrod et al.,²⁷⁴ where, for example, under some conditions and times, the CO gas-phase and ice-phase abundances calculated by rate equations can differ by more

than 1 order of magnitude from a stochastic approach. CO is one of the worst cases, however, and discrepancies are much smaller when the rate equation approach is modified according to the prescription of Garrod.²⁷³ For the case of H_2O , agreement is generally within 10% for the two approaches. One major advantage of the stochastic approaches is that they are correct physically and should give the correct answer, if the chemical and physical processes are correctly treated, whereas there is no security in using the rate equation method, whether it be done in a two-phase or a three-phase calculation. Moreover, microscopic stochastic approaches can take into account grains with roughness on the surface, which are far more likely to occur in space than flat grains. The bulk of the models described in section 4 have been carried out with the two-phase rate equation method, however, with at most a partial modification.

4. COMPARISON WITH OBSERVATIONS

In section 3, three different routes to water in space have been described in detail and important individual molecular processes leading to the formation and destruction of water have been identified, both in the gas phase and in the solid phase, as well as at the gas–solid interface. In this section, we summarize the observations of water in different astrophysical sources and explore to what extent the observed abundances of water are consistent with the chemistry described in section 3. The discussion is ordered by the different types of chemistry that dominate the formation and destruction of water in a particular set of sources, rather than by type of astronomical source. Thus, some types of sources can appear more than once in the examples. A review of water from the astronomical perspective as it cycles from cold clouds to disks and planets is given by van Dishoeck et al.²⁸⁰

As a general comment, it should be recalled that astronomers only observe column densities N in cm^{-2} integrated along the line of sight L in cm rather than local concentrations n in cm^{-3} , which are usually obtained from models. As noted in section 1.4, astronomers often adopt the visual extinction A_V as a measure of the depth into a cloud, using the empirical relation $N_{\text{H}} = (1.8 \times 10^{21})A_V \text{ cm}^{-2}$. For dense clouds shielded from radiation, there is little variation with depth into a cloud, and the fractional abundances are usually taken to be the same as the column density ratios, i.e., $n(\text{X})/n(\text{H}_2) = N(\text{X})/N(\text{H}_2)$. For low- and high-density PDRs, proper comparison requires the calculation of column densities integrated through the model cloud. Unless stated otherwise, fractional abundances are quoted relative to H_2 , and are simply called “abundances”. To convert to abundances with respect to total hydrogen nuclei, $n_{\text{H}} = n(\text{H}) + 2n(\text{H}_2)$, the abundances need to be divided by a factor of 2 (assuming the atomic hydrogen fraction to be negligible).

In many cases, the accuracy in observed abundances is limited to a factor of a few, primarily by uncertainties in the *denominator*, i.e., the H_2 column. Because H_2 can generally not be observed directly, indirect tracers have to be used. Many different methods exist, ranging from the use of simple molecules like CH in diffuse clouds to measurements of CO and its isotopologues in dense clouds. For dense star-forming regions where freeze-out plays a role, dust continuum observations often provide a more reliable tracer, although this assumes a gas/dust mass ratio of typically 100. Agreement between models and observations is usually considered to be good if they are within 1 order of magnitude in observed columns. Some of the chemistry tests described below are at the factor of 2–3 level, which is considered excellent agreement. Measured abundance ratios of species, e.g., $\text{H}_2\text{O}/$

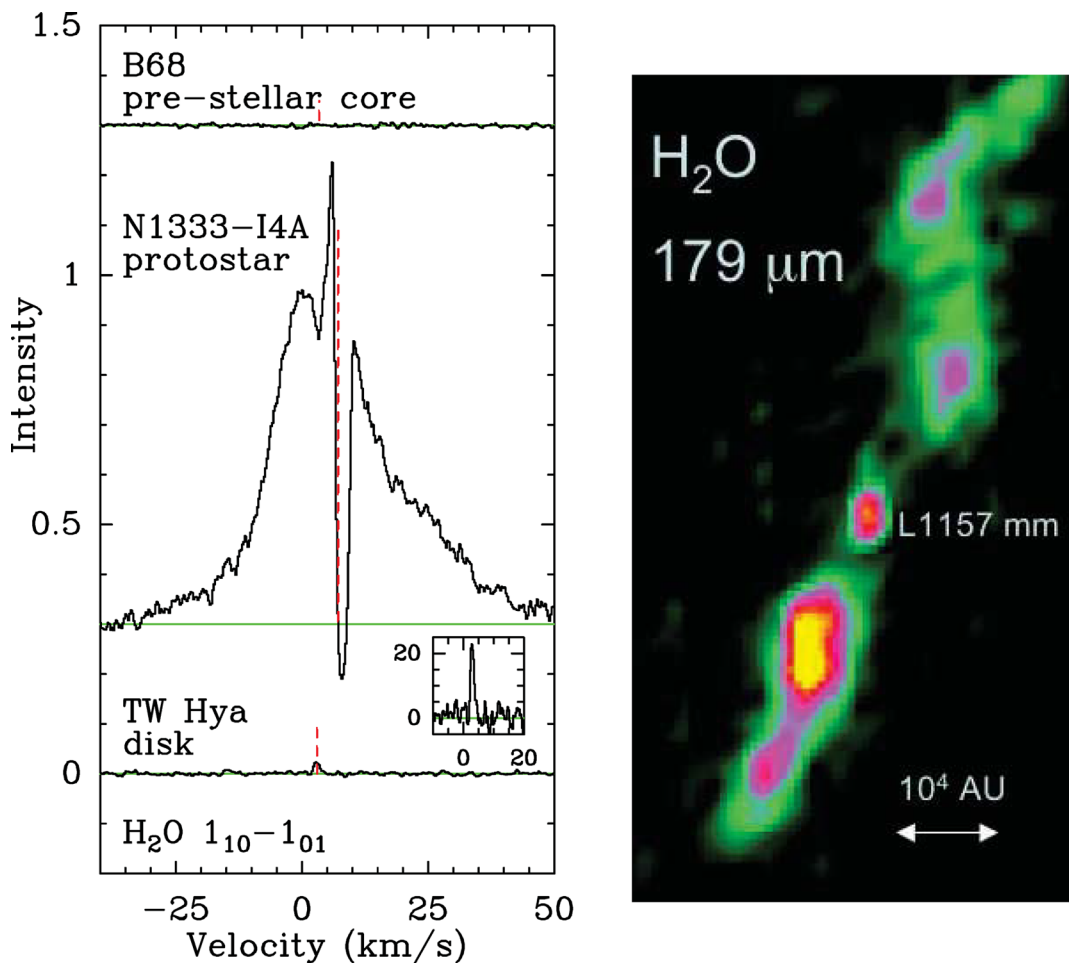


Figure 22. (Left) Herschel-HIFI spectra of the ortho-H₂O 1₁₀–1₀₁ 557 GHz line across the different evolutionary stages of a low-mass protostar. From top to bottom: the prestellar core B68,²⁸³ the low-mass protostar NGC 1333 IRAS4A, and the protoplanetary disk TW Hya.²⁸⁴ Note that only the protostellar stage shows strong and broad water lines, coupled with narrow absorption lines. The intensity is in units of K, whereas the insert for TW Hya is in units of millikelvin. Adapted with permission from ref 281. Copyright 2012 Wiley. (Right) Herschel-PACS image of the H₂O 2₁₂–1₀₁ line at 179 μm toward the L 1157 protostar.²⁸² Water emission is strong toward the protostar itself and also in “hot spots” along the outflow. Adapted with permission from ref 40 (Copyright 2011 The University of Chicago Press.) and from ref 282 (Copyright 2010 European Southern Observatory.).

OH, are often more accurate than absolute abundances, H₂O/H₂.

Figure 22 (left) shows Herschel-HIFI spectra of H₂O of astronomical sources at different stages of evolution,²⁸¹ whereas Figure 22 (right) shows a PACS image of water in the protostellar phase.²⁸² The strength of the lines is related to the abundance of water, whereas the line profiles provide information on the kinematics of the gas containing water. Clearly, water emission is weak in some sources and strong in others. The water line profiles are complex with a mixture of narrow lines originating in cold quiescent gas and very broad and strong lines due to fast outflow gas. These observational characteristics point to different types of chemistry at work in different regions.

4.1. Testing Ion–Molecular Chemistry

Diffuse and translucent molecular clouds present a valuable laboratory for testing the gas-phase chemical models described in section 3.1 above. Such clouds may be observed in absorption toward background sources of continuum radiation, providing robust estimates of the molecular column densities. Because the Milky Way galaxy is rotating differentially, with an angular velocity that decreases with distance from the galactic center, multiple diffuse clouds along the sight-line to a given continuum

source may be distinguished by their Doppler shifts. Thanks to the relatively low densities within such clouds (Table 2) and the weakness of the submillimeter radiation to which they are typically exposed, most molecules are in the ground rotational state; in this regime, the inferred column densities are very insensitive to the assumed physical conditions. The main uncertainty in the abundances therefore comes from the determination of N(H₂). In these clouds, the CH and HF molecules are often used as surrogates,^{285,286} although these two tracers do not always agree. The N(HF)/N(H₂) conversion has recently been calibrated directly using near-infrared observations of both species.²⁸⁷

4.1.1. Water Abundances in Diffuse and Translucent Clouds. While ultraviolet searches for water vapor in translucent molecular clouds have not been successful³⁶ (see section 2.3 above), submillimeter absorption line observations of water have proven to be a powerful tool for the study of interstellar water vapor. Detections of foreground absorption by water along the sight-lines to several bright continuum sources were obtained by ISO, which was capable of detecting the 179 μm 2₁₂–1₀₁ transition of ortho-water,²⁸⁸ and by SWAS and Odin, which targeted the fundamental 1₁₀–1₀₁ transition of ortho-water near 557 GHz (Table 1).

Much more sensitive observations performed with Herschel have greatly expanded the number of sight-lines along which water absorption has been detected and have permitted observations of the $1_{11}-0_{00}$ transition of para-water, near 1113 GHz, along with the 557 GHz ortho-water transition.²⁸⁵ These observations have shown that the water abundance is remarkably constant²⁸⁹ within the diffuse interstellar medium, with the exception of the galactic center region, which appears to contain diffuse clouds with significantly higher water abundances by a factor of 3 than those found elsewhere in the galaxy.^{286,290} The typical water abundance relative to H nuclei is $\sim(0.5-1.5) \times 10^{-8}$, with no apparent trend with H₂ column density over the range $(3-30) \times 10^{20} \text{ cm}^{-2}$ or with galactocentric distance over the range 5.5–8 kpc. These values are broadly consistent within a few factors with model predictions for diffuse clouds,²⁶² providing support for the ion–molecule production route discussed in section 3 above. Figure 23 shows the abundances of water molecules predicted by Hollenbach et al.,²⁶² as a function of depth into a molecular cloud.

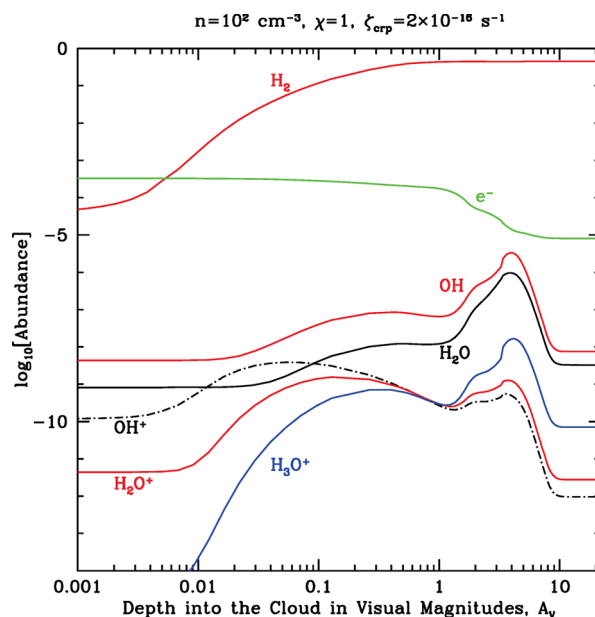


Figure 23. Predicted abundances (relative to H nuclei) as a function of depth into a molecular cloud measured by the visual extinction (see section 1.4). The assumed cloud density $n_{\text{H}} = 100 \text{ cm}^{-3}$, the incident UV radiation field is equal to the average galactic value ($\chi = 1$), and the cosmic-ray ionization rate $\zeta_{\text{H}} = 2 \times 10^{-16} \text{ s}^{-1}$. Reprinted with permission from ref 262. Copyright 2012 American Astronomical Society.

Absorption lines of H₂O and H₂¹⁸O have also been seen with Herschel-PACS toward the far-infrared continuum emission in external galaxies.^{291,292} Part of this absorption has been inferred to arise in a low-density extended component with water abundances of a few $\times 10^{-8}$, similar to those found in galactic diffuse and translucent clouds. Thus, ion–molecule chemistry appears to be widespread throughout galaxies.

4.1.2. Related Species in Diffuse and Translucent Clouds. In addition to water itself, Herschel-HIFI observations have allowed the intermediaries OH⁺ and H₂O⁺ to be measured along the same diffuse cloud sight-lines.^{195,293} OH⁺ was first detected from the ground using the submillimeter APEX telescope.²⁰⁰ Once again, the observed abundances are found to be in good agreement with the predictions of ion–neutral chemistry, for reasonable estimates of the cosmic-ray ionization

rate.¹⁸³ Because the OH⁺ and H₂O⁺ abundances peak closer to the cloud surface than do OH and H₂O (Figure 23), they can be detected in clouds with a small molecular fraction.¹⁹⁵ By contrast, the lowest frequency transition (at 2.5 THz) of the neutral OH radical in its ground state lies outside the frequency range covered by the HIFI instrument. It can, however, be observed at high spectral resolution using the GREAT instrument on the NASA/DLR airborne observatory SOFIA. Recent absorption line observations of this transition have provided robust estimates of the H₂O/OH ratio in diffuse clouds along the sight-line to three bright continuum sources;²⁹⁴ observed values in the range 0.3–1 are in good agreement with model predictions (Figure 23). Similar H₂O/OH ratios are found in diffuse extended regions of galaxies.²⁹¹ Previous observations of OH at UV wavelengths in a different set of diffuse clouds toward bright stars^{295–297} have also been reproduced well with the basic ion–molecule network within a factor of 2.¹⁹¹

OH⁺, H₂O⁺, and H₃O⁺ absorption has been detected as well in some external galaxies, even from energy levels up to ~ 200 K using Herschel-PACS.²⁹⁸ The abundance ratios are consistent with the ion–molecule chemistry in relatively low density gas with a high atomic fraction, starting with H⁺ and followed by charge transfer to O⁺ (eq 8). The inferred cosmic-ray ionization rate $\zeta_{\text{H}} > 10^{-13} \text{ s}^{-1}$ for clouds in these galaxies is at least 2 orders of magnitude higher than those found in galactic sources, however.

4.1.3. Dense PDRs. Dense molecular clouds close to bright O or B stars are exposed to much more intense UV radiation than diffuse and translucent clouds, typically by a factor of 10⁴. An illustrative example is provided by the Orion Bar PDR. The Herschel-SPIRE spectrum of this source²⁹⁹ reveals strong CO lines, but only weak low-J H₂O lines, implying a water abundance $\leq 5 \times 10^{-7}$. In contrast, a number of OH lines are readily detected with Herschel-PACS³⁰⁰ indicating a high OH/H₂O column density ratio > 1 . These findings are consistent with dense PDR models,³⁰¹ where rapid photodissociation due to the intense UV radiation limits the buildup of water. The strong OH emission most likely originates in the warm (~ 200 K) H/H₂ transition layer, where vibrationally excited H₂ is produced, which can react with atomic O without barrier to form OH (see eq 12 and associated discussion). The only other dense PDR for which water data have been published is the Monoceros R2 region.³⁰² The inferred water abundance in the quiescent part of the cloud is again low, about 10⁻⁸.

In summary, observations of water and related species in diffuse and translucent clouds as well as dense PDRs confirm the basic ion neutral chemistry outlined in section 3.1, within the factor of a few uncertainty in both observations and models. The fact that all the intermediate ions in the network leading to water have now been observed, both within our own Milky Way and in external galaxies, leaves little doubt about the main processes at work. Since the principal reactions are well-determined, observations of these species can now be used as diagnostics of astrophysical parameters, such as the cosmic-ray ionization rate, UV radiation field and density.

4.2. Testing Solid-State Chemistry: Ice Formation and Photodesorption

4.2.1. Cold Clouds: Ice Observations. The most direct evidence for solid-state formation of interstellar water comes from the detection of the 3 μm O–H stretching vibration band of water ice toward numerous infrared sources.^{99,303} In many cases, the 6 μm bending and 11 μm librational modes have also been

observed (see Figure 12). The observations²¹ show that water ice formation starts at a threshold extinction of $A_V \approx 5$ mag in clouds that have densities of at least 1000 cm^{-3} . Cuppen and Herbst²⁵² have simulated the formation of water ice at the microscopic level, layer by layer, for clouds with densities ranging from 10^2 to $5 \times 10^4 \text{ cm}^{-3}$ and extinctions up to 10 mag (Figure 20). Critical parameters in the models are the binding energies and diffusion barriers, as discussed in section 3.3. Only the higher extinction models start to approach the observed columns of water ice because of rapid photodissociation and photodesorption of grain-surface species. The lifetime of the cloud is also an important parameter:³⁰⁴ densities need to be larger than $\sim 10^4 \text{ cm}^{-3}$ in order for the time scale for an O atom or molecule other than H₂ to collide with a grain and stick on it to become shorter than the age of the cloud, the latter being at least a few $\times 10^5$ yr.

In dense clouds, the bulk of the water is in the form of ice,^{88,98,102,303,305,306} at levels of H₂O ice/H₂ $\approx 10^{-4}$. Such high ice abundances are too large to result from freeze-out of gas-phase water produced by ion–molecule reactions,³⁰⁷ so grain surface reactions must surely happen. The overall abundance of elemental oxygen with respect to hydrogen nuclei in the solar neighborhood³⁰⁸ is estimated to be 5.75×10^{-4} , of which 16–24% is locked up in refractory silicate material in diffuse clouds.³⁰⁹ If this silicate fraction stays the same in dense clouds, and if the amount of oxygen locked up in CO gas and ice ($\sim 1.4 \times 10^{-4}$) is subtracted, the maximum abundance of water ice in dense clouds would be $(2.4\text{--}2.9) \times 10^{-4}$ with respect to hydrogen nuclei or $(5\text{--}6) \times 10^{-4}$ with respect to H₂. Thus, the observed ice abundances in dense clouds of $\sim 10^{-4}$ indicate that water ice contains a significant fraction of the available oxygen, but not all of it.³¹⁰ It is still unclear whether all oxygen is fully accounted for and, if not, in which form the missing oxygen is.³⁰⁹

4.2.2. Cold Pre- and Protostellar Cores: Gas-Phase Water. Another strong but more indirect argument in favor of ice chemistry comes from the weak gas-phase H₂O lines and lack of O₂ lines observed by SWAS and Odin in cold molecular clouds. Most likely, atomic O is converted rapidly on the grains into water ice, only a small fraction of which is subsequently desorbed back into the gas by nonthermal processes.^{9,311,312} A generic set of models for this situation has been developed by Hollenbach et al.,⁹ which is illustrated in Figure 24. Because H₂O and O₂ are only abundant at intermediate depth, their integrated column densities over depth reach a maximum value that is much lower than if freeze-out were not taking place.

The most recent, quantitative test of this basic gas–grain chemistry comes from the first detection of extremely weak water vapor emission and absorption in the centrally concentrated prestellar core L1544, a cloud which is likely on the verge of collapse to form a new star.³¹³ The Herschel-HIFI line profile of the H₂O 1₀₀–1₀₁ 557 GHz transition toward L1544 is presented in Figure 25 (left) and shows both emission and absorption. This so-called “inverse P-Cygni profile” is indicative of inward motions in the core: the infalling red-shifted gas on the near-side of the core is partly absorbed against line and continuum emission produced deeper in the cloud, whereas the blue-shifted emission from the backside of the cloud can proceed unhindered to the observer.³¹⁴ Because the different parts of the line profile probe different parts of the core, this can be used to reconstruct the water vapor abundance as a function of position throughout the entire core. Specifically, the detection of an emission feature signals the presence of water vapor in the densest central part of the core, whereas the absorption profile is sensitive to the water abundance in the outer part of the core.

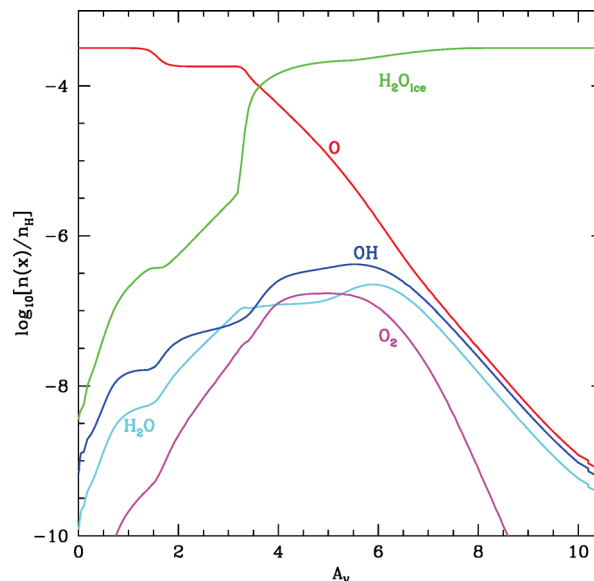


Figure 24. Oxygen chemistry for a standard steady-state cloud exposed to ultraviolet radiation including freeze-out, grain surface reactions, sublimation, photodesorption, and cosmic-ray desorption. Model abundances with respect to total hydrogen are shown as a function of visual extinction from the cloud surface, A_V . The density is $n_H = 10^4 \text{ cm}^{-3}$ and the cloud is illuminated by 100 times the average interstellar radiation field. Reprinted with permission from ref 9. Copyright 2009 American Astronomical Society.

Figure 25 (right) shows the best fitting water vapor abundance for L1544, using a temperature and density structure that has been determined independently from other data.³¹³ The main features of this figure are well described by a highly simplified water chemistry that contains just the freeze-out of gas-phase O and H₂O on the grains, the immediate formation of water ice from adsorbed s-O, the photodesorption of s-H₂O ice by the ambient and cosmic-ray-induced UV radiation fields back into the gas phase, and the photodissociation of gaseous H₂O. The critical parameters are the strength of the cosmic-ray-induced field combined with the photodesorption yield. Indeed, the presence of the blue-shifted emission requires efficient cosmic-ray-induced photodesorption of water ice in the center of the core, which was neglected in the models⁹ presented in Figure 24. Closer to the edge, at $A_V < 5$ mag, the interstellar radiation field takes over as the main photodesorption mechanism, and the gas-phase water abundance reaches its maximum of $\sim 10^{-7}$. At the very edge of the cloud, $A_V < 2$ mag, water gas is photodissociated and its abundance drops. Thus, water gas has a ringlike abundance structure, with its peak at intermediate depth into a core and decreasing abundances toward the edge and the center of the core that are measurable in the absorption and emission features.

The same simple water chemistry has also been found to reproduce well the water line profiles observed toward low-mass protostars, which show similar absorption and emission features after the outflow contributions have been removed.^{69,315,316} A prominent example is the NGC 1333 IRAS4A protostar, for which the observed HIFI spectrum is presented in Figure 22 and the best fitting model in Figure 26. The main difference with prestellar cores as shown in Figure 25 is that the dust temperature now increases rather than decreases from the edge of the core inward. The two cold core studies differ slightly in the best fitting parameters: the protostar study³¹⁶ finds that the standard CR-

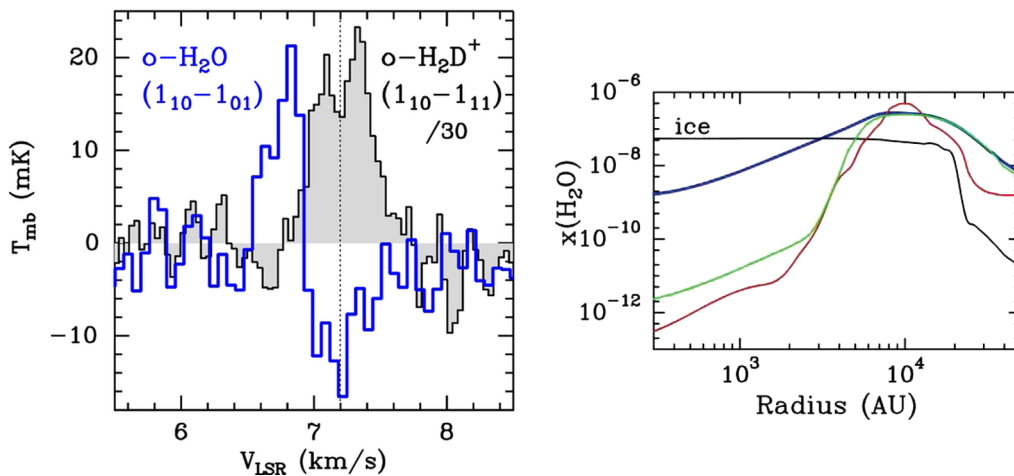
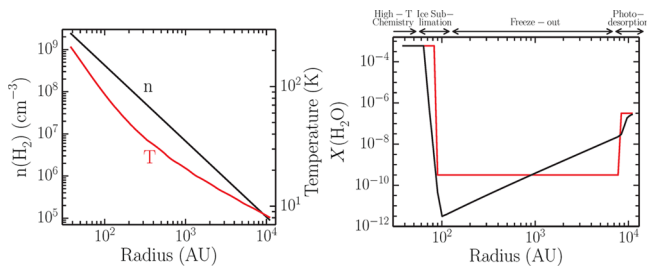


Figure 25. (Left) HIFI spectrum of ortho- H_2O $1_{10}-1_{01}$ at 557 GHz tracing the dense cold gas toward the prestellar core L1544 compared with ortho- H_2D^+ (intensity divided by 30). The water line shows emission only at blue-shifted velocities coming from the densest gas at the backside of the core, whereas water on the near-side of the core absorbs the far-infrared dust continuum emission produced by the core central regions. (Right) Best-fitting water vapor abundance profile through the core indicated in blue, obtained using a simplified water chemistry with cosmic-ray-induced photodesorption of water ice included. The red and green lines indicate the results of a full gas-grain and simplified water chemistry model, respectively, without cosmic-ray-induced photodesorption. The water ice abundance (black line) has been divided by a factor of 10^4 for clarity of presentation. Reprinted with permission from ref 313. Copyright 2012 American Astronomical Society.



UV flux of 10^4 photons $\text{cm}^{-2} \text{s}^{-1}$ combined with the measured photodesorption yield of 10^{-3} per incident photon²⁴⁰ fits the data well for several low-mass protostars, whereas the prestellar core study³¹³ uses the order of magnitude higher CR-UV flux adopted in earlier models.⁹ Also, the ortho/para ratio of H_2 used for the collisional excitation of H_2O plays a role.³¹³

Both studies, as well as Coutens et al.⁶⁹ agree on the need for a cloud layer in which water ice is photodesorbed by external UV radiation in order to obtain deep enough absorptions (Figure 26, adapted from ref 316). The discussion centers on whether this is simply the photodesorption layer at the illuminated edge around $A_V = 2$ mag of the envelope³¹⁶ or whether it is a separate cloud.⁶⁹ More generally, the step-function abundance structure used traditionally in the analysis of observations is now being replaced

by a more gradual power-law decrease of the abundance inward (Figure 26) until the ice sublimation radius is reached.³¹⁶

4.2.3. Outer Protoplanetary Disks. Protoplanetary disks around young stars, representing a later stage in the star formation cycle (Figure 1), provide another environment to test the water ice chemistry. Hogerheijde et al.²⁸⁴ detected the ground-state ortho- and para-water lines toward the young star TW Hya with Herschel-HIFI (Figure 22 and section 4.6). Disks have typical sizes of 200 AU diameter and are therefore small on the sky, on the order of 1" in the nearest star-forming regions. Thus, the signals from disks are strongly diluted in the large Herschel beam. Moreover, disks have typical masses of only $0.01 M_\odot$, a factor of 100 less than their parent clouds. Therefore, the signals of water from disks are expected to be very weak, requiring long integration times of >10 h to detect them. The TW Hya disk has a favorable near face-on geometry and is the closest known source of its kind, facilitating the detection of the water emission lines. Deep searches for water also exist for the outer portions of other disks, showing a common pattern of very weak or no emission.

The chemical structure of water in disks obtained from models^{317,318} is illustrated in Figure 27 and follows the typical

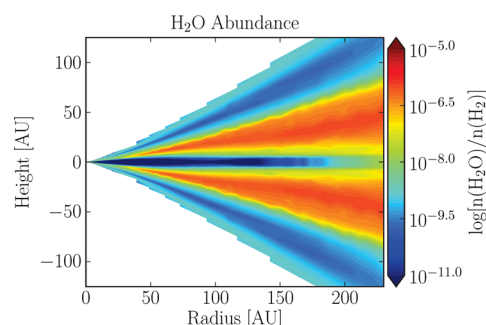


Figure 27. Abundance of water vapor relative to total hydrogen in the outer disk as a function of both radial distance and vertical height. Adapted with permission from ref 317. Copyright 2010 European Southern Observatory.

layered “sandwich” structure²⁶⁴ also found for other molecules. This structure is similar to that in Figures 24–26, but now in the vertical direction. The upper layers of the disk contain very little water due to rapid photodissociation by the stellar and interstellar UV radiation. In the cold midplane, where densities reach values of $>10^{10} \text{ cm}^{-3}$, virtually all molecules are frozen out. The bulk of the emission comes from the intermediate layers of the disk where UV radiation can still penetrate to photodesorb the icy grains, yet photodissociation is not too rapid.³¹⁹ Because of the large range of temperatures and densities contained in the beam, the test of the water chemistry is not as detailed as for the prestellar cores and protostellar envelopes discussed above, but the observations are broadly consistent with the models described here.

4.2.4. Related Ice Species. The above observational studies do not distinguish between the three different channels postulated by Tielens and Hagen⁸ to form water ice and confirmed and extended by the laboratory studies presented in section 3.3 (Figure 17). If the solid O and O₂ pathways are indeed equally important in dense cores, as suggested by models,^{243,277} then the intermediate products HO₂ and H₂O₂ should also be present in the gas at low levels assuming they have similar photodesorption yields as water ice. Indeed, a major confirmation of the ice chemistry comes from the recent detections of hydrogen peroxide, H₂O₂, and the hydroperoxyl radical, HO₂, toward ρ OphA.^{320,321}

In summary, both the original ice detections as well as more recent Herschel-HIFI and other studies validate the solid-state ice chemistry described in section 3.3 at a quantitative level to better than an order of magnitude. The detection of HO₂ and H₂O₂ demonstrates that gas–grain chemistry now has predictive power for other molecules. The era in which grain–surface chemistry could be considered “the last refuge of a scoundrel”³²² is definitely over.

4.3. Testing Gas–Grain Chemistry: Water Ice Sublimation

4.3.1. Warm Protostellar Envelopes and Hot Cores.

Close to a protostar, the dust temperature exceeds 100 K, at which point the sublimation of water ice becomes very fast under interstellar conditions and the dust grains lose their icy mantles on time scales short compared with the lifetimes of the sources (see section 3.3). These regions of warm, dense gas are known as “hot cores” (Figure 5 and 26), after the prototype in the Orion molecular cloud. They often have large abundances of complex organic molecules that are formed on the icy surface, trapped in the water ice, and released together with the water ice when the grains are heated. Thus, the water abundance in these hot cores is expected to be equal to the original ice abundance,⁹⁹ which is on the order of 10^{-4} within a factor of 2. This high water abundance will be maintained in the gas if the water vapor destruction is slow compared with the lifetime of the source or as long as there is continuous replenishment, e.g., by a moving ice sublimation front.

Tests of this simple prediction are possible for high-mass protostars. In particular, the ISO-SWS instrument was able to observe both the water ice (through the 3 and 6 μm ice features) and gas (through the 6 μm vibration–rotation band, Figure 10) in absorption along the line of sight toward several high-mass protostars in a single spectrum, thereby allowing an accurate determination of their relative column densities. A clear increase in the gas/ice ratio with increasing (source-averaged) dust temperature has been found, reaching values greater than unity.^{326–328} Boonman et al.³¹⁰ coupled a simple gas-phase and

ice chemistry with the physical structure of these sources to model both the ISO-SWS and -LWS and SWAS lines from 3 to 540 μm . A clear conclusion from this work is that scenarios without ice sublimation do not have large enough columns of warm (>100 K) water to reproduce the ISO-SWS spectra.

The wealth of Herschel-HIFI lines of H₂O, H₂¹⁸O, and H₂¹⁷O toward high-mass protostars (Figure 28) can be used to

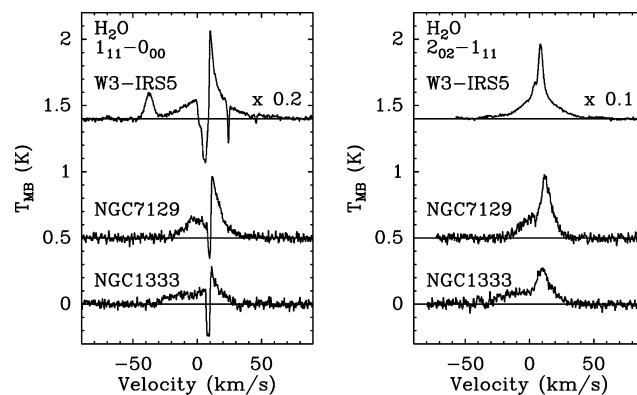


Figure 28. Herschel-HIFI spectra of the para-H₂O 1₁₁–0₀₀ 1113 GHz (left) and 2₀₂–1₁₁ 988 GHz (right) lines from low to high mass protostars. From top to bottom: the high-mass protostar W3 IRS5 ($L = 1.5 \times 10^5 L_\odot$, $d = 2.0 \text{ kpc}$),³²³ the intermediate-mass protostar NGC 7129 FIRS2 (430 L_\odot , 1260 pc),³²⁵ and the low-mass protostar NGC 1333 IRAS2A (20 L_\odot , 235 pc).³¹⁷ Note the complexity of the line profiles and the similarities from low to high mass. All spectra have been shifted to a central velocity of 0 km s⁻¹. The red-shifted absorption features seen in the 1₁₁–0₀₀ spectrum toward W3 IRS5 are due to water in foreground diffuse clouds, whereas the small emission line on the blue side can be ascribed to the SO₂ 13_{9,5}–12_{8,4} transition. Reprinted with permission from ref 40. Copyright 2011 The University of Chicago Press.

determine the gaseous water abundance in the hot cores through emission lines. Thanks to the high spectral resolution of HIFI, the quiescent core contribution can be separated from the outflow component and analyzed separately. Also, the H₂¹⁷O and H₂¹⁸O lines have low optical depths, facilitating accurate determinations of the water abundances. Most models have used a “jump” abundance profile in which the water abundance increases from a constant low value in the outer envelope (on the order of 10^{-8}) to a high abundance in the warm region, as illustrated in Figure 26. The hot core abundances derived from observations are found to range from values as low as 10^{-6} for some sources³²⁹ to the expected abundance of 10^{-4} for other sources.^{323,330} The low hot core abundances are surprising and are not yet understood. They require a rapid gas-phase destruction mechanism such as UV photodissociation or X-rays,²²² but it is not known whether the fluxes are high enough in these inner shielded regions.

For low-mass protostars, the analysis is complicated by the fact that ISO-SWS did not have the sensitivity to observe these low luminosity sources, whereas the observed Herschel-HIFI lines are dominated by broad emission from outflows (Figures 22 and 28), even for isotopologue lines.^{315,325} Several H₂¹⁸O and H₂¹⁷O lines toward the chemically rich low-mass protostar IRAS 16293–2422 have been interpreted⁶⁹ as originating in a hot core with a water abundance of only 5×10^{-6} . Deep integrations of the excited H₂¹⁸O 3₁₂–3₀₃ line ($E_u/k = 249$ K) near 1095 GHz toward a few other sources reveal a narrow feature that must come from the hot core region.³³¹ Also, the H₂¹⁸O 3₁₃–2₂₀ line

Table 4. Summary of H₂O/H₂ Abundance Determinations in Shocks^a

source	instrument	H ₂ O/H ₂ (10 ⁻⁴)	H ₂ from	ref
Orion-KL	ISO-LWS	5		Harwit et al. ³³⁴
Orion-IRc2	ISO-SWS	2–5	model	Wright et al. ³³⁵
Orion peak 1	ISO-SWS	0.2		Gonzalez-Alfonso et al. ³³⁶
Orion peaks 1 + 2	ISO-LWS	0.2		Cernicharo et al. ³³⁷
Orion-KL	SWAS	3.5		Melnick et al. ²⁷
Orion-KL	Odin	0.1–1		Olofsson et al. ³³⁸
several	Herschel-HIFI	7.4	low- <i>J</i> CO	Melnick et al. ⁶⁷
several	ISO-LWS	0.1–1 (class 0)	high- <i>J</i> CO	Nisini et al. ³⁵⁵
		<0.1 (class I)	high- <i>J</i> CO	Nisini et al. ³⁵⁵
several	SWAS	0.001–0.01 ^b	low- <i>J</i> CO	Franklin et al. ³³⁹
several	Odin	0.003–5 ^b	low- <i>J</i> CO	Bjerkeli et al. ³⁵⁶
HH 54	ISO-LWS	0.1	high- <i>J</i> CO	Liseau et al. ³⁵⁷
HH 54	Herschel-HIFI	0.1 ^b	mid- <i>J</i> CO, H ₂	Bjerkeli et al. ³⁵⁸
L1157 B1	Herschel-HIFI	0.008 (LV) 0.8 (HV)	mid- <i>J</i> CO	Lefloch et al. ³⁴⁰ Lefloch et al. ³⁴⁰
L1157 B2/R	Herschel-HIFI/PACS	0.01	warm H ₂	Vasta et al. ³⁵⁹
L1448 B2/R4	Herschel-HIFI/PACS	0.05–0.1 (HV)	warm H ₂	Santangelo et al. ³⁶⁰
L1448	Herschel-HIFI/PACS	0.005–0.01	warm H ₂	Nisini et al. ³⁴³
VLA1623	Herschel-HIFI	<0.01 ^b	warm H ₂	Bjerkeli et al. ³⁶¹
Several	Herschel-HIFI	0.1 (HV)	low- <i>J</i> CO	Kristensen et al. ³¹⁵
NGC1333 IRAS4B	Herschel-PACS	1.0	warm H ₂	Herczeg et al. ⁶⁸
Serpens SMM1	Herschel-PACS	0.4	high- <i>J</i> CO	Goicoechea et al. ³⁴¹
L1448 several B/R	Herschel-PACS	0.01	warm H ₂	Tafalla et al. ³⁴²
NGC 7129 IRS	Herschel-HIFI/PACS	0.2–0.3	high- <i>J</i> CO	Johnstone et al. ³²⁴ Fich et al. ³⁶²
NGC 6334I	Herschel-HIFI	0.4	mid- <i>J</i> CO	Emprechtinger et al. ³⁶³
DR21(OH)	Herschel-HIFI	0.32 ^c	high- <i>J</i> ¹³ CO	van der Tak et al. ³⁶⁴

^aUncertainties claimed by the authors range from a factor of 2 up to an order of magnitude. HV = high-velocity; LV = low velocity. In most cases, the abundance refers to the outflow at the central source position. B and R indicated blue- and red-shifted outflow spots offset from the source. ^bOrtho-H₂O abundance. ^cFrom para-H₂O assuming ortho/para = 3.

($E_u/k = 204$ K) at 203 GHz has been mapped interferometrically in some of the same sources showing compact narrow emission.^{33,332} While the determination of the hot water column is relatively straightforward from such data if the lines are optically thin (as in the case of the 203 GHz line, but not the 1095 GHz line), the water abundance is much more uncertain due to the uncertain warm H₂ column, which in turn is related to the source structure on scales of 100 AU representative of the hot core. Using independent data from C¹⁸O 9–8 and 10–9, a high water abundance of a few $\times 10^{-5}$ – 10^{-4} has been argued, with values as low as 10^{-6} – 10^{-5} clearly excluded.³³¹

In summary, there is considerable evidence for water ice sublimation in hot cores, but warm water abundance determinations still differ by up to 2 orders of magnitude. Thus, the question whether hot cores are generally “dry” or “wet” due to ice sublimation is still open and may differ from source to source.

4.4. Testing High-Temperature Chemistry

The reaction scheme discussed in section 3.2 predicts that almost all available oxygen not locked up into grains or CO is driven into water at high temperatures.^{232,333} Astronomical regions in which this chemistry can be tested include shocks associated with the outflows from young stars, supernova remnants expanding into the interstellar medium, the warm envelopes around evolved stars, the hot cores around high-mass protostars, the inner zones of protoplanetary disks, and the nuclei of external galaxies. The expected water vapor abundance in these regions is H₂O/H₂ \approx (5–6) $\times 10^{-4}$ (see above), unless photodissociation or reactions with atomic H drive the water back to O and OH (Figure 16). If

all nonrefractory carbon is locked up in CO, the expected H₂O/CO ratio is ~ 1.3 .

4.4.1. Shocks. Orion. The shocked regions in Orion-KL form one of the best test cases of high-temperature chemistry because of the wealth of lines observed at mid- and far-infrared wavelengths. Using ISO-LWS, Harwit et al.³³⁴ detected eight far-infrared water emission lines that indicate H₂O/H₂ $\approx 5 \times 10^{-4}$, consistent with most oxygen driven into H₂O. Other ISO studies of Orion based on many additional absorption and emission lines with the SWS and LWS either came to a similar conclusion³³⁵ or found a lower abundance by a factor of 5–10.^{336,337} Observations of the 1₁₀–1₀₁ 557 GHz line with SWAS and Odin give abundances of 3.5×10^{-4} and 10^{-5} – 10^{-4} , respectively.^{27,338} Differences can be due to different positions targeted in the various studies (central source IRc2 versus outflow positions $\sim 30''$ offset from IRc2), different observing beams (from $\sim 20''$ to $>3'$) containing a range of physical components with uncertain source sizes, different reference species used to compute abundances (H₂ or CO), different conclusions on the optical depths of the lines, and different excitation analyses with infrared radiative pumping included or not.

Most recently, Melnick et al.⁶⁷ observed a plethora of spectrally resolved H₂O, H₂¹⁸O, and H₂¹⁷O lines with Herschel-HIFI (Figure 8) to separate the different physical components and infer abundances of 7.4×10^{-5} , 1.0×10^{-5} , and 1.6×10^{-5} for the shock (“plateau”), hot core, and extended warm gas, respectively. The plateau value is consistent with a significant fraction of the oxygen driven into water, but not all of

it. Either some fraction of oxygen is locked up in unidentified refractory material or photodissociation of H₂O by the intense UV radiation pervading the Orion cloud reduces the water abundance somewhat below its maximum value.

Other Shocks. Table 4 contains a (nonexhaustive) summary of H₂O abundances determined in shocks associated with young stellar objects, using a variety of instruments. The inferred values for sources other than Orion vary by 3 orders of magnitude, with only a few sources consistent with all oxygen driven into water. This has led to the suggestion based on SWAS data that only a small fraction (<1%) of the outflow gas has passed through shocks strong (i.e., hot, >400 K) enough to convert oxygen into water during the lifetime of the shock, primarily the gas at high velocities.³³⁹ A similar conclusion is reached based on Herschel-HIFI data at much higher spatial resolution,³⁴⁰ which suggests³¹⁵ that the water abundance increases with velocity from 10⁻⁷ to 10⁻⁵.

As for Orion, part of the problem in this comparison of results stems from the fact that different methods are used by the various teams to infer the H₂ column. Most studies use low-*J* (*J_u* ≤ 3) CO lines as their reference,^{315,339} but these line wings trace primarily the cool (<100 K) swept-up ambient gas rather than the warm currently shocked gas with temperatures of a few hundred up to few thousand kelvin. If the H₂O line profiles are compared with those of high-*J* (*J_u* > 10) CO, no increase in the water abundance with velocity is seen and the higher abundance of a few ×10⁻⁵ is found (Kristensen, private communication). Alternatively, comparison with warm H₂ columns obtained directly from Spitzer mid-IR data should result in reliable water abundances. Such studies point to high H₂O abundances of ∼10⁻⁴ in the densest, heavily extinguished regions centered on the deeply embedded protostars^{68,341} but to lower H₂O abundances of 10⁻⁷–10⁻⁶ at shock positions offset from the protostars^{342–344} [see Figure 22 (right)]. Thus, there do appear to be real variations in the water (and also CO) abundance in high-temperature gas depending on the conditions.

The explanation for the low H₂O abundances centers again on the presence of UV photons and on the type of shocks involved. Broadly speaking, two classes of shocks occur in interstellar clouds:³⁴⁵ in *J*-shocks, there is sudden jump in the physical variables (temperature, density) at the shock position, and temperatures often reach high enough values (>4000 K) to dissociate most molecules, although nondissociative *J*-shocks exist as well. The gas is significantly compressed in the cooler postshock gas. In C-type shocks, the ions in a magnetic precursor are able to communicate the upcoming shock to the neutrals so that temperature and density vary much more smoothly through the shock and do not dissociate the molecules. In dissociative *J*-type shocks, the H₂O abundance is low,³⁴⁶ in C-type and nondissociative *J* shocks it is high.^{333,347} Analysis of the H₂O excitation in several shock spots offset from the protostar indicates that most of the water emission comes from gas that is overpressured with respect to the surroundings by a factor of ∼10⁴, consistent with *J*-type shocks.^{342,343} Typical temperatures of the water-emitting gas are around 500 K and densities on the order of 10⁷ cm⁻³, and the inferred water abundances are indeed low, down to 10⁻⁷.

One further option to distinguish between the various models is to look at the dissociation products, OH and [O I]. Nondissociative continuous shocks predict OH/H₂O ≪ 1 if photodissociation is negligible. Spectrally resolved data on OH are still sparse, but for one high-mass protostar, a ratio OH/H₂O > 0.03 is found in the outflow.³⁴⁸ From spectrally unresolved data

of the IRAS4B low-mass protostar, OH/H₂O = 0.2 is inferred.⁶⁸ These high ratios, combined with strong emission from [O I] and widespread detection of OH,^{349–352} also point to the presence of dissociative shocks. On the other hand, the high abundance of H₂O at the source position, together with high-*J* CO excitation, indicates the presence of some nondissociative shocks as well.^{341,351} Most likely, a combination of *J*-type shocks and UV-irradiated C-type shocks is needed to explain the data at the various positions. The UV radiation does not have to originate externally from nearby bright stars as in the case of Orion, but it can be produced locally by fast *J*-type shocks.^{353,354} One firm conclusion from all these studies is that UV-irradiated shocks are common near protostars and that a new generation of shock models needs to be developed to interpret the observed abundance ratios.

Alternative explanations for the low H₂O abundance include rapid freeze-out onto grains in the cool postshock gas. For a density of 10⁶ cm⁻³, the time scale is ∼10³ yr, longer than typical shock time scales.²³¹ Thus, freeze-out will not be significant in the still warm postshock gas probed by the Herschel data. Other time-dependent effects can also play a role. Slow C-type shocks with velocities ≤15 km s⁻¹ reach postshock temperatures of only 300–400 K.³³³ The time scale to convert all oxygen into water is >400 yr at such low temperatures, longer than the cooling time of the shock itself, which is less than 100 yr. Coupled with their ineffectiveness in releasing water ice into the gas, slow shocks could have low water abundances. The main argument against this option is that the water line profiles³⁴³ indicate shock velocities higher than 15 km s⁻¹ (Figures 22 and 28).

High-Temperature Chemistry vs Ice Sputtering. The above shock models produce water through the high-temperature neutral–neutral reactions. However, sputtering of ice by high-velocity particles in the shocks is another option, thereby releasing the ice mantle material back into the gas. Models^{232,365} indicate that this becomes effective for shocks faster than 10–15 km s⁻¹. One possibility to distinguish between these two options is to compare observations of H₂O in shocks with those of other grain-surface products. In particular, NH₃ and CH₃OH are also known to be among the abundant ice mantle constituents, with abundances of ∼5% and 1–20% with respect to that of H₂O ice, respectively.²³⁵

High S/N Herschel and ground-based data indicate that for most sources the observed NH₃ and/or CH₃OH emission profiles lack the broad line wings seen for the H₂O lines, implying an absence of these molecules at the highest velocities.^{366,367} This could be taken to imply a lack of ice mantle sputtering. However, Viti et al.³⁶⁸ note that NH₃ and CH₃OH can actually be destroyed by atomic H in high-temperature gas following ice sputtering, whereas H₂O is not. This is because the energy barrier for destroying H₂O by atomic H is much higher, ∼9000 versus ∼5000 and ∼3000 K for NH₃ and CH₃OH, respectively. Thus, ice mantle sputtering is not yet excluded. If this scenario is valid, the lack of NH₃ or CH₃OH would allow the shock temperature to be constrained. Further observational tests of this scenario are needed.

4.4.2. Supernova Remnants. IC 443 is a prototypical example of high-velocity gas ejected by a supernova interacting with the interstellar medium. A molecular cloud lies across the face of the supernova remnant and at locations where the remnant encounters this cloud, shocked molecular gas is revealed by broad asymmetric line profiles. SWAS and ISO data point to a very low abundance of H₂O in the shock, H₂O/CO = (2 × 10⁻⁴)–(3 × 10⁻³) in the downstream gas.³⁵⁴ Only in the warmer

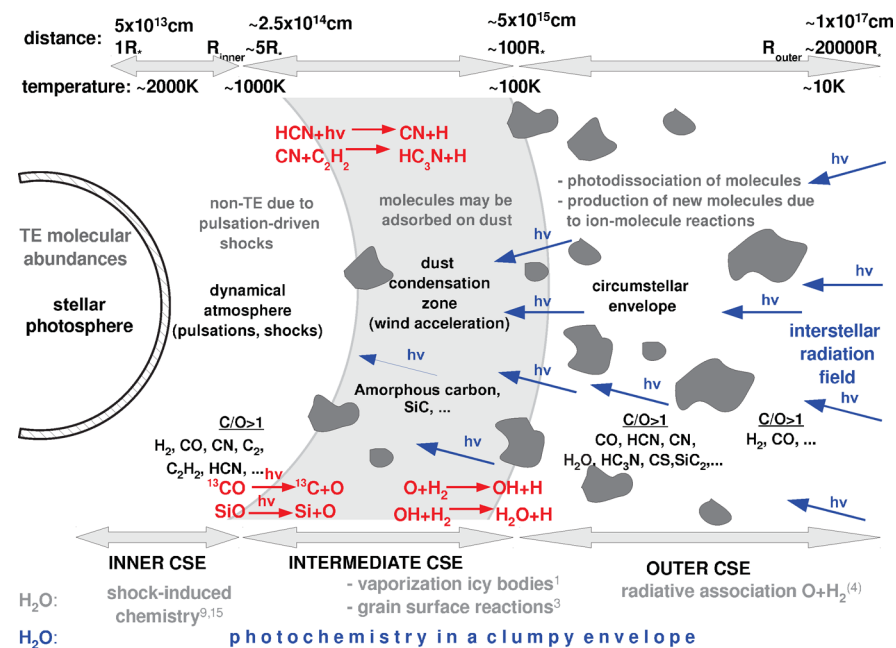


Figure 29. Schematic structure of the envelope of an evolved carbon-rich star. Several chemical processes are indicated at their typical temperatures and radial distances from the star (not to scale). Thermodynamic equilibrium (TE) chemistry defines the abundances in the stellar atmosphere; shock-induced nonequilibrium chemistry can take place in the inner wind envelope; dust–gas and ion–molecule reactions alter the abundances in the intermediate wind zone; penetration of cosmic rays and UV photons dissociates the molecules and initiates an active photochemistry. If the medium is clumpy, the UV radiation can penetrate more deeply (blue arrows). The different mechanisms proposed as origins of water in a carbon-rich environment are indicated at the bottom of the figure in gray at the typical distances where they occur. Reprinted with permission from ref 405. Copyright 2010 Macmillan Publishers Ltd.: Nature.

part of the shock does the ratio reach $\text{H}_2\text{O}/\text{CO} \approx 0.2$. As for the shocks associated with protostars, a combination of freeze-out of H_2O in the pre- and postshock cloud (with slow shocks preventing complete ice sputtering) and photodissociation of H_2O in postshock gas are invoked to explain the low abundances. The UV radiation is thought to be generated by a preceding fast J -type shock. Further evidence for enhanced UV radiation comes from the high C/CO ratio in the preshock gas.³⁶⁹ Compared with dense star-forming clouds, the molecular cloud encountered by IC 443 has a lower density, more like a translucent cloud. The higher H/H₂ ratio in a translucent region could potentially drive reactions that convert H_2O back to O. Similarly, an enhanced cosmic-ray ionization rate could result in higher H/H₂ and C/CO ratios in the preshock gas.³⁷⁰ However, even a very high H/H₂ ratio of 10 drives most oxygen into water since, as noted above, the energy barrier for the $\text{H}_2\text{O} + \text{H}$ back reaction is very high (~ 9000 K).³⁵⁴

Similar conclusions have been reached for other supernova remnants interacting with molecular clouds based on high OH/H₂O ratios.^{371,372}

4.4.3. External Galaxies. The central regions of galaxies contain dense and warm gas, which allow the water chemistry to be tested on scales of a few hundred parsec, as opposed to the subparsec scales in our own galaxy. Following early detections with ISO,^{373,374} a wealth of water lines has now been seen in nearby galaxies ($z < 0.3$) with all three instruments on Herschel.^{291,298,375–381} The lines are sometimes seen in emission and in other cases in absorption against the bright nuclear continuum and arise from levels with E_u/k_B up to 650 K. Water is now even seen at high red-shifts up to $z = 6.3$ ³⁸² with ground-based telescopes^{16,383–386} (see Figure 2). The line luminosities of water are high, only slightly below those of CO.

The water lines in these distant sources arise from a mix of physical components, including the compact nuclear region but also more extended diffuse gas (see section 4.1), so detailed modeling is needed to disentangle them. The warm and dense nuclear regions are found to have high water abundances on the order of 10^{-5} , consistent with high-temperature chemistry and grain mantle sublimation.²⁹¹ In some galaxies, water outflows out to several hundred km s⁻¹ are seen, so shocks can play a role as well.³⁸⁰ The high OH/H₂O ratios of order unity again point to enhanced water dissociation; however, rather than UV radiation, X-rays and/or cosmic rays are invoked.

The ubiquitous detection of high excitation water lines such as $3_{21}-3_{12}$ and $4_{22}-4_{13}$ has been interpreted to imply that pumping by far-infrared continuum radiation due to warm dust plays an important role in the excitation of water in many, but not all,³⁸⁰ of these sources.^{381,384}

4.4.4. Evolved Stars. O-Rich Envelopes. The dense and warm envelopes around dying stars (Figure 1) provide another good laboratory to investigate the high-temperature water chemistry. O-Rich stars have $[\text{O}]/[\text{C}] > 1$, so at densities up to 10^{13} cm^{-3} and temperatures up to 1000 K, most oxygen should be driven into water: since H_2O is the thermodynamically most stable oxygen-containing molecule after CO, its abundance is basically set by the available oxygen reservoir minus the abundance of oxygen locked up in CO. H_2O and OH have been detected for decades in these sources through their maser lines at radio wavelengths.³⁸⁷ These data have led to the development of photochemical models of the envelopes in which thermal equilibrium chemistry dominates in the innermost envelope, but two-body reactions and photodissociation due to UV radiation from the interstellar field become more important in the outer envelope.^{380–391} In the later stages leading up to the planetary nebulae stage, asymmetries and bipolar outflows

develop, the morphology of which is probed by H₂O and OH masers.³⁹²

To quantify the water chemistry, nonmasing lines need to be observed. A wealth of thermal water lines have been detected with ISO toward the evolved stars W Hydrae^{393,394} and VY CMa,³⁹⁵ showing that water is abundant and that the emission originates primarily in the acceleration zone of the dense outflows created by radiation pressure on the dust grains. The presence of OH illustrates the importance of photodissociation at larger distances from the star. A physical model of the W Hydrae envelope has been used to infer H₂O/H₂ = 8 × 10⁻⁴ in the innermost layers and 3 × 10⁻⁴ at larger radii.³⁹³ Comparable values have been found in other studies based on ISO data.^{396–398} Alternatively, rather than testing the oxygen chemistry, the water observations can be used to make independent estimates of the temperature structure and mass loss rates.³⁹⁴

Spectrally resolved lines of H₂O and its isotopologues with Herschel-HIFI provide the next step forward in the modeling of the water chemistry in these sources. The best studied case so far is IK Tau, for which an abundance ortho-H₂O/H₂ = 5 × 10⁻⁵ has been derived.³⁹⁹ The abundance is consistent with thermodynamic equilibrium chemistry and does not require other processes that have been proposed, such as pulsationally induced nonequilibrium chemistry or grain surface chemistry via Fischer-Tropsch catalysis.⁴⁰⁰

For the star χ Cyg, which has [C]/[O] ≈ 1, a water abundance H₂O/H₂ = 1.1 × 10⁻⁵ has been found with Herschel-HIFI, much lower than in O-rich stars.⁴⁰¹ This implies that the bulk of the oxygen in this source is locked up in CO rather than in H₂O and that [C]/[O] ≤ 0.98.

C-Rich Envelopes. Water was not expected to be detected in the envelopes of C-rich stars with [C]/[O] > 1, since all free oxygen should be locked up in the very stable CO molecule. The detection of the H₂O 557 GHz line toward the C-rich star IRC +10216 with SWAS⁴⁰² (and subsequently Odin⁴⁰³) therefore came as a surprise. It has been speculated that the cold water could result from sublimating icy bodies orbiting the star in an analog of the Kuiper Belt in our own solar system.^{402,404} However, the subsequent Herschel detection of a multitude of warm water lines⁴⁰⁵ combined with their line profiles⁴⁰⁶ argues against the vaporization of ices and favors a scenario in which periodic high-temperature shocks⁴⁰⁷ and/or UV penetrating in a clumpy medium⁴⁰⁵ liberate oxygen from CO in the inner envelope and drive it into water (Figure 29). Detection of water in C-rich evolved stars is now found to be common,⁴⁰⁸ with inferred H₂O/H₂ abundances ranging from 8 × 10⁻⁸ to 2 × 10⁻⁶.

4.4.5. Inner Protoplanetary Disks. The inner few astronomical units of protoplanetary disks around young stars have very high temperatures (>few hundred kelvin) and densities (>10¹¹ cm⁻³) near the midplane. Under these conditions, the chemistry is close to thermodynamic equilibrium and most of the oxygen will be driven into water. This warm water reservoir is denoted as region 1 in the study by Woitke et al.⁴⁰⁹ and illustrated in Figure 30. As pointed out by Bethell and Bergin,⁴¹⁰ the water column in the upper layers is so large that the UV absorption optical depth becomes greater than unity so that water can shield itself from the dissociating stellar radiation and have an even higher abundance at intermediate heights.

At somewhat larger distances (out to 30 AU, depending on the type of star) and higher up in the disk atmosphere, the chemistry is no longer in thermodynamic equilibrium but controlled by two-body processes. In these upper layers, the gas temperature is

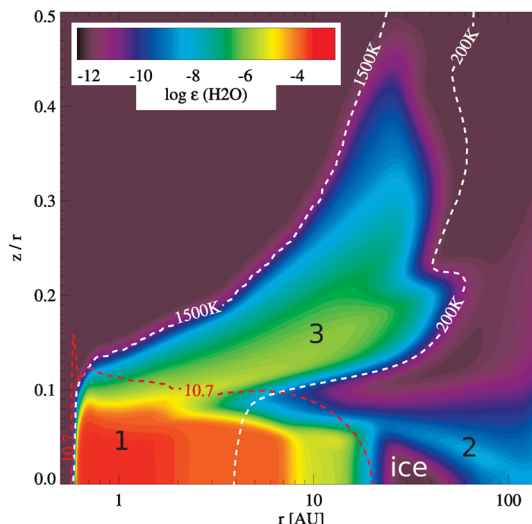


Figure 30. Abundance of water vapor relative to total hydrogen as a function of both radial distance r and relative height above the midplane z/r for a disk around an A-type star (T_* = 8600 K). Three regions with high H₂O abundance can be distinguished. Regions 1 and 3 involve high-temperature chemistry, whereas region 2 lies beyond the ice line and involves photodesorption of water ice (see also Figure 27). The white contours indicate gas temperatures of 200 and 1500 K, whereas the red contour shows the $n_H = 5 \times 10^{10} \text{ cm}^{-3}$ density contour. Reprinted with permission from ref 409. Copyright 2009 European Southern Observatory.

significantly higher than the dust temperature, typically 300–2000 K. Thus, the energy barriers for the neutral–neutral reactions of O + H₂ and OH + H₂ are readily overcome and H₂O is rapidly produced^{411–413} (region 3 in Figure 30). In the uppermost surface layers, water is even more rapidly destroyed by photodissociation and reactions with atomic H than it is produced, so there is little water at the very top of the disk. The bulk of the warm water reservoir therefore lies at intermediate heights in the disk, where it is shielded from the most intense stellar UV radiation. The cold water reservoir, region 2 in Figure 30, is discussed in section 4.2.3.

The warm water reservoir in the inner regions of disks has been detected using the Spitzer-IRS through highly excited pure rotational lines at mid-infrared wavelengths^{72–74,414,415} (Figure 9) and through ground-based near-infrared vibration rotation lines^{73,416} (Figure 31). Abundance ratios are difficult to extract from the observations because the lines are highly saturated and in the case of Spitzer data spectrally unresolved, but abundance

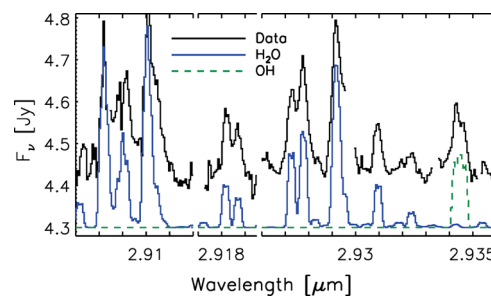


Figure 31. Example of vibration–rotation lines of H₂O observed with Keck-NIRSPEC arising in the warm water reservoir in the inner AU of the AS 205 protoplanetary disk. Adapted with permission from ref 73. Copyright 2008 American Astronomical Society.

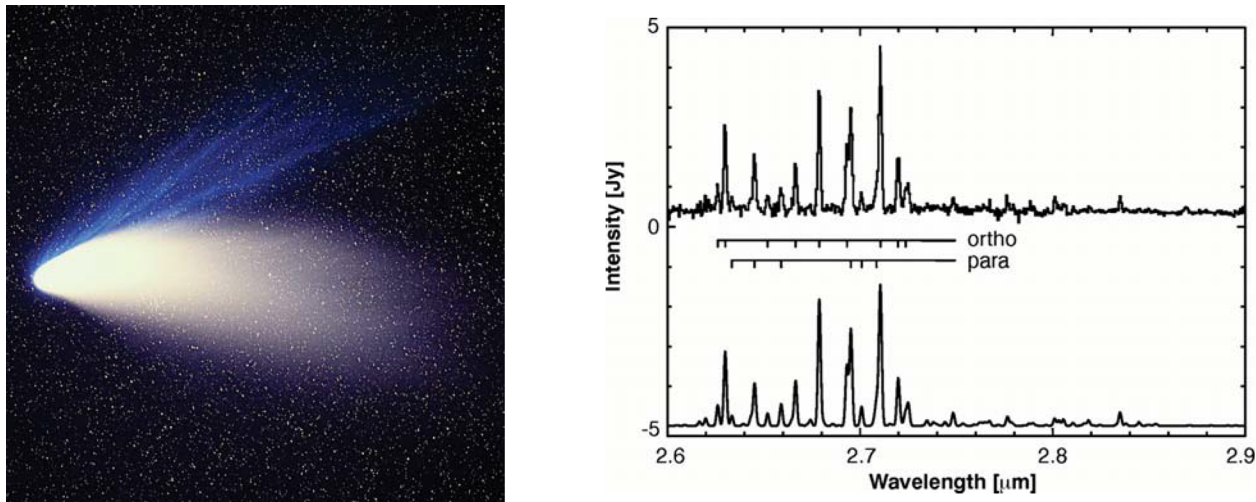


Figure 32. (Left) Image of comet C/1995 O1 Hale-Bopp taken on April 4 1997 by E. Kolmhofer and H. Raab (www.sternwarte.at) and reproduced with their permission. (Right) H_2O vibration–rotation lines of comet Hale-Bopp observed with the ISO-SWS. Reprinted with permission from ref 429. Copyright 1997 American Association for the Advancement of Science.

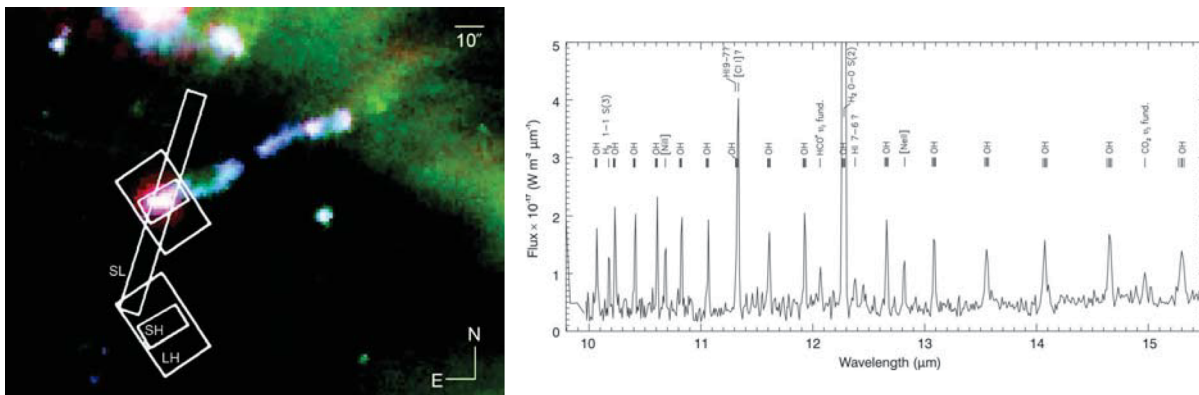


Figure 33. (Left) Spitzer infrared image of the HH 211 jet and bow shock with the IRS spectrometer slits overlaid (blue = $3.6 + 4.5 \mu\text{m}$, green = $8 \mu\text{m}$, red = $24 \mu\text{m}$). (Right) Spitzer-IRS spectrum of HH 211 at the bow shock (red tip). The OH lines originate from levels up to $J = 69/2$. Reprinted with permission from refs 437 and 438. Copyright 2008 and 2012 American Astronomical Society.

ratios of $\text{H}_2\text{O}/\text{CO} \sim 1\text{--}10$ have been inferred for emitting radii up to a few astronomical units.^{415,416} Within the more than an order of magnitude uncertainties, these values are consistent with the model predictions for the warm layers (Figure 30). The Spitzer and near-IR data show a clear dichotomy between disks around the cooler T Tauri stars ($T_* \lesssim 5000 \text{ K}$), where H_2O is detected, and those around the hotter A-type stars ($T_* \sim 8000\text{--}10\,000 \text{ K}$), where it is usually not, presumably due to the more rapid photodissociation in the latter case producing the observed OH.^{74,417}

Longer wavelength observations with Herschel-PACS probe gas further out into the disk. Far-infrared lines from warm water have been detected in some sources, mostly around T Tauri stars^{418,419} but also a few A-type stars.^{420–422} Together with the shorter and longer wavelength water data (see section 4.2.3), these observations can be used to constrain the water ice line in disks.^{124,418}

In summary, the observations of a wide range of sources confirm that water can be produced in copious amounts by a combination of high-temperature chemistry and ice mantle sublimation and sputtering. However, a common finding in all of these regions is that the water abundance is lower than expected if all oxygen were driven into water, by up to 2–3 orders of

magnitude, and that the OH/ H_2O ratios are correspondingly higher than expected. This indicates that destructive radiation (UV, X-rays, and/or cosmic rays) plays a significant role in limiting the water abundance and must be included in the next generation of models.

4.5. Testing Photodissociation Models

4.5.1. Comets. Comets are small (a few kilometers in diameter) solid bodies in the outer solar system consisting of ice (mostly water), dust, and small rocky particles. When they come close to the Sun, the solids are heated up and the ices sublimate into the gas, creating the coma and tails that emit visible radiation due to the fluorescence of small molecules (Figure 32). The solar radiation also dissociates the “parent” molecules that originate from the cometary ices into “daughter” molecules.^{423,424} Specifically, H_2O is photodissociated into OH, which in turn photodissociates into O. The OH radical can readily be observed through its 18 cm radio hyperfine/Λ-doubling transitions. The photodissociation model is then used to infer the original H_2O production rate in the cometary coma.^{425–429} This requires an accurate determination of the H_2O and OH photodissociation rates by the solar radiation.

The radiation field of the Sun ($T_* = 5780 \text{ K}$) peaks at visible wavelengths and has relatively few photons at UV wavelengths

where molecules like H₂O and OH can absorb and dissociate. The main photodissociation channel of H₂O is therefore through solar Lyman α radiation, which can excite H₂O into the $\tilde{\text{B}}$ electronic state. As discussed in section 3.1.3, this process leads to OH in very high rotational levels as well as some vibrational excitation. This “prompt” emission of vibrationally and rotationally excited OH produced directly from H₂O photodissociation (in contrast to the fluorescently pumped OH emission) has been detected in several comets.^{430–432} If the production rates into the various OH states are well-known, the observed emission can be calibrated to provide an alternative method to determine the H₂O release from the comet nucleus.^{433,434} Longer wavelength radiation at 1570 Å photodissociates H₂O through the $\tilde{\Lambda}$ state and has been experimentally found to produce population inversion in OH with a strong preference for populating the upper Λ -doubling state.⁴³⁵ However, this mechanism is unlikely to be responsible for the bulk of the observed OH emission in comets.

4.5.2. Bow Shocks. Another example of OH prompt emission following photodissociation is found in some shocked regions. The most powerful shocks occur at the tip of the outflows, where the jet rams into the surrounding cloud with velocities up to several hundred kilometers/second. At these so-called bow shocks, the gas temperature increases up to 10⁵ K, resulting in dissociation of molecules and ionization of atoms. As the gas cools, the atomic ions recombine with electrons and emit UV radiation, specifically Lyman α photons.^{346,436} These photons dissociate H₂O produced further downstream in the cooling gas through the $\tilde{\text{B}}$ electronic state, producing highly rotationally excited OH. This scenario has been nicely confirmed by the detection of OH pure rotational lines up to $J = 69/2$ in the HH 211 outflow using Spitzer-IRS^{437,438} (see Figure 33).

In summary, the observed state-resolved OH product distribution leaves no doubt that photodissociation of water by Lyman α photons occurs in these regions. This is a beautiful example of detailed molecular physics and astronomy going hand-in-hand in enhancing our understanding of the universe.

4.6. Water Ortho-to-Para Ratio

Observations of water in space also provide constraints on the ortho/para ratio (OPR) of water in the gas, which in turn could tell astronomers something about the conditions, formation, or thermal history of water in specific regions. An alternative way to describe the OPR is through the “spin temperature”, defined as the temperature that characterizes the observed OPR if it were in thermal equilibrium. The OPR becomes zero in the limit of low temperature and 3 in the limit of high temperature. For $T \geq 50$ K, the equilibrium OPR exceeds 2.95, while for $T \leq 25$ K, the OPR is well-approximated by $9 \exp(-\Delta E/kT) = 9 \exp(-34.2 \text{ K}/T)$, where ΔE is the energy difference between the 1_{01} and 0_{00} rotational states. This expression applies specifically to the gas phase, in which the molecule is free to rotate; the relationship between the temperature and the equilibrium OPR may be different if the molecule is rotationally hindered.⁴³⁹

Accurate measurements of the OPR have been made for diffuse and translucent clouds by combining absorption line observations of optically thin 557 and 1113 GHz transitions. In a study of 13 translucent clouds observed with Herschel-HIFI, Flagey et al.²⁸⁹ derived a mean OPR of 2.9, very close to the value of 3 expected from nuclear spin statistics in thermal equilibrium in the limit of high temperature. While 10 of the 13 clouds exhibited an OPR consistent with 3, one had a measured OPR significantly larger than three (4.3 ± 0.2), and two had OPRs

significantly smaller than 3 (2.3 ± 0.1 and 2.4 ± 0.2). Gas-phase ion molecule chemistry is expected to produce a ratio close to 3: the dissociative recombination of H₃O⁺ with electrons to produce H₂O, the dominant channel leading to water in these clouds, has several electron volts of excess energy, and the nuclear spins should be produced in the statistical high temperature ratio, although a detailed calculation using the angular momentum approach of Oka⁴⁴⁰ should be used to check this assumption. Exchange reactions of H₂O with H⁺ can further drive the OPR to the kinetic temperature if these reactions are rapid enough compared with the lifetime of the cloud.

In shocks and evolved stars where the water lines are seen in emission, it is difficult to measure the OPR with the same precision as for translucent clouds, even though many lines of both ortho- and para-H₂O have been observed. Nevertheless, all analyses so far^{67,68,329,399} are consistent with an OPR of 3, as expected for hot water. Similarly, the data on warm water detected at mid-infrared wavelengths in the inner regions of protoplanetary disks⁷⁴ are consistent with OPR = 3. In contrast, the OPR of cold water seen with Herschel-HIFI in the outer regions of disks²⁸⁴ imply an OPR < 1 (Figure 34), although smaller emitting areas and correspondingly higher optical depths than assumed in the original analysis could drive the observed ratios closer to 3.

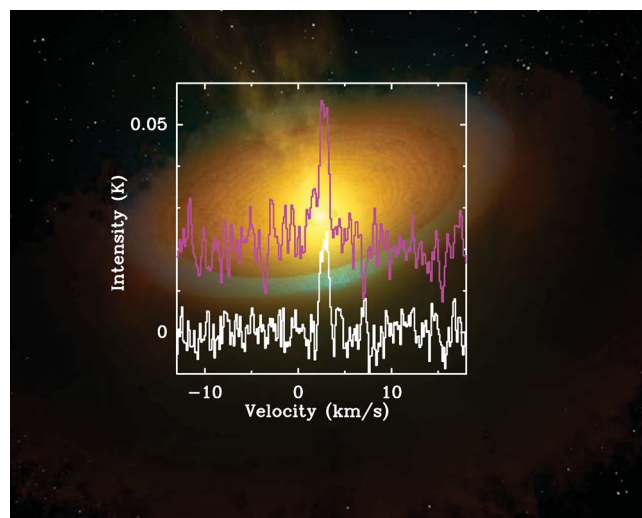


Figure 34. Emission lines of ortho-H₂O ($1_{10} - 1_{01}$ at 557 GHz) and para-H₂O ($1_{11} - 0_{00}$ at 1113 GHz) observed with Herschel-HIFI toward the TW Hya disk. The para-H₂O line is offset for clarity. Adapted with permission from ref 284. Copyright 2011 American Association for the Advancement of Science. Background image: cartoon of the TW Hya disk (credit ESA/NASA/JPL-Caltech).

Finally, near-infrared cometary spectra such as shown in Figure 32 allow an accurate determination of the OPR. More than a dozen comets have now been measured, with inferred OPRs ranging from 2.4 to 3. A summary is presented in Figure 10 of Mumma and Charnley;⁴⁴¹ the OPRs correspond to spin temperatures as low as ~20 K. These spin temperatures have often been interpreted as a measure of the temperature at which molecules formed, or condensed, on the grain surfaces providing potentially a measure of where the comets formed in the solar nebula. However, this interpretation assumes that the nuclear spins of water equilibrate to the grain temperature by some mechanism and that the OPR is preserved upon sublimation.

These assumptions are discussed in the review by Hama and Watanabe in this issue (<http://dx.doi.org/10.1021/cr4000978>) (see also Dulieu²⁵¹) and are being heavily debated by molecular physicists and astronomers. Recent laboratory measurements of water molecules isolated in solid Ar matrices at 4 K, initially prepared as pure para-H₂O,⁴⁴² show a thermal OPR upon heating to 260–280 K. Similarly, studies of vapor deposited water at low temperatures show a thermal OPR upon sublimation at 150 K, even if the water is kept at 8 K for several days.⁴⁴³ These data suggest that spin conversion of water clusters and water ice is fast upon heating and that the OPR retains no history of the formation temperature.

In the outer regions of protoplanetary disks, the water vapor is produced by photodesorption, not thermal sublimation. To what extent does the process of photodesorption preserve the OPR in the ice? As discussed in section 3.3.3, there are two possible mechanisms for water produced by photodesorption, following dissociation of H₂O ice into H + OH: (i) recombination of H + OH → H₂O in the ice, which then has enough energy to desorb, and (ii) the kick-out mechanism where the energetic H atom kicks out a neighboring H₂O molecule on picosecond time scales. In option i, the H–OH bond is broken and re-formed, so the OPR should go to the statistical value of 3. In option ii, no bond is broken and the original OPR in the ice should be preserved. The relative importance of options i and ii depends on the ice monolayer and to a lesser extent on the ice temperature, but they are roughly of equal importance.²⁵⁹ Thus, even if the water OPR in the ice were low, say ≤ 0.5 , the gas-phase OPR of the photodesorbed H₂O would be significantly higher, about 2, but still lower than 3.

In summary, the molecular processes that lead to ortho/para equilibration, and the time scale for those processes relative to relevant astrophysical time scales, are still poorly understood. More laboratory work on both the gas-phase and grain-surface processes that convert nuclear spins is needed. The results so far indicate that water spin temperatures measured in comets and disks may tell astronomers less about the water formation location than previously thought (see also discussion in Tielens³⁸).

5. CONCLUDING REMARKS

In this review, we have illustrated the major facets of the interdisciplinary science of astrochemistry by consideration of one relatively small but important molecule: water. A critical molecule for life as we know it, water is found to a greater or lesser extent in almost all environments studied in some detail by astrochemists, be it in the gas or condensed phase. Since it is made of two of the most abundant elements, H and O, its formation is to some degree inevitable, yet its chemistry is found to be varied, depending on physical conditions. Indeed, the water vapor abundance is found to be high, about 10^{-4} with respect to H₂ in warm sources such as dense shocks, oxygen-rich circumstellar shells, and inner disks. Its abundance drops to $\sim 10^{-7}$ in diffuse clouds due to photodissociation and is even lower, $\sim 10^{-9}$, in cold cores and the outer regions of protoplanetary disks due to freeze-out. In contrast, water ice is a major reservoir of oxygen in these latter regions, at an abundance of 10^{-4} .

The three main sets of chemical processes thought to form and destroy water can be tested against observations from these different sources. In some types of sources, agreement between models and observations is good, at the level of a factor of 2–3, but in other regions there is a difference of a few orders of

magnitude. In the latter cases, the large disagreement can point to missing chemical reactions in the models, but it can also be caused by observational difficulties in determining the abundances.

The discussion of the three main sets of chemical processes—low temperature ion–molecule and grain-surface reactions and high-temperature neutral–neutral gas-phase reactions—and their use in chemical simulations should give the reader an understanding of the role of these chemical processes. Such simulations can be used to confirm or identify not only the driving chemical processes but also the physical conditions, homogeneous or heterogeneous, of the sources where water is observed and the amount of UV radiation or cosmic rays, and even tell us something of the history and/or fate of these sources. In this sense, chemistry helps astronomy, via spectroscopy and chemical kinetics and via theory and experiment, and it enhances greatly the scientific return from the major investments made in ground- and space-based telescopes.

Enormous progress has clearly been made in the last decades in quantifying molecular processes involving water, but there continues to be further astronomical need for basic data. Examples include spectroscopy of water vapor and its isotopologues at high temperatures for use in exoplanet and disk atmosphere models; collisional rate coefficients for H₂O vibration–rotation transitions and for H₂O with H for use in inner disk and dissociative shock models; an independent check of the branching ratio for dissociative recombination of H₃O⁺ to water for benchmarking diffuse cloud chemistry; state-resolved rate coefficients for high-temperature neutral–neutral reactions in shocks and in the surface layers of disks; and determination of the OH vibration–rotation populations as function of wavelength following H₂O photodissociation for applications in comets, disks, and shocks. In terms of water ice formation, the main uncertainties are illustrated in Figure 17, and more generally, further work is required in the translation of laboratory data to quantities to be used in gas–grain models. There is clearly a major need for wavelength-dependent photodesorption rates of H₂O and OH from water ice to analyze water vapor observations of cold cores and the outer regions of disks. Also, the chemical desorption process and its efficiency needs to be quantified and understood.

To audiences of chemists, it must be pointed out that astronomy has and will continue to aid chemistry in making chemists aware that some of the standard chemical curriculum is terrestrially biased, and that “exotic” molecules (e.g., gaseous cations, anions, three-membered rings, etc.) and “exotic” chemical processes (e.g., dissociative recombination leading to water, radiative association) not normally studied in the chemical laboratory are of great importance in the universe as a whole. Indeed, the use of the word exotic may be more applicable to our home planet than to the interstellar medium! Similarly, there has been a surprising lack of chemical physics studies of water ice formation until astronomers developed the field of solid-state astrochemistry using surface science techniques. Much of the terrestrial chemistry had focused on thin, monolayer experiments, often on metallic surfaces rather than on thick ices. Our increase in knowledge of several of these fundamental chemical processes has at least partially come about because chemists learned of their likely importance to astronomy, and water is an excellent case. More examples are likely to follow.

Regarding the role of water in the new science of astrobiology, astrochemistry has taught us much of relevance. Astrobiology is the study of the origin, evolution, distribution, and future of life in

the universe. Water is commonly implicated as a prerequisite for carbon-based life as found on Earth. We know that water is found in many diverse sources, which certainly does not help to constrain the location where life could form, but it does indicate that the conditions for life are widespread throughout the universe. We also know that in the colder regions that lie along the evolutionary trail of star and planetary formation (Figure 1), water is mainly in its solid form and is likely to be incorporated in this form into the larger solid objects eventually formed from interstellar grains, such as comets and asteroids.²⁸⁰ Indeed, the terrestrial oceans have likely have come from cometary and asteroidal bombardment, and solar system structures such as the Oort cloud and Kuiper Belt may well be common. Equally related to astrobiology, the existence of gaseous water in exoplanets has recently been observed (Figure 3), and the first generation of chemical simulations of this chemistry are already being undertaken. Eventually, we will have a much better understanding of the trail of water from stellar atmospheres to diffuse clouds to dense clouds, protostars, protoplanetary disks, and new generations of stars and planets, all the way out to the edge of the universe. By then, the science of astrochemistry will have progressed from its essential beginnings in the 1970s to a full-fledged science capable of helping astronomers understand the universe to a degree not recognizable today.

AUTHOR INFORMATION

Corresponding Author

*E-mail: ewine@strw.leidenuniv.nl; eh2ef@virginia.edu; neufeld@pha.jhu.edu.

Notes

The authors declare no competing financial interest.

Biographies



Ewine F. van Dishoeck is Professor of Molecular Astrophysics at Leiden University, the Netherlands, where she studied chemistry and received her Ph.D. in Astronomy in 1984 under co-guidance from Alexander Dalgarno. She is also an external scientific member of the Max Planck Institut für Extraterrestrische Physik in Garching, Germany. Following postdoctoral and visiting positions at Harvard and Princeton, she was appointed as an Assistant Professor in Cosmochemistry at the California Institute for Technology in 1988. In 1990, she moved back to Leiden University. Her research group is centered on the astrochemical evolution from clouds to planet-forming disks combined with studies of basic molecular processes. From 1992 until 2007, she was director of the Raymond & Beverly Sackler Laboratory for Astrophysics at Leiden Observatory, in which processes in icy grain mantles are simulated. She holds many national and international science policy functions, including promoting astrochemistry through the International Astro-

nomic Union. As leader of the “Water In Star-forming regions with Herschel” (WISH) key program her research has focused on water over the last decade (www.strw.leidenuniv.nl/WISH). She has been fortunate to work with many excellent students and postdocs and to receive several prestigious awards, including the Dutch Spinoza award (2000) and the Dutch Academy prize (2012). She is a member of the Dutch Royal Academy of Sciences, a Foreign Associate of the US National Academy of Sciences, and a Foreign Member of the American Academy of Arts and Sciences.



Eric Herbst is currently Commonwealth Professor of Chemistry at the University of Virginia, where he also holds courtesy appointments in astronomy and physics. He received his Ph.D. from Harvard University in 1972, working under William Klemperer in molecular beam spectroscopy. After a postdoctoral position at Harvard, during which he became interested in astrochemistry, he worked as a postdoctoral fellow with Carl Lineberger in laser photodetachment. His first academic employment was at the College of William and Mary; in 1980 he moved to Duke University, where he started his first appointment in the Physics Department. Eleven years later, he moved to the Department of Physics at the Ohio State University, where he remained for 20 years, until his return to chemistry at the University of Virginia. His current research interests center on astrochemistry, especially the simulation of the chemistry that occurs in interstellar clouds as portions of them collapse to form new stars and planets. He is a Fellow of the Royal Society of Chemistry (UK), from which he was awarded the Centenary Award.



David Neufeld was introduced to astrochemistry by Prof. Alexander Dalgarno, who was his thesis advisor at Harvard University from 1983 to 1987. After a postdoctoral position at the University of California, Berkeley, he joined the faculty of Johns Hopkins University in 1990, where he is now a Professor of Physics and Astronomy. His research interests include molecular astrophysics, astrochemistry, astrophysical masers, and infrared and submillimeter astronomy. Over the past 25 years, he has had a special thirst for anything involving astrophysical

water, which he has pursued both through theoretical investigations as well as observational studies with the Hubble, ISO, SWAS, Spitzer, and Herschel satellite observatories; to date, 62% of his refereed publications contain the word “water” in the abstract.

ACKNOWLEDGMENTS

The authors thank many colleagues for fruitful discussions on water chemistry and observations. We are particularly grateful to all the physicists and chemists that have provided key molecular data to analyze and interpret observations of water in space. Magnus Persson and Lars Kristensen provided support with figures, whereas Adwin Boogert, Qiang Chang, Thanja Lamberts, Gary Melnick, and Colette Salyk kindly adapted their figures for this review. David Hollenbach, Alain Baudry, Javier Goicoechea, Lars Kristensen, Geoff Mathews, Joe Mottram, Amiel Sternberg, Ruud Visser, and three anonymous referees provided detailed comments that have improved this paper. E.F.v.D. is supported by The Netherlands Organization for Scientific Research (NWO), The Netherlands Research School for Astronomy (NOVA), by a Royal Netherlands Academy of Arts and Sciences (KNAW) professor prize, and by a European Union A-ERC grant 291141 CHEMPLAN. E.H. acknowledges the National Science Foundation for its support of his program in astrochemistry and NASA for support through its Exobiology and Evolutionary Biology program and its program in Herschel science.

REFERENCES

- (1) Steigman, G. *Annu. Rev. Nucl. Part. Sci.* **2007**, *57*, 463.
- (2) Hinshaw, G.; et al. *Astrophys. J., Suppl. Ser.* **2013**, *57*, 463.
- (3) Planck Collaboration; Ade, P. A. R.; Aghanim, N.; Armitage-Caplan, C.; Arnaud, M.; Ashdown, M.; Atrio-Barandela, F.; Aumont, J.; Baccigalupi, C.; Banday, A. J.; et al. *arXiv e-prints*: 1303.5062, **2013**.
- (4) Solomon, P. M.; Klemperer, W. *Astrophys. J.* **1972**, *178*, 389.
- (5) Herbst, E.; Klemperer, W. *Astrophys. J.* **1973**, *185*, 505.
- (6) van de Hulst, H. C. In *Molecules in Astrophysics: Probes & Processes*; IAU Symposium 178; van Dishoeck, E. F., Ed.; Kluwer: Dordrecht; 1996; Vol. 178; p 13.
- (7) Allen, M.; Robinson, G. W. *Astrophys. J.* **1977**, *212*, 396.
- (8) Tielens, A. G. G. M.; Hagen, W. *Astron. Astrophys.* **1982**, *114*, 245.
- (9) Hollenbach, D.; Kaufman, M. J.; Bergin, E. A.; Melnick, G. J. *Astrophys. J.* **2009**, *690*, 1497.
- (10) Cernicharo, J.; Crovisier, J. *Space Sci. Rev.* **2005**, *119*, 29.
- (11) Melnick, G. J. In *Submillimeter Astrophysics and Technology*; Astronomical Society of the Pacific Conference Series; Lis, D. C., Vaillancourt, J. E., Goldsmith, P. F., Bell, T. A., Scoville, N. Z., Zmuidzinas, J., Eds.; Astronomical Society of the Pacific: San Francisco; 2009; Vol. 417; p 59.
- (12) Bergin, E. A.; van Dishoeck, E. F. *Philos. Trans. R. Soc., A* **2012**, *370*, 2778.
- (13) Cheung, A. C.; Rank, D. M.; Townes, C. H. *Nature* **1969**, *221*, 626.
- (14) Miyoshi, M.; Moran, J.; Herrnstein, J.; Greenhill, L.; Nakai, N.; Diamond, P.; Inoue, M. *Nature* **1995**, *373*, 127.
- (15) Birkby, J. L.; de Kok, R. J.; Brogi, M.; de Mooij, E. J. W.; Schwarz, H.; Albrecht, S.; Snellen, I. A. G. *Mon. Not. R. Astron. Soc.* **2013**, *436*, L35.
- (16) Weiß, A.; et al. *Astrophys. J.* **2013**, *767*, 88.
- (17) Seager, S.; Deming, D. *Annu. Rev. Astron. Astrophys.* **2010**, *48*, 631.
- (18) Madhusudhan, N.; Seager, S. *Astrophys. J.* **2009**, *707*, 24.
- (19) Fraser, H. J.; Collings, M. P.; McCoustra, M. R. S.; Williams, D. A. *Mon. Not. R. Astron. Soc.* **2001**, *327*, 1165.
- (20) Gillett, F. C.; Forrest, W. J. *Astrophys. J.* **1973**, *179*, 483.
- (21) Whittet, D. C. B. *Dust in the Galactic Environment*, 2nd ed.; Institute of Physics Publishing: Bristol, 2003.
- (22) Caselli, P.; Ceccarelli, C. *Astron. Astrophys. Rev.* **2012**, *20*, 56.
- (23) Ceccarelli, C.; Caselli, P.; Bockelée-Morvan, D.; Mousis, O.; Pizzarelli, F.; Robert, F.; Semenov, D. In *Protostars & Planets VI*; Beuther, H., Klessen, R., Dullemond, K., Henning, Th., Eds.; University of Arizona Press: Tucson, AZ, 2013; submitted.
- (24) de Graauw, T.; et al. *Astron. Astrophys.* **1996**, *315*, L49.
- (25) Clegg, P. E.; et al. *Astron. Astrophys.* **1996**, *315*, L38.
- (26) van Dishoeck, E. F. *Annu. Rev. Astron. Astrophys.* **2004**, *42*, 119.
- (27) Melnick, G. J.; et al. *Astrophys. J. Lett.* **2000**, *539*, L77.
- (28) Nordh, H. L.; et al. *Astron. Astrophys.* **2003**, *402*, L21.
- (29) Pilbratt, G. L.; Riedinger, J. R.; Passvogel, T.; Crone, G.; Doyle, D.; Gageur, U.; Heras, A. M.; Jewell, C.; Metcalfe, L.; Ott, S.; Schmidt, M. *Astron. Astrophys.* **2010**, *518*, L1.
- (30) de Graauw, T.; et al. *Astron. Astrophys.* **2010**, *518*, L6.
- (31) Poglitsch, A.; et al. *Astron. Astrophys.* **2010**, *518*, L2.
- (32) Cernicharo, J.; Thum, C.; Hein, H.; John, D.; Garcia, P.; Mattioco, F. *Astron. Astrophys.* **1990**, *231*, L15.
- (33) Jørgensen, J. K.; van Dishoeck, E. F. *Astrophys. J. Lett.* **2010**, *710*, L72.
- (34) Houck, J. R.; et al. *Astrophys. J., Suppl. Ser.* **2004**, *154*, 18.
- (35) Young, E. T.; et al. *Astrophys. J. Lett.* **2012**, *749*, L17.
- (36) Spaans, M.; Neufeld, D.; Lepp, S.; Melnick, G. J.; Stauffer, J. *Astrophys. J.* **1998**, *503*, 780.
- (37) Tielens, A. G. G. M. *The Physics and Chemistry of the Interstellar Medium*; Cambridge University Press: Cambridge, 2005.
- (38) Tielens, A. G. G. M. *Rev. Mod. Phys.* **2013**, *85*, 1021.
- (39) Tielens, A. G. G. M.; Hollenbach, D. *Astrophys. J.* **1985**, *291*, 722.
- (40) van Dishoeck, E. F.; et al. *Publ. Astron. Soc. Pac.* **2011**, *123*, 138.
- (41) Mottram, J. C.; Hoare, M. G.; Davies, B.; Lumsden, S. L.; Oudmaijer, R. D.; Urquhart, J. S.; Moore, T. J. T.; Cooper, H. D. B.; Stead, J. *J. Astrophys. J. Lett.* **2011**, *730*, L33.
- (42) Habing, H. J. *Bull. Astron. Netherlands* **1968**, *19*, 421.
- (43) Draine, B. T. *Astrophys. J., Suppl. Ser.* **1978**, *36*, 595.
- (44) Bergin, E. A.; Kaufman, M. J.; Melnick, G. J.; Snell, R. L.; Howe, J. *Astrophys. J.* **2003**, *582*, 830.
- (45) van Dishoeck, E. F.; Jonkheid, B.; van Hemert, M. C. *Faraday Discuss.* **2006**, *133*, 231.
- (46) van Dishoeck, E. F.; Black, J. H. *Astrophys. J.* **1982**, *258*, 533.
- (47) Hauschildt, P. H.; Allard, F.; Ferguson, J.; Baron, E.; Alexander, D. *R. Astrophys. J.* **1999**, *525*, 871.
- (48) Roberge, W. G.; Jones, D.; Lepp, S.; Dalgarno, A. *Astrophys. J., Suppl. Ser.* **1991**, *77*, 287.
- (49) Rachford, B. L.; et al. *Astrophys. J., Suppl. Ser.* **2009**, *180*, 125.
- (50) Bohlin, R. C.; Savage, B. D.; Drake, J. F. *Astrophys. J.* **1978**, *224*, 132.
- (51) Prasad, S. S.; Tarafdar, S. P. *Astrophys. J.* **1983**, *267*, 603.
- (52) Gredel, R.; Lepp, S.; Dalgarno, A.; Herbst, E. *Astrophys. J.* **1989**, *347*, 289.
- (53) Shen, C. J.; Greenberg, J. M.; Schutte, W. A.; van Dishoeck, E. F. *Astron. Astrophys.* **2004**, *415*, 203.
- (54) Bruderer, S.; Doty, S. D.; Benz, A. O. *Astrophys. J., Suppl. Ser.* **2009**, *183*, 179.
- (55) Pickett, H. M.; Poynter, I. R. L.; Cohen, E. A.; Delitsky, M. L.; Pearson, J. C.; Muller, H. S. P. *J. Quant. Spectrosc. Radiat. Transfer* **1998**, *60*, 883.
- (56) Müller, H. S. P.; Thorwirth, S.; Roth, D. A.; Winnewisser, G. *Astron. Astrophys.* **2001**, *370*, L49.
- (57) Müller, H. S. P.; Schlöder, F.; Stutzki, J.; Winnewisser, G. *J. Mol. Struct.* **2005**, *742*, 215.
- (58) De Lucia, F.; Gordy, W.; Helminger, P.; Cook, R. *Phys. Rev. A* **1972**, *5*, 487.
- (59) Polyansky, O.; Zobov, N.; Viti, S.; Tennyson, J.; Bernath, P.; Wallace, L. *J. Mol. Spectrosc.* **1997**, *186*, 422.
- (60) Toth, R. *J. Mol. Spectrosc.* **1999**, *194*, 28.
- (61) Yu, S.; Pearson, J.; Drouin, B.; Martin-Drumel, M.-A.; Pirali, O.; Vervloet, M.; Coudert, L.; Mueller, H.; Bruenken, S. *J. Mol. Spectrosc.* **2012**, *279*, 16.
- (62) Coudert, L. H.; Wagner, G.; Birk, M.; Baranov, Y. I.; Lafferty, W. J.; Flaud, J. M. *J. Mol. Spectrosc.* **2008**, *251*, 339.
- (63) De Lucia, F.; Helminger, P. *J. Mol. Spectrosc.* **1975**, *56*, 138.

- (64) Steenbeck, G.; Bellet, J. *Comptes Rendus B* **1971**, 273, 471.
- (65) Johns, J. J. *Opt. Soc. Am. B-Opt. Phys.* **1985**, 2, 1340.
- (66) Guelachvili, G. *J. Opt. Soc. Am.* **1983**, 73, 137.
- (67) Melnick, G. J.; et al. *Astron. Astrophys.* **2010**, 521, L27.
- (68) Herczeg, G. J.; Karska, A.; Bruderer, S.; Kristensen, L. E.; van Dishoeck, E. F.; Jørgensen, J. K.; Visser, R.; Wampfler, S. F.; Bergin, E. A.; Yıldız, U. A.; Pontoppidan, K. M.; Gracia-Carpio, J. *Astron. Astrophys.* **2012**, 540, A84.
- (69) Coutens, A.; Vastel, C.; Caux, E.; Ceccarelli, C.; Bottinelli, S.; Wiesenfeld, L.; Faure, A.; Scribano, Y.; Kahane, C. *Astron. Astrophys.* **2012**, 539, A132.
- (70) Neill, J. L.; Wang, S.; Bergin, E. A.; Crockett, N. R.; Favre, C.; Plume, R.; Melnick, G. J. *Astrophys. J.* **2013**, 770, 142.
- (71) Watson, D. M.; Bohac, C. J.; Hull, C.; Forrest, W. J.; Furlan, E.; Najita, J.; Calvet, N.; D'Alessio, P.; Hartmann, L.; Sargent, B.; Green, J. D.; Kim, K. H.; Houck, J. R. *Nature* **2007**, 448, 1026.
- (72) Carr, J. S.; Najita, J. R. *Science* **2008**, 319, 1504.
- (73) Salyk, C.; Pontoppidan, K. M.; Blake, G. A.; Lahuis, F.; van Dishoeck, E. F.; Evans, N. J., II. *Astrophys. J. Lett.* **2008**, 676, L49.
- (74) Pontoppidan, K. M.; Salyk, C.; Blake, G. A.; Meijerink, R.; Carr, J. S.; Najita, J. *Astrophys. J.* **2010**, 720, 887.
- (75) Flaud, J.; Camypreyret, C. *J. Mol. Spectrosc.* **1975**, 55, 278.
- (76) Camypreyret, C.; Flaud, J. *Mol. Phys.* **1976**, 32, 523.
- (77) Rothman, L. S.; et al. *J. Quant. Spectrosc. Radiat. Transfer* **2009**, 110, 533.
- (78) Bruenken, S.; Mueller, H. S. P.; Endres, C.; Lewen, F.; Giesen, T.; Drouin, B.; Pearson, J. C.; Maeder, H. *Phys. Chem. Chem. Phys.* **2007**, 9, 2103.
- (79) Barber, R.; Tennyson, J.; Harris, G.; Tolchenov, R. *Mon. Not. R. Astron. Soc.* **2006**, 368, 1087.
- (80) Shirin, S.; Polyansky, O.; Zobov, N.; Ovsyannikov, R.; Csaszar, A.; Tennyson, J. *J. Mol. Spectrosc.* **2006**, 236, 216.
- (81) Voronin, B. A.; Tennyson, J.; Tolchenov, R. N.; Lugovskoy, A. A.; Yurchenko, S. N. *Mon. Not. R. Astron. Soc.* **2010**, 402, 492.
- (82) Tennyson, J.; Shine, K. P. *Philos. Trans. R. Soc., A* **2012**, 370, 2491.
- (83) Helmich, F. P.; van Dishoeck, E. F.; Black, J. H.; de Graauw, T.; Beintema, D. A.; Heras, A. M.; Lahuis, F.; Morris, P. W.; Valentijn, E. A. *Astron. Astrophys.* **1996**, 315, L173.
- (84) Gudipati, M.; Castillo-Rogez, J. (Eds.) *The Science of Solar System Ices*; Springer: New York, 2013.
- (85) D'Hendecourt, L.; Joblin, C.; Jones, A. (Eds.) *Solid Interstellar Matter: The ISO Revolution*; Springer: Berlin, 1999.
- (86) Hudgins, D. M.; Sandford, S. A.; Allamandola, L. J.; Tielens, A. G. G. M. *Astrophys. J., Suppl. Ser.* **1993**, 86, 713.
- (87) Tielens, A. G. G. M. *Astron. Astrophys.* **1983**, 119, 177.
- (88) Smith, R. G.; Sellgren, K.; Tokunaga, A. T. *Astrophys. J.* **1989**, 344, 413.
- (89) Jenniskens, P.; Blake, D.; Wilson, M.; Pohorille, A. *Astrophys. J.* **1995**, 455, 389.
- (90) Stevenson, K.; Kimmel, G.; Dohnalek, Z.; Smith, R.; Kay, B. *Science* **1999**, 283, 1505.
- (91) Kimmel, G.; Stevenson, K.; Dohnalek, Z.; Smith, R.; Kay, B. *J. Chem. Phys.* **2001**, 114, 5284.
- (92) Schutte, W. A. *Astron. Astrophys.* **2002**, 386, 1103.
- (93) Jenniskens, P.; Blake, D. *Science* **1994**, 265, 753.
- (94) Ehrenfreund, P.; Boogert, A. C. A.; Gerakines, P. A.; Jansen, D. J.; Schutte, W. A.; Tielens, A. G. G. M.; van Dishoeck, E. F. *Astron. Astrophys.* **1996**, 315, L341.
- (95) Bouwman, J.; Ludwig, W.; Awad, Z.; Öberg, K. I.; Fuchs, G. W.; van Dishoeck, E. F.; Linnartz, H. *Astron. Astrophys.* **2007**, 476, 995.
- (96) Moore, M. H.; Hudson, R. L. *Astrophys. J.* **1992**, 401, 353.
- (97) Moore, M. H.; Hudson, R. L. *Astron. Astrophys., Suppl. Ser.* **1994**, 103, 45.
- (98) Gibb, E. L.; Whittet, D. C. B.; Boogert, A. C. A.; Tielens, A. G. G. M. *Astrophys. J., Suppl. Ser.* **2004**, 151, 35.
- (99) Boogert, A. C. A.; et al. *Astrophys. J.* **2008**, 678, 985.
- (100) Boogert, A. C. A.; Tielens, A. G. G. M.; Ceccarelli, C.; Boonman, A. M. S.; van Dishoeck, E. F.; Keane, J. V.; Whittet, D. C. B.; de Graauw, T. *Astron. Astrophys.* **2000**, 360, 683.
- (101) Whittet, D. C. B.; Shenoy, S. S.; Bergin, E. A.; Chiar, J. E.; Gerakines, P. A.; Gibb, E. L.; Melnick, G. J.; Neufeld, D. A. *Astrophys. J.* **2007**, 655, 332.
- (102) Boogert, A. C. A.; Huard, T. L.; Cook, A. M.; Chiar, J. E.; Knez, C.; Decin, L.; Blake, G. A.; Tielens, A. G. G. M.; van Dishoeck, E. F. *Astrophys. J.* **2011**, 729, 92.
- (103) Soifer, B. T.; Willner, S. P.; Rudy, R. J.; Capps, R. W. *Astrophys. J.* **1981**, 250, 631.
- (104) Sylvester, R. J.; Kemper, F.; Barlow, M. J.; de Jong, T.; Waters, L. B. F. M.; Tielens, A. G. G. M.; Omont, A. *Astron. Astrophys.* **1999**, 352, 587.
- (105) Spoon, H. W. W.; Armus, L.; Cami, J.; Tielens, A. G. G. M.; Chiar, J. E.; Peeters, E.; Keane, J. V.; Charmandaris, V.; Appleton, P. N.; Teplitz, H. I.; Burgdorf, M. J. *Astrophys. J., Suppl. Ser.* **2004**, 154, 184.
- (106) Sajina, A.; Spoon, H.; Yan, L.; Imanishi, M.; Fadda, D.; Elitzur, M. *Astrophys. J.* **2009**, 703, 270.
- (107) Shimonishi, T.; Onaka, T.; Kato, D.; Sakon, I.; Ita, Y.; Kawamura, A.; Kaneda, H. *Astron. Astrophys.* **2010**, 514, A12.
- (108) Bossa, J.-B.; Isokoski, K.; de Valois, M. S.; Linnartz, H. *Astron. Astrophys.* **2012**, 545, A82.
- (109) Aitken, D. K.; Smith, C. H.; James, S. D.; Roche, P. F.; Hough, J. H. *Mon. Not. R. Astron. Soc.* **1988**, 230, 629.
- (110) Schegerer, A. A.; Wolf, S. *Astron. Astrophys.* **2010**, 517, A87.
- (111) Fillion, J.; van Harreveld, R.; Ruiz, J.; Castillejo, N.; Zanganeh, A.; Lemaire, J.; van Hemert, M.; Rostas, F. *J. Phys. Chem. A* **2001**, 105, 11414.
- (112) Yoshino, K.; Esmond, J.; Parkinson, W.; Ito, K.; Matsui, T. *Chem. Phys.* **1996**, 211, 387.
- (113) Cheng, B.; Chew, E.; Liu, C.; Bahou, M.; Lee, Y.; Yung, Y.; Gerstell, M. *Geophys. Res. Lett.* **1999**, 26, 3657.
- (114) Keller-Rudek, H.; Moortgat, G.; Sander, R.; Sörensen, R. (Eds.) *MPI-Mainz UV/VIS Spectral Atlas of Gaseous Molecules*, www.uv-vis-spectral-atlas-mainz.org, 2013.
- (115) Andersson, S.; van Dishoeck, E. F. *Astron. Astrophys.* **2008**, 491, 907.
- (116) Andersson, S.; Al-Halabi, A.; Kroes, G.-J.; van Dishoeck, E. F. *J. Chem. Phys.* **2006**, 124, 064715.
- (117) Ajello, J. M. *Geophys. Res. Lett.* **1984**, 11, 1195.
- (118) Green, S.; Maluendes, S.; McLean, A. D. *Astrophys. J., Suppl. Ser.* **1993**, 85, 181.
- (119) Phillips, T. R.; Maluendes, S.; Green, S. *Astrophys. J., Suppl. Ser.* **1996**, 107, 467.
- (120) Dubernet, M.; Daniel, F.; Grosjean, A.; Lin, C. Y. *Astron. Astrophys.* **2009**, 497, 911.
- (121) Daniel, F.; Dubernet, M.-L.; Grosjean, A. *Astron. Astrophys.* **2011**, 536, A76.
- (122) Valiron, P.; Wernli, M.; Faure, A.; Wiesenfeld, L.; Rist, C.; Kedzuch, S.; Noga, J. *J. Chem. Phys.* **2008**, 129, 134306.
- (123) Indriolo, N.; Neufeld, D. A.; Seifahrt, A.; Richter, M. *J. Astrophys. J.* **2013**, 776, 8.
- (124) Meijerink, R.; Pontoppidan, K. M.; Blake, G. A.; Poelman, D. R.; Dullemond, C. P. *Astrophys. J.* **2009**, 704, 1471.
- (125) Faure, A.; Josselin, E. *Astron. Astrophys.* **2008**, 492, 257.
- (126) Neufeld, D. A. *Astrophys. J.* **2012**, 749, 125.
- (127) Wiesenfeld, L.; Faure, A. *Phys. Rev. A* **2010**, 82, 040702.
- (128) Drouin, B.; Wiesenfeld, L. *Phys. Rev. A* **2012**, 86, 022705.
- (129) Yang, C.-H.; Sarma, G.; ter Meulen, J. J.; Parker, D. H.; McBane, G. C.; Wiesenfeld, L.; Faure, A.; Scribano, Y.; Feautrier, N. *J. Chem. Phys.* **2010**, 122, 131103.
- (130) van der Avoird, A.; Nesbitt, D. J. *J. Chem. Phys.* **2011**, 134, 044314.
- (131) van der Avoird, A.; Scribano, Y.; Faure, A.; Weida, M. J.; Fair, J. R.; Nesbitt, D. J. *Chem. Phys.* **2012**, 399, 28.
- (132) Ziemkiewicz, M. P.; Pluetzer, C.; Nesbitt, D. J.; Scribano, Y.; Faure, A.; van der Avoird, A. *J. Chem. Phys.* **2012**, 137, 084301.
- (133) Dick, M.; Drouin, B.; Pearson, J. *Phys. Rev. A* **2010**, 81, 022706.
- (134) Daniel, F.; Goicoechea, J. R.; Cernicharo, J.; Dubernet, M.-L.; Faure, A. *Astron. Astrophys.* **2012**, 547, A81.

- (135) Crimier, N.; Faure, A.; Ceccarelli, C.; Valiron, P.; Wiesenfeld, L.; Dubernet, M. L. In *Molecules in Space and Laboratory*; International Astrophysics and Astrochemistry Conference; Lemaire, J. L.; Combes, F., Ed.; S. Diana: Paris, 2007.
- (136) Crimier, C.; Faure, A.; Ceccarelli, C.; Valiron, P.; Wiesenfeld, L.; Dubernet, M. L. In *SF2A-2007: Proceedings of the Annual Meeting of the French Society of Astronomy and Astrophysics*; Bouvier, J., Chalabaev, A., Charbonnel, C., Eds.; 2007; p 241.
- (137) Grosjean, A.; Dubernet, M.-L.; Ceccarelli, C. *Astron. Astrophys.* **2003**, *408*, 1197.
- (138) Faure, A.; Crimier, N.; Ceccarelli, C.; Valiron, P.; Wiesenfeld, L.; Dubernet, M. L. *Astron. Astrophys.* **2007**, *472*, 1029.
- (139) Hollenbach, D.; Elitzur, M.; McKee, C. F. *Astrophys. J.* **2013**, *773*, 70.
- (140) Dubernet, M.-L.; et al. *Astron. Astrophys.* **2013**, *553*, A50.
- (141) Schöier, F. L.; van der Tak, F. F. S.; van Dishoeck, E. F.; Black, J. H. *Astron. Astrophys.* **2005**, *432*, 369.
- (142) Bernes, C. *Astron. Astrophys.* **1979**, *73*, 67.
- (143) Rybicki, G. B.; Hummer, D. G. *Astron. Astrophys.* **1991**, *245*, 171.
- (144) Hummer, D. G.; Rybicki, G. B. *Astrophys. J.* **1982**, *254*, 767.
- (145) Sobolev, V. V. *Moving Envelopes of Stars*; Harvard University Press: Cambridge, 1960.
- (146) Hogerheijde, M. R.; van der Tak, F. F. S. *Astron. Astrophys.* **2000**, *362*, 697.
- (147) Brinch, C.; Hogerheijde, M. R. *Astron. Astrophys.* **2010**, *523*, A25.
- (148) van der Tak, F. F. S.; Black, J. H.; Schöier, F. L.; Jansen, D. J.; van Dishoeck, E. F. *Astron. Astrophys.* **2007**, *468*, 627.
- (149) de Jong, T. *Astron. Astrophys.* **1973**, *26*, 297.
- (150) Genzel, R. In *Masers, Molecules, and Mass Outflows in Star Formation Regions*; Haschick, A. D., Moran, J. M., Eds.; Haystack: Westford, 1986; p 233.
- (151) Garay, G.; Moran, J. M.; Haschick, A. D. *Astrophys. J.* **1989**, *338*, 244.
- (152) Neufeld, D. A.; Wu, Y.; Kraus, A.; Menten, K. M.; Tolls, V.; Melnick, G. J.; Nagy, Z. *Astrophys. J.* **2013**, *769*, 48.
- (153) Neufeld, D. A.; Melnick, G. J. *Astrophys. J.* **1991**, *368*, 215.
- (154) Alcolea, J.; Menten, K. M. In *Astrophysical Masers*; Lecture Notes in Physics; Clegg, A. W., Nedoluha, G. E., Eds.; Springer: Berlin, 1993; Vol. 412; p 399.
- (155) Waters, J. W.; Kakar, R. K.; Kuiper, T. B. H.; Roscoe, H. K.; Swanson, P. N.; Rodriguez Kuiper, E. N.; Kerr, A. R.; Thaddeus, P.; Gustincic, J. *J. Astrophys. J.* **1980**, *235*, 57.
- (156) Menten, K. M.; Melnick, G. J.; Phillips, T. G. *Astrophys. J. Lett.* **1990**, *350*, L41.
- (157) Menten, K. M.; Melnick, G. J.; Phillips, T. G.; Neufeld, D. A. *Astrophys. J. Lett.* **1990**, *363*, L27.
- (158) Phillips, T. G.; Kwan, J.; Huggins, P. J. In *Interstellar Molecules*; IAU Symposium; Andrew, B. H., Ed.; Kluwer: Dordrecht, 1980; Vol. 87; pp 21.
- (159) Melnick, G. J.; Menten, K. M.; Phillips, T. G.; Hunter, T. *Astrophys. J. Lett.* **1993**, *416*, L37.
- (160) Menten, K. M.; Lundgren, A.; Belloche, A.; Thorwirth, S.; Reid, M. J. *Astron. Astrophys.* **2008**, *477*, 185.
- (161) Justtanont, K.; et al. *Astron. Astrophys.* **2012**, *537*, A144.
- (162) Menten, K. M.; Melnick, G. J. *Astrophys. J. Lett.* **1989**, *341*, L91.
- (163) Menten, K. M.; Philipp, S. D.; Güsten, R.; Alcolea, J.; Polehampton, E. T.; Brünken, S. *Astron. Astrophys.* **2006**, *454*, L107.
- (164) Walsh, A. J.; et al. *Mon. Not. R. Astron. Soc.* **2011**, *416*, 1764.
- (165) Lo, K. Y. *Annu. Rev. Astron. Astrophys.* **2005**, *43*, 625.
- (166) Surcis, G.; Tarchi, A.; Henkel, C.; Ott, J.; Lovell, J.; Castangia, P. *Astron. Astrophys.* **2009**, *502*, 529.
- (167) Brunthaler, A.; Henkel, C.; de Blok, W. J. G.; Reid, M. J.; Greenhill, L. J.; Falcke, H. *Astron. Astrophys.* **2006**, *457*, 109.
- (168) Braatz, J. A.; Reid, M. J.; Humphreys, E. M. L.; Henkel, C.; Condon, J. J.; Lo, K. Y. *Astrophys. J.* **2010**, *718*, 657.
- (169) Reid, M. J.; Menten, K. M.; Zheng, X. W.; Brunthaler, A.; Xu, Y. *Astrophys. J.* **2009**, *705*, 1548.
- (170) Wakelam, V.; Smith, I. W. M.; Herbst, E.; Troe, J.; Geppert, W.; Linnartz, H.; Öberg, K.; Roueff, E.; Agundez, M.; Pernot, P.; Cuppen, H. M.; Loison, J. C.; Talbi, D. *Space Sci. Rev.* **2010**, *156*, 13.
- (171) Steinfeld, J.; Francisco, J.; Hase, W. *Chemical Kinetics and Dynamics*; Prentice Hall: Upper Saddle River, NJ, 1999.
- (172) Su, T.; Chesnavich, W. *J. Chem. Phys.* **1982**, *76*, 5183.
- (173) Maergoiz, A. I.; Nikitin, E. E.; Troe, J. *Int. J. Mass Spectrom.* **2009**, *280*, 42.
- (174) Woon, D. E.; Herbst, E. *Astrophys. J. Suppl. Ser.* **2009**, *185*, 273.
- (175) Anicich, V. *An Index of the Literature for Bimolecular Gas Phase Cation-Molecule Reaction Kinetics*; JPL Publication 03-19; JPL: Pasadena, CA, 2003.
- (176) Smith, I. W. M.; Herbst, E.; Chang, Q. *Mon. Not. R. Astron. Soc.* **2004**, *350*, 323.
- (177) Mitchell, J.; Florescu-Mitchell, A. *Phys. Rep.* **2006**, *430*, 277.
- (178) Larsson, M.; Orel, A. In *Dissociative Recombination of Molecular Ions*; Larsson, M., Ed.; Cambridge Univ. Press: Cambridge, 2008.
- (179) Rimmer, P. B.; Herbst, E.; Morata, O.; Roueff, E. *Astron. Astrophys.* **2012**, *537*, A7.
- (180) Padovani, M.; Galli, D.; Glassgold, A. E. *Astron. Astrophys.* **2009**, *501*, 619 (erratum **2013**, *549*, C3)..
- (181) Padovani, M.; Galli, D.; Glassgold, A. E. *Astron. Astrophys.* **2013**, *549*, C3.
- (182) McCall, B. J.; et al. *Nature* **2003**, *422*, 500.
- (183) Indriolo, N.; McCall, B. J. *Astrophys. J.* **2012**, *745*, 91.
- (184) Padovani, M.; Galli, D. In *Cosmic Rays in Star-Forming Environments*; Advances in Solid State Physics; Torres, D. F., Reimer, O., Eds.; Springer: Berlin, 2013; Vol. 34; p 61.
- (185) Hollenbach, D.; Salpeter, E. E. *Astrophys. J.* **1971**, *163*, 155.
- (186) Cazaux, S.; Tielens, A. G. G. M. *Astrophys. J.* **2010**, *715*, 698.
- (187) Katz, N.; Furman, I.; Biham, O.; Pirronello, V.; Vidali, G. *Astrophys. J.* **1999**, *522*, 305.
- (188) Chang, Q.; Cuppen, H. M.; Herbst, E. *Astron. Astrophys.* **2005**, *434*, 599.
- (189) Iqbal, W.; Acharyya, K.; Herbst, E. *Astrophys. J.* **2012**, *751*, 58.
- (190) Cazaux, S.; Tielens, A. G. G. M. *Astrophys. J. Lett.* **2002**, *575*, L29.
- (191) van Dishoeck, E. F.; Black, J. H. *Astrophys. J. Suppl. Ser.* **1986**, *62*, 109.
- (192) Cordiner, M. A.; Millar, T. J. *Astrophys. J.* **2009**, *697*, 68.
- (193) Wakelam, V.; et al. *Astrophys. J. Suppl. Ser.* **2012**, *199*, 21.
- (194) Herbst, E.; Millar, T. In *Low Temperatures and Cold Molecules*; Smith, I. W. M., Ed.; Imperial College: London, 2008; p 1.
- (195) Gerin, M.; et al. *Astron. Astrophys.* **2010**, *518*, L110.
- (196) Benz, A. O.; et al. *Astron. Astrophys.* **2010**, *521*, L35.
- (197) Bruderer, S.; et al. *Astron. Astrophys.* **2010**, *521*, L44.
- (198) Gupta, H.; et al. *Astron. Astrophys.* **2010**, *521*, L47.
- (199) Wyrowski, F.; et al. *Astron. Astrophys.* **2010**, *521*, L34.
- (200) Wyrowski, F.; Menten, K. M.; Güsten, R.; Belloche, A. *Astron. Astrophys.* **2010**, *518*, A26.
- (201) Menten, K. M.; Wyrowski, F.; Belloche, A.; Güsten, R.; Dedes, L.; Müller, H. S. P. *Astron. Astrophys.* **2011**, *525*, A77.
- (202) Field, G. B.; Steigman, G. *Astrophys. J.* **1971**, *166*, 59.
- (203) Spirko, J. A.; Zirbel, J. J.; Hickman, A. P. *J. Phys. B: At. Mol. Opt. Phys.* **2003**, *36*, 1645.
- (204) Jensen, M. J.; Bilodeau, R. C.; Safvan, C. P.; Seiersen, K.; Andersen, L. H.; Pedersen, H. B.; Heber, O. *Astrophys. J.* **2000**, *543*, 764.
- (205) Buhr, H.; et al. *Phys. Rev. Lett.* **2010**, *105*.
- (206) Neau, A.; Al Khalili, A.; Rosen, S.; Le Padellec, A.; Derkatch, A.; Shi, W.; Vikor, L.; Larsson, M.; Semaniak, J.; Thomas, R.; Nagard, M.; Andersson, K.; Danared, H.; af Ugglas, M. *J. Chem. Phys.* **2000**, *113*, 1762.
- (207) Herd, C. R.; Adams, N. G.; Smith, D. *Astrophys. J.* **1990**, *349*, 388.
- (208) Okabe, H. *Photochemistry of Small Molecules*; Wiley: New York, 1978.
- (209) van Hemert, M.; van der Avoird, A. *J. Chem. Phys.* **1979**, *71*, 5310.
- (210) Engel, V.; Schinke, R.; Staemmler, V. *J. Chem. Phys.* **1988**, *88*, 129.

- (211) Engel, V.; Staemmler, V.; VanderWal, R.; Crim, F.; Sension, R.; Hudson, B.; Andresen, P.; Hennig, S.; Weide, K.; Schinke, R. *J. Phys. Chem. A* **1992**, *96*, 3201.
- (212) Schinke, R. *Photodissociation Dynamics*; Cambridge University Press: Cambridge, 1993.
- (213) van Harreveld, R.; van Hemert, M. *J. Chem. Phys.* **2001**, *114*, 9453.
- (214) Hwang, D.; Yang, X.; Harich, S.; Lin, J.; Yang, X. *J. Chem. Phys.* **1999**, *110*, 4123.
- (215) Yang, X.; Hwang, D.; Lin, J.; Ying, X. *J. Chem. Phys.* **2000**, *113*, 10597.
- (216) van Harreveld, R.; van Hemert, M. *J. Chem. Phys.* **2000**, *112*, 5787.
- (217) Harich, S.; Hwang, D.; Yang, X.; Lin, J.; Yang, X.; Dixon, R. *J. Chem. Phys.* **2000**, *113*, 10073.
- (218) van Harreveld, R.; van Hemert, M.; Schatz, G. *J. Phys. Chem. A* **2001**, *105*, 11480.
- (219) van Dishoeck, E. F. In *Rate Coefficients in Astrochemistry*; Astrophysics and Space Science Library; Millar, T. J., Williams, D. A., Eds.; Springer: New York, 1988; Vol. 146; pp 49–72.
- (220) van Dishoeck, E. F. *Proc. Natl. Acad. Sci., U. S. A.* **2006**, *103*, 12249.
- (221) Aikawa, Y.; Herbst, E. *Astron. Astrophys.* **1999**, *351*, 233.
- (222) Stäuber, P.; Jørgensen, J. K.; van Dishoeck, E. F.; Doty, S. D.; Benz, A. O. *Astron. Astrophys.* **2006**, *453*, 555.
- (223) Harada, N.; Herbst, E.; Wakelam, V. *Astrophys. J.* **2010**, *721*, 1570 (erratum **2012**, *756*, 104).
- (224) Baulch, D.; Cobos, C.; Cox, R.; Esser, C.; Frank, P.; Just, T.; Kerr, J.; Pilling, M.; Troe, J.; Walker, R.; Warnatz, J. *J. Phys. Chem. Ref. Data* **1992**, *21*, 411.
- (225) Balakrishnan, N. *J. Chem. Phys.* **2004**, *121*, 6346.
- (226) Charnley, S. B. *Astrophys. J.* **1997**, *481*, 396.
- (227) Javoy, S.; Naudet, V.; Abid, S.; Paillard, C. *Exp. Therm. Fluid Sci.* **2003**, *27*, 371.
- (228) Atkinson, R.; Baulch, D.; Cox, R.; Crowley, J.; Hampson, R.; Hynes, R. *Atmos. Chem. Phys.* **2004**, *4*, 1461.
- (229) Sultanov, R.; Balakrishnan, N. *J. Chem. Phys.* **2004**, *121*, 11038.
- (230) Han, J.; Chen, X.; Weiner, B. *Chem. Phys. Lett.* **2000**, *332*, 243.
- (231) Bergin, E. A.; Neufeld, D. A.; Melnick, G. *J. Astrophys. J.* **1998**, *499*, 777.
- (232) Draine, B. T.; Roberge, W. G.; Dalgarno, A. *Astrophys. J.* **1983**, *264*, 485.
- (233) Cuppen, H. M.; Ioppolo, S.; Romanzin, C.; Linnartz, H. *Phys. Chem. Chem. Phys.* **2010**, *12*, 12077.
- (234) Lamberts, T.; Cuppen, H. M.; Ioppolo, S.; Linnartz, H. *Phys. Chem. Chem. Phys.* **2013**, *15*, 8287.
- (235) Öberg, K. I.; Boogert, A. C. A.; Pontoppidan, K. M.; van den Broek, S.; van Dishoeck, E. F.; Bottinelli, S.; Blake, G. A.; Evans, N. J., II. *Astrophys. J.* **2011**, *740*, 109.
- (236) Oba, Y.; Watanabe, N.; Hama, T.; Kuwahata, K.; Hidaka, H.; Kouchi, A. *Astrophys. J.* **2012**, *749*, 67.
- (237) Fayolle, E. C.; Öberg, K. I.; Cuppen, H. M.; Visser, R.; Linnartz, H. *Astron. Astrophys.* **2011**, *S29*, A74.
- (238) Buch, V.; Zhang, Q. *Astrophys. J.* **1991**, *379*, 647.
- (239) Al-Halabi, A.; van Dishoeck, E. F. *Mon. Not. R. Astron. Soc.* **2007**, *382*, 1648.
- (240) Öberg, K. I.; Linnartz, H.; Visser, R.; van Dishoeck, E. F. *Astrophys. J.* **2009**, *693*, 1209.
- (241) Fayolle, E. C.; Bertin, M.; Romanzin, C.; Michaut, X.; Öberg, K. I.; Linnartz, H.; Fillion, J.-H. *Astrophys. J. Lett.* **2011**, *739*, L36.
- (242) Dulieu, F.; Congiu, E.; Noble, J.; Baouche, S.; Chaabouni, H.; Moudens, A.; Minissale, M.; Cazaux, S. *Sci. Rep.* **2013**, *3*, 1338.
- (243) Ioppolo, S.; Cuppen, H. M.; Romanzin, C.; van Dishoeck, E. F.; Linnartz, H. *Astrophys. J.* **2008**, *686*, 1474.
- (244) Cuppen, H. M.; van Dishoeck, E. F.; Herbst, E.; Tielens, A. G. G. M. *Astron. Astrophys.* **2009**, *508*, 275.
- (245) Ward, M. D.; Price, S. D. *Astrophys. J.* **2011**, *741*, 121.
- (246) Ioppolo, S.; Cuppen, H. M.; Romanzin, C.; van Dishoeck, E. F.; Linnartz, H. *Phys. Chem. Chem. Phys.* **2010**, *12*, 12065.
- (247) Miyuchi, N.; Hidaka, H.; Chigai, T.; Nagaoka, A.; Watanabe, N.; Kouchi, A. *Chem. Phys. Lett.* **2008**, *456*, 27.
- (248) Dulieu, F.; Amiaud, L.; Congiu, E.; Fillion, J.; Matar, E.; Momeni, A.; Pirronello, V.; Lemaire, J. L. *Astron. Astrophys.* **2010**, *S12*, A30.
- (249) Romanzin, C.; Ioppolo, S.; Cuppen, H. M.; van Dishoeck, E. F.; Linnartz, H. *J. Chem. Phys.* **2011**, *134*, 084504.
- (250) Accolla, M.; Congiu, E.; Manico, G.; Dulieu, F.; Chaabouni, H.; Lemaire, J. L.; Pirronello, V. *Mon. Not. R. Astron. Soc.* **2013**, *429*, 3200.
- (251) Dulieu, F. In *IAU Symposium*; Cernicharo, J., Bachiller, R., Eds.; Cambridge University Press: Cambridge, 2011; Vol. 280; p 405.
- (252) Cuppen, H. M.; Herbst, E. *Astrophys. J.* **2007**, *668*, 294.
- (253) Du, F.; Parise, B.; Bergman, P. *Astron. Astrophys.* **2012**, *S38*, A91.
- (254) Sandford, S. A.; Allamandola, L. J. *Icarus* **1990**, *87*, 188.
- (255) Collings, M. P.; McCoustra, M. R. S. In *Astrochemistry: Recent Successes and Current Challenges*; IAU Symposium; Lis, D. C., Blake, G. A., Herbst, E., Eds.; Cambridge University Press: Cambridge, 2005; Vol. 231; pp 405.
- (256) Collings, M. P.; Anderson, M. A.; Chen, R.; Dever, J. W.; Viti, S.; Williams, D. A.; McCoustra, M. R. S. *Mon. Not. R. Astron. Soc.* **2004**, *354*, 1133.
- (257) Westley, M. S.; Baragiola, R. A.; Johnson, R. E.; Baratta, G. A. *Nature* **1995**, *373*, 405.
- (258) Arasa, C.; Andersson, S.; Cuppen, H. M.; van Dishoeck, E. F.; Kroes, G.-J. *J. Chem. Phys.* **2010**, *132*, 184510.
- (259) Arasa, C.; Andersson, S.; Cuppen, H. M.; van Dishoeck, E. F.; Kroes, G. J. *J. Chem. Phys.* **2011**, *134*, 164503.
- (260) Koning, J.; Kroes, G. J.; Arasa, C. *J. Chem. Phys.* **2013**, *138*.
- (261) Arasa, C.; Koning, J.; Kroes, G.; Walsh, C.; van Dishoeck, E. *Astron. Astrophys.* **2013**, submitted.
- (262) Hollenbach, D.; Kaufman, M. J.; Neufeld, D.; Wolfire, M.; Goicoechea, J. R. *Astrophys. J.* **2012**, *754*, 105.
- (263) Hollenbach, D. J.; Tielens, A. G. G. M. *Annu. Rev. Astron. Astrophys.* **1997**, *35*, 179.
- (264) Aikawa, Y.; van Zadelhoff, G. J.; van Dishoeck, E. F.; Herbst, E. *Astron. Astrophys.* **2002**, *386*, 622.
- (265) Lee, J.; Bergin, E. A.; Evans, N. J., II. *Astrophys. J.* **2004**, *617*, 360.
- (266) Aikawa, Y.; Wakelam, V.; Garrod, R. T.; Herbst, E. *Astrophys. J.* **2008**, *674*, 984.
- (267) Visser, R.; van Dishoeck, E. F.; Doty, S. D.; Dullemond, C. P. *Astron. Astrophys.* **2009**, *495*, 881.
- (268) Aikawa, Y.; Wakelam, V.; Hersant, F.; Garrod, R. T.; Herbst, E. *Astron. Astrophys. J.* **2012**, *760*, 40.
- (269) Wakelam, V.; Herbst, E.; Le Bourlot, J.; Hersant, F.; Selsis, F.; Guilloteau, S. *Astron. Astrophys.* **2010**, *S17*, A21.
- (270) Wakelam, V.; Herbst, E.; Selsis, F. *Astron. Astrophys.* **2006**, *451*, 551.
- (271) Hasegawa, T. I.; Herbst, E. *Mon. Not. R. Astron. Soc.* **1993**, *263*, 589.
- (272) Caselli, P.; Hasegawa, T. I.; Herbst, E. *Astrophys. J.* **1998**, *495*, 309.
- (273) Garrod, R. T. *Astron. Astrophys.* **2008**, *491*, 239.
- (274) Garrod, R. T.; Vasyunin, A. I.; Semenov, D. A.; Wiebe, D. S.; Henning, T. *Astrophys. J. Lett.* **2009**, *700*, L43.
- (275) Stantcheva, T.; Shematovich, V. I.; Herbst, E. *Astron. Astrophys.* **2002**, *391*, 1069.
- (276) Caselli, P.; Stantcheva, T.; Shalabiea, O.; Shematovich, V. I.; Herbst, E. *Planet. Space Sci.* **2002**, *50*, 1257.
- (277) Du, F.; Parise, B. *Astron. Astrophys.* **2011**, *530*, A131.
- (278) Chang, Q.; Herbst, E. *Astrophys. J.* **2012**, *759*, 147.
- (279) Vasyunin, A. I.; Herbst, E. *Astrophys. J.* **2013**, *762*, 86.
- (280) van Dishoeck, E.; Bergin, E.; Lis, D.; Lunine, J. In *Protostars & Planets VI*; Beuther, H., Klessen, R., Dullemond, K., Henning, Th., Eds.; University of Arizona Press: Tucson, AZ, 2013.
- (281) Kristensen, L. E.; van Dishoeck, E. F. *Astron. Nachr.* **2011**, *332*, 475.
- (282) Nisini, B.; et al. *Astron. Astrophys.* **2010**, *S18*, L120.
- (283) Caselli, P.; et al. *Astron. Astrophys.* **2010**, *S21*, L29.
- (284) Hogerheijde, M. R.; Bergin, E. A.; Brinch, C.; Cleeves, L. I.; Fogel, J. K. J.; Blake, G. A.; Dominik, C.; Lis, D. C.; Melnick, G.; Neufeld, G.

- D.; Panić, O.; Pearson, J. C.; Kristensen, L.; Yıldız, U. A.; van Dishoeck, E. F. *Science* **2011**, 334, 338.
- (285) Sonnentrucker, P.; et al. *Astron. Astrophys.* **2010**, 521, L12.
- (286) Monje, R. R.; Emprechtinger, M.; Phillips, T. G.; Lis, D. C.; Goldsmith, P. F.; Bergin, E. A.; Bell, T. A.; Neufeld, D. A.; Sonnentrucker, P. *Astrophys. J. Lett.* **2011**, 734, L23.
- (287) Indriolo, N.; Neufeld, D. A.; Seifahrt, A.; Richter, M. J. *Astrophys. J.* **2013**, 764, 188.
- (288) Cernicharo, J.; Lim, T.; Cox, P.; Gonzalez-Alfonso, E.; Caux, E.; Swinyard, B. M.; Martin-Pintado, J.; Baluteau, J. P.; Clegg, P. *Astron. Astrophys.* **1997**, 323, L25.
- (289) Flagey, N.; Goldsmith, P. F.; Lis, D. C.; Gerin, M.; Neufeld, D.; Sonnentrucker, P.; De Luca, M.; Godard, B.; Goicoechea, J. R.; Monje, R.; Phillips, T. G. *Astrophys. J.* **2013**, 762, 11.
- (290) Sonnentrucker, P.; Neufeld, D. A.; Gerin, M.; De Luca, M.; Indriolo, N.; Lis, D. C.; Goicoechea, J. R. *Astrophys. J. Lett.* **2013**, 763, L19.
- (291) González-Alfonso, E.; et al. *Astron. Astrophys.* **2012**, 541, A4.
- (292) Fischer, J.; Sturm, E.; González-Alfonso, E.; Gracia-Carpio, J.; Hailey-Dunsheath, S.; Poglitsch, A.; Contursi, A.; Lutz, D.; Genzel, R.; Sternberg, A.; Verma, A.; Tacconi, L. *Astron. Astrophys.* **2010**, 518, L41.
- (293) Neufeld, D. A.; et al. *Astron. Astrophys.* **2010**, 521, L5.
- (294) Wiesemeyer, H.; Güsten, R.; Heyminck, S.; Jacobs, K.; Menten, K. M.; Neufeld, D. A.; Requena-Torres, M. A.; Stutzki, J. *Astron. Astrophys.* **2012**, 542, L7.
- (295) Roueff, E. *Mon. Not. R. Astron. Soc.* **1996**, 279, L37.
- (296) Weselak, T.; Galazutdinov, G.; Beletsky, Y.; Krełowski, J. *Astron. Astrophys.* **2009**, 499, 783.
- (297) Weselak, T.; Galazutdinov, G. A.; Beletsky, Y.; Krełowski, J. *Mon. Not. R. Astron. Soc.* **2010**, 402, 1991.
- (298) González-Alfonso, E.; et al. *Astron. Astrophys.* **2013**, 550, A25.
- (299) Habart, E.; et al. *Astron. Astrophys.* **2010**, 518, L116.
- (300) Goicoechea, J. R.; Joblin, C.; Contursi, A.; Berne, O.; Cernicharo, J.; Gerin, M.; Le Bourlot, J.; Bergin, E. A.; Bell, T. A.; Rollig, M. *Astron. Astrophys.* **2011**, 530, L16.
- (301) Sternberg, A.; Dalgarno, A. *Astrophys. J., Suppl. Ser.* **1995**, 99, 565.
- (302) Pilleri, P.; Fuente, A.; Cernicharo, J.; Ossenkopf, V.; Berne, O.; Gerin, M.; Pety, J.; Goicoechea, J. R.; Rizzo, J. R.; Montillaud, J.; Gonzalez-Garcia, M.; Joblin, C.; Le Bourlot, J.; Le Petit, F.; Kramer, C. *Astron. Astrophys.* **2012**, 544, A110.
- (303) Whittet, D. C. B.; Bode, M. F.; Longmore, A. J.; Adamson, A. J.; McFadzean, A. D.; Aitken, D. K.; Roche, P. F. *Mon. Not. R. Astron. Soc.* **1988**, 233, 321.
- (304) Walmsley, C. M. In *Chemistry and Spectroscopy of Interstellar Molecules*; Bohme, D. K., Ed.; University of Tokyo Press: Tokyo, 1992; p 267.
- (305) Murakawa, K.; Tamura, M.; Nagata, T. *Astrophys. J., Suppl. Ser.* **2000**, 128, 603.
- (306) Pontoppidan, K. M.; van Dishoeck, E. F.; Dartois, E. *Astron. Astrophys.* **2004**, 426, 925.
- (307) Lee, H.-H.; Bettens, R. P. A.; Herbst, E. *Astron. Astrophys., Suppl. Ser.* **1996**, 119, 111.
- (308) Przybilla, N.; Nieva, M.-F.; Butler, K. *Astrophys. J. Lett.* **2008**, 688, L103.
- (309) Whittet, D. C. B. *Astrophys. J.* **2010**, 710, 1009.
- (310) Boonman, A. M. S.; Doty, S. D.; van Dishoeck, E. F.; Bergin, E. A.; Melnick, G. J.; Wright, C. M.; Stark, R. *Astron. Astrophys.* **2003**, 406, 937.
- (311) Bergin, E. A.; et al. *Astrophys. J. Lett.* **2000**, 539, L129.
- (312) Roberts, H.; Herbst, E. *Astron. Astrophys.* **2002**, 395, 233.
- (313) Caselli, P.; Keto, E.; Bergin, E. A.; Tafalla, M.; Aikawa, Y.; Douglas, T.; Pagani, L.; Yıldız, U. A.; van der Tak, F. F. S.; Walmsley, C. M.; Codella, C.; Nisini, B.; Kristensen, L. E.; van Dishoeck, E. F. *Astrophys. J. Lett.* **2012**, 759, L37.
- (314) Evans, N. J., II *Annu. Rev. Astron. Astrophys.* **1999**, 37, 311.
- (315) Kristensen, L. E.; et al. *Astron. Astrophys.* **2012**, 542, A8.
- (316) Mottram, J. C.; van Dishoeck, E. F.; Schmalzl, M.; Kristensen, L. E.; Visser, R.; Hogerheijde, M. R.; Bruderer, S. *Astron. Astrophys.* **2013**, 558, A126.
- (317) Bergin, E. A.; et al. *Astron. Astrophys.* **2010**, 521, L33.
- (318) Fogel, J. K. J.; Bethell, T. J.; Bergin, E. A.; Calvet, N.; Semenov, D. *Astrophys. J.* **2011**, 726, 29.
- (319) Dominik, C.; Ceccarelli, C.; Hollenbach, D.; Kaufman, M. *Astrophys. J. Lett.* **2005**, 635, L85.
- (320) Parise, B.; Bergman, P.; Du, F. *Astron. Astrophys.* **2012**, 541, L11.
- (321) Bergman, P.; Parise, B.; Liseau, R.; Larsson, B.; Olofsson, H.; Menten, K. M.; Gusten, R. *Astron. Astrophys.* **2011**, 531, L8.
- (322) Charnley, S. B.; Tielens, A. G. G. M.; Millar, T. J. *Astrophys. J. Lett.* **1992**, 399, L71.
- (323) Chavarría, L.; et al. *Astron. Astrophys.* **2010**, 521, L37.
- (324) Johnstone, D.; et al. *Astron. Astrophys.* **2010**, 521, L41.
- (325) Kristensen, L. E.; et al. *Astron. Astrophys.* **2010**, 521, L30.
- (326) van Dishoeck, E. F.; Helmich, F. P. *Astron. Astrophys.* **1996**, 315, L177.
- (327) van Dishoeck, E. F.; Blake, G. A. *Annu. Rev. Astron. Astrophys.* **1998**, 36, 317.
- (328) Boonman, A. M. S.; van Dishoeck, E. F. *Astron. Astrophys.* **2003**, 403, 1003.
- (329) Emprechtinger, M.; Lis, D. C.; Rolfs, R.; Schilke, P.; Monje, R. R.; Comito, C.; Ceccarelli, C.; Neufeld, D. A.; van der Tak, F. F. S. *Astrophys. J.* **2013**, 765, 61.
- (330) Herpin, F.; Chavarría, L.; van der Tak, F.; Wyrowski, F.; van Dishoeck, E. F.; Jacq, T.; Braine, J.; Baudry, A.; Bontemps, S.; Kristensen, L. *Astron. Astrophys.* **2012**, 542, A76.
- (331) Visser, R.; Jørgensen, J. K.; Kristensen, L. E.; van Dishoeck, E. F.; Bergin, E. A. *Astrophys. J.* **2013**, 769, 19.
- (332) Persson, M. V.; Jørgensen, J. K.; van Dishoeck, E. F. *Astron. Astrophys.* **2012**, 541, A39.
- (333) Kaufman, M. J.; Neufeld, D. A. *Astrophys. J.* **1996**, 456, 611.
- (334) Harwit, M.; Neufeld, D. A.; Melnick, G. J.; Kaufman, M. J. *Astrophys. J. Lett.* **1998**, 497, L105.
- (335) Wright, C. M.; van Dishoeck, E. F.; Black, J. H.; Feuchtgruber, H.; Cernicharo, J.; González-Alfonso, E.; de Graauw, T. *Astron. Astrophys.* **2000**, 358, 689.
- (336) González-Alfonso, E.; Wright, C. M.; Cernicharo, J.; Rosenthal, D.; Boonman, A. M. S.; van Dishoeck, E. F. *Astron. Astrophys.* **2002**, 386, 1074.
- (337) Cernicharo, J.; Goicoechea, J. R.; Daniel, F.; Lerate, M. R.; Barlow, M. J.; Swinyard, B. M.; van Dishoeck, E. F.; Lim, T. L.; Viti, S.; Yates, J. *Astrophys. J. Lett.* **2006**, 649, L33.
- (338) Olofsson, A. O. H.; et al. *Astron. Astrophys.* **2003**, 402, L47.
- (339) Franklin, J.; Snell, R. L.; Kaufman, M. J.; Melnick, G. J.; Neufeld, D. A.; Hollenbach, D. J.; Bergin, E. A. *Astrophys. J.* **2008**, 674, 1015.
- (340) Lefloch, B.; et al. *Astron. Astrophys.* **2010**, 518, L113.
- (341) Goicoechea, J. R.; Cernicharo, J.; Karska, A.; Herczeg, G. J.; Polehampton, E. T.; Wampfler, S. F.; Kristensen, L. E.; van Dishoeck, E. F.; Etxaluze, M.; Berne, O.; Visser, R. *Astron. Astrophys.* **2012**, 548, A77.
- (342) Tafalla, M.; Liseau, R.; Nisini, B.; Bachiller, R.; Santiago-Garcia, J.; van Dishoeck, E. F.; Kristensen, L. E.; Herczeg, G. J.; Yıldız, U. A. *Astron. Astrophys.* **2013**, 551, A116.
- (343) Nisini, B.; et al. *Astron. Astrophys.* **2013**, 549, A16.
- (344) Santangelo, G.; Nisini, B.; Antonucci, S.; Codella, C.; Cabrit, S.; Giannini, T.; Herczeg, G. J.; Liseau, R.; Tafalla, M.; van Dishoeck, E. F. *Astron. Astrophys.* **2013**, 557, A22.
- (345) Draine, B. T. *Annu. Rev. Astron. Astrophys.* **2003**, 41, 241.
- (346) Neufeld, D. A.; Dalgarno, A. *Astrophys. J.* **1989**, 340, 869.
- (347) Flower, D. R.; Pineau Des Forêts, G. *Mon. Not. R. Astron. Soc.* **2010**, 406, 1745.
- (348) Wampfler, S. F.; Bruderer, S.; Kristensen, L. E.; Chavarria, L.; Bergin, E. A.; Benz, A. O.; van Dishoeck, E. F.; Herczeg, G. J.; van der Tak, F. F. S.; Goicoechea, J. R.; Doty, S. D.; Herpin, F. *Astron. Astrophys.* **2011**, 531, L16.
- (349) van Kempen, T. A.; et al. *Astron. Astrophys.* **2010**, 518, L121.
- (350) Wampfler, S. F.; Bruderer, S.; Karska, A.; Herczeg, G. J.; van Dishoeck, E. F.; Kristensen, L. E.; Goicoechea, J. R.; Benz, A. O.; Doty, S. D.; McCaughan, C.; Baudry, A.; Giannini, T.; Larsson, B. *Astron. Astrophys.* **2013**, 552, A56.
- (351) Karska, A.; et al. *Astron. Astrophys.* **2013**, 552, A141.

- (352) Green, J. D.; et al. *Astrophys. J.* **2013**, 770, 123.
- (353) Neufeld, D. A.; Dalgarno, A. *Astrophys. J.* **1989**, 344, 251.
- (354) Snell, R. L.; Hollenbach, D.; Howe, J. E.; Neufeld, D. A.; Kaufman, M. J.; Melnick, G. J.; Bergin, E. A.; Wang, Z. *Astrophys. J.* **2005**, 620, 758.
- (355) Nisini, B.; Giannini, T.; Lorenzetti, D. *Astrophys. J.* **2002**, 574, 246.
- (356) Bjerkeli, P.; Liseau, R.; Olberg, M.; Falgarone, E.; Frisk, U.; Hjalmarson, Å.; Klotz, A.; Larsson, B.; Olofsson, A. O. H.; Olofsson, G.; Ristorcelli, I.; Sandqvist, A. *Astron. Astrophys.* **2009**, 507, 1455.
- (357) Liseau, R.; et al. *Astron. Astrophys.* **1996**, 315, L181.
- (358) Bjerkeli, P.; Liseau, R.; Nisini, B.; Tafalla, M.; Benedettini, M.; Bergman, P.; Dionatos, O.; Giannini, T.; Herczeg, G.; Justtanont, K.; Larsson, B.; McOey, C.; Olberg, M.; Olofsson, A. O. H. *Astron. Astrophys.* **2011**, 533, A80.
- (359) Vasta, M.; Codella, C.; Lorenzani, A.; Santangelo, G.; Nisini, B.; Giannini, T.; Tafalla, M.; Liseau, R.; van Dishoeck, E. F.; Kristensen, L. *Astron. Astrophys.* **2012**, 537, A98.
- (360) Santangelo, G.; Nisini, B.; Giannini, T.; Antoniucci, S.; Vasta, M.; Codella, C.; Lorenzani, A.; Tafalla, M.; Liseau, R.; van Dishoeck, E. F.; Kristensen, L. E. *Astron. Astrophys.* **2012**, 538, A45.
- (361) Bjerkeli, P.; Liseau, R.; Larsson, B.; Rydbeck, G.; Nisini, B.; Tafalla, M.; Antoniucci, S.; Benedettini, M.; Bergman, P.; Cabrit, S.; Giannini, T.; Melnick, G.; Neufeld, D.; Santangelo, G.; van Dishoeck, E. F. *Astron. Astrophys.* **2012**, 546, A29.
- (362) Fich, M.; et al. *Astron. Astrophys.* **2010**, 518, L86.
- (363) Emprechtinger, M.; et al. *Astron. Astrophys.* **2010**, 521, L28.
- (364) van der Tak, F. F. S.; et al. *Astron. Astrophys.* **2010**, 518, L107.
- (365) Jiménez-Serra, I.; Caselli, P.; Martín-Pintado, J.; Hartquist, T. W. *Astron. Astrophys.* **2008**, 482, 549.
- (366) Jiménez-Serra, I.; Martín-Pintado, J.; Rodríguez-Franco, A.; Martín, S. *Astrophys. J. Lett.* **2005**, 627, L121.
- (367) Codella, C.; et al. *Astron. Astrophys.* **2010**, 518, L112.
- (368) Viti, S.; Jiménez-Serra, I.; Yates, J. A.; Codella, C.; Vasta, M.; Caselli, P.; Lefloch, B.; Ceccarelli, C. *Astrophys. J. Lett.* **2011**, 740, L3.
- (369) Keene, J.; Phillips, T. G.; van Dishoeck, E. F. In *International Astronomical Union Symposium*; Latter, W. B., Radford, S. J. E., Jewell, P. R., Mangum, J. G., Bally, J., Eds.; Kluwer: Dordrecht, 1997; Vol. 170; pp 382–384.
- (370) Indriolo, N.; Blake, G. A.; Goto, M.; Usuda, T.; Oka, T.; Geballe, T. R.; Fields, B. D.; McCall, B. J. *Astrophys. J.* **2010**, 724, 1357.
- (371) Reach, W. T.; Rho, J. *Astrophys. J. Lett.* **1998**, 507, L93.
- (372) Lockett, P.; Gauthier, E.; Elitzur, M. *Astrophys. J.* **1999**, 511, 235.
- (373) González-Alfonso, E.; Smith, H. A.; Fischer, J.; Cernicharo, J. *Astrophys. J.* **2004**, 613, 247.
- (374) González-Alfonso, E.; Smith, H. A.; Ashby, M. L. N.; Fischer, J.; Spinoglio, L.; Grundy, T. W. *Astrophys. J.* **2008**, 675, 303.
- (375) van der Werf, P. P.; et al. *Astron. Astrophys.* **2010**, 518, L42.
- (376) Weiß, A.; et al. *Astron. Astrophys.* **2010**, 521, L1.
- (377) Rangwala, N.; et al. *Astrophys. J.* **2011**, 743, 94.
- (378) Spinoglio, L.; et al. *Astrophys. J.* **2012**, 758, 108.
- (379) Kamenetzky, J.; et al. *Astrophys. J.* **2012**, 753, 70.
- (380) Meijerink, R.; et al. *Astrophys. J. Lett.* **2013**, 762, L16.
- (381) Yang, C.; Gao, Y.; Omont, A.; Liu, D.; Isaak, K. G.; Downes, D.; van der Werf, P. P.; Lu, N. *Astrophys. J. Lett.* **2013**, 771, L24.
- (382) Riechers, D. A.; et al. *Nature* **2013**, 496, 329.
- (383) Omont, A.; et al. *Astron. Astrophys.* **2011**, 530, L3.
- (384) van der Werf, P. P.; Berciano Alba, A.; Spaans, M.; Loenen, A. F.; Meijerink, R.; Riechers, D. A.; Cox, P.; Weiß, A.; Walter, F. *Astrophys. J. Lett.* **2011**, 741, L38.
- (385) Combes, F.; et al. *Astron. Astrophys.* **2012**, 538, L4.
- (386) Omont, A.; et al. *Astron. Astrophys.* **2013**, 551, A115.
- (387) Habing, H. J. *Astron. Astrophys. Rev.* **1996**, 7, 97.
- (388) Goldreich, P.; Scoville, N. *Astrophys. J.* **1976**, 205, 144.
- (389) Glassgold, A. E. *Annu. Rev. Astron. Astrophys.* **1996**, 34, 241.
- (390) Justtanont, K.; Skinner, C. J.; Tielens, A. G. G. M. *Astrophys. J.* **1994**, 435, 852.
- (391) Willacy, K.; Millar, T. J. *Astron. Astrophys.* **1997**, 324, 237.
- (392) Amiri, N.; Vlemmings, W.; van Langevelde, H. J. *Astron. Astrophys.* **2011**, 532, A149.
- (393) Barlow, M. J.; et al. *Astron. Astrophys.* **1996**, 315, L241.
- (394) Neufeld, D. A.; Chen, W.; Melnick, G. J.; de Graauw, T.; Feuchtgruber, H.; Haser, L.; Lutz, D.; Harwit, M. *Astron. Astrophys.* **1996**, 315, L237.
- (395) Neufeld, D. A.; Feuchtgruber, H.; Harwit, M.; Melnick, G. J. *Astrophys. J. Lett.* **1999**, 517, L147.
- (396) Justtanont, K.; Bergman, P.; Larsson, B.; Olofsson, H.; Schöier, F. L.; Frisk, U.; Hasegawa, T.; Hjalmarson, Å.; Kwok, S.; Olberg, M.; Sandqvist, A.; Volk, K.; Elitzur, M. *Astron. Astrophys.* **2005**, 439, 627.
- (397) Maercker, M.; Schöier, F. L.; Olofsson, H.; Bergman, P.; Ramstedt, S. *Astron. Astrophys.* **2008**, 479, 779.
- (398) Maercker, M.; Schöier, F. L.; Olofsson, H.; Bergman, P.; Frisk, U.; Hjalmarson, Å.; Justtanont, K.; Kwok, S.; Larsson, B.; Olberg, M.; Sandqvist, A. *Astron. Astrophys.* **2009**, 494, 243.
- (399) Decin, L.; et al. *Astron. Astrophys.* **2010**, 521, L4.
- (400) Willacy, K. *Astrophys. J. Lett.* **2004**, 600, L87.
- (401) Justtanont, K.; et al. *Astron. Astrophys.* **2010**, 521, L6.
- (402) Melnick, G. J.; Neufeld, D. A.; Ford, K. E. S.; Hollenbach, D. J.; Ashby, M. L. N. *Nature* **2001**, 412, 160.
- (403) Hasegawa, T. I.; Kwok, S.; Koning, N.; Volk, K.; Justtanont, K.; Olofsson, H.; Schöier, F. L.; Sandqvist, A.; Hjalmarson, Å.; Olberg, M.; Winnberg, A.; Nyman, L. Å.; Frisk, U. *Astrophys. J.* **2006**, 637, 791.
- (404) Saavik Ford, K. E.; Neufeld, D. A. *Astrophys. J. Lett.* **2001**, 557, L113.
- (405) Decin, L.; et al. *Nature* **2010**, 467, 64.
- (406) Neufeld, D. A.; González-Alfonso, E.; Melnick, G. J.; Szczepański, R.; Schmidt, M.; Decin, L.; de Koter, A.; Schöier, F.; Cernicharo, J. *Astrophys. J. Lett.* **2011**, 727, L28.
- (407) Cherchneff, I. *Astron. Astrophys.* **2011**, 526, L11.
- (408) Neufeld, D. A.; et al. *Astrophys. J. Lett.* **2011**, 727, L29.
- (409) Woitke, P.; Thi, W.-F.; Kamp, I.; Hogerheijde, M. R. *Astron. Astrophys.* **2009**, 501, L5.
- (410) Bethell, T.; Bergin, E. *Science* **2009**, 326, 1675.
- (411) Thi, W.-F.; Bik, A. *Astron. Astrophys.* **2005**, 438, 557.
- (412) Woitke, P.; Kamp, I.; Thi, W.-F. *Astron. Astrophys.* **2009**, 501, 383.
- (413) Glassgold, A. E.; Meijerink, R.; Najita, J. R. *Astrophys. J.* **2009**, 701, 142.
- (414) Pontoppidan, K. M.; Salyk, C.; Blake, G. A.; Kaufl, H. U. *Astrophys. J. Lett.* **2010**, 722, L173.
- (415) Salyk, C.; Pontoppidan, K. M.; Blake, G. A.; Najita, J. R.; Carr, J. S. *Astrophys. J.* **2011**, 731, 130.
- (416) Mandell, A. M.; Bast, J.; van Dishoeck, E. F.; Blake, G. A.; Salyk, C.; Mumma, M. J.; Villanueva, G. *Astrophys. J.* **2012**, 747, 92.
- (417) Fedele, D.; Pascucci, I.; Brittain, S.; Kamp, I.; Woitke, P.; Williams, J. P.; Dent, W. R. F.; Thi, W.-F. *Astrophys. J.* **2011**, 732, 106.
- (418) Zhang, K.; Pontoppidan, K. M.; Salyk, C.; Blake, G. A. *Astrophys. J.* **2013**, 766, 82.
- (419) Rivière-Marichalar, P.; Ménard, F.; Thi, W. F.; Kamp, I.; Montesinos, B.; Meeus, G.; Woitke, P.; Howard, C.; Sandell, G.; Podio, L.; Dent, W. R. F.; Mendiguta, I.; Pinte, C.; White, G. J.; Barrado, D. *Astron. Astrophys.* **2012**, 538, L3.
- (420) Fedele, D.; Bruderer, S.; van Dishoeck, E. F.; Herczeg, G. J.; Evans, N. J.; Bouwman, J.; Henning, T.; Green, J. *Astron. Astrophys.* **2012**, 544, L9.
- (421) Meeus, G.; et al. *Astron. Astrophys.* **2012**, 544, A78.
- (422) Fedele, D.; Bruderer, S.; van Dishoeck, E. F.; Carr, J.; Herczeg, G. J.; Salyk, C.; Evans, N. J.; Bouwman, J.; Meeus, G.; Henning, T.; Green, J.; Najita, J. R.; Guedel, M. *Astron. Astrophys.* **2013**, 559, A77.
- (423) Whipple, F. L. *Astrophys. J.* **1951**, 113, 464.
- (424) Haser, L. *Bull. Soc. R. Sci. Liège* **1957**, 43, 740.
- (425) Bockelée-Morvan, D.; Crovisier, J.; Mumma, M. J.; Weaver, H. A. In *Comets II*; Festou, M. C., Keller, H. U., Weaver, H. A., Eds.; University of Arizona Press: Tucson, AZ, 2004; p 391.
- (426) Festou, M. C. *Astron. Astrophys.* **1981**, 95, 69.
- (427) Crovisier, J. *Astron. Astrophys.* **1989**, 213, 459.

- (428) Mumma, M. J.; Weissman, P. R.; Stern, S. A. In *Protostars and Planets III*; Levy, E. H., Lunine, J. I., Eds.; University of Arizona Press: Tucson, AZ, 1993; pp 1177.
- (429) Crovisier, J.; Leech, K.; Bockelee-Morvan, D.; Brooke, T. Y.; Hanner, M. S.; Altieri, B.; Keller, H. U.; Lellouch, E. *Science* **1997**, 275, 1904.
- (430) Brooke, T. Y.; Sellgren, K.; Smith, R. G. *Astrophys. J.* **1996**, 459, 209.
- (431) Magee-Sauer, K.; Mumma, M. J.; DiSanti, M. A.; Dello Russo, N. *J. Geophys. Res.* **2002**, 107, 5095.
- (432) Gibb, E. L.; Mumma, M. J.; Dello Russo, N.; Disanti, M. A.; Magee-Sauer, K. *Icarus* **2003**, 165, 391.
- (433) Bonev, B. P.; Mumma, M. J.; Dello Russo, N.; Gibb, E. L.; DiSanti, M. A.; Magee-Sauer, K. *Astrophys. J.* **2004**, 615, 1048.
- (434) Bonev, B. P.; Mumma, M. J. *Astrophys. J.* **2006**, 653, 788.
- (435) Andresen, P.; Ondrey, G. S.; Titze, B. *Phys. Rev. Lett.* **1983**, 50, 486.
- (436) Raymond, J. C. *Astrophys. J., Suppl. Ser.* **1979**, 39, 1.
- (437) Tappe, A.; Lada, C. J.; Black, J. H.; Muench, A. A. *Astrophys. J. Lett.* **2008**, 680, L117.
- (438) Tappe, A.; Forbrich, J.; Martin, S.; Yuan, Y.; Lada, C. J. *Astrophys. J.* **2012**, 751, 9.
- (439) Buntkowski, G.; Limbach, H. H.; Walaszek, B.; Adamczyk, A.; Xu, Y.; Breitzke, H.; Schweitzer, A.; Gutmann, T.; Waechter, M.; Frydel, J.; Elnmller, T.; Amadeu, N.; Tietze, D.; Chaudret, B. *Z. Phys. Chem.* **2008**, 222, 1049.
- (440) Oka, T. *J. Mol. Spectrosc.* **2004**, 228, 635.
- (441) Mumma, M. J.; Charnley, S. B. *Annu. Rev. Astron. Astrophys.* **2011**, 49, 471.
- (442) Sliter, R.; Gish, M.; Vilesov, A. F. *J. Phys. Chem. A* **2011**, 115, 9682.
- (443) Hama, T.; Watanabe, N.; Kouchi, A.; Yokoyama, M. *Astrophys. J. Lett.* **2011**, 738, L15.